117

MICROSTRUCTURAL AND STRUCTURAL STABILITY OF RAPIDLY SOLIDIFIED GOLD-TITANIUM ALLOYS

by

David Peter van Heerden

A thesis submitted to the Faculty of Engineering, University of Cape Town
in fulfilment of the degree of Doctor of Philosophy

Department of Materials Engineering
University of Cape Town
March 1993

PREFACE

All of the work contained in this thesis reflects original work by the author unless otherwise explicitly stated, and none of the work presented has been submitted previously for degree purposes. Portions of the work presented have been published in the following journal articles:

"Precipitation in rapidly solidified Au-Ti alloys", D.P. van Heerden, T. Aboud, D. Shechtman and M.P. Shaw, *Mater. Lett.* **10**, 425 (1991);

"The evolution of structural order in rapidly solidified Au-Ti alloys", D.P. van Heerden, M.P. Shaw and D. Shechtman, *Phil. Mag. B*, **66**, 3, 361 (1992);

and the following international conference proceedings:

"Aspects of grain growth in rapidly solidified gold alloys", D.P. van Heerden and M.P. Shaw in *Proc. Int. Conf. on Grain Growth in Polycrystalline Materials, Rome* (eds. G. Abbruzzese and P. Bozzo) published in *Mat. Scie. Forum*, **93-94**, Pt. 2, (Trans Tech, Zürich), 571 (1991);

"Transitional order in rapidly solidified Au-Ti", D.P. van Heerden and M.P. Shaw, *Proc. 10th European Congress on Electron Microscopy: EUREM 1992, Grenada* (eds. A. López and M.I. Rodríguez-García), Vol. 2, 345 (1992);

However, the regulations regarding the submission of a PhD thesis at the University of Cape Town prohibit the inclusion of reprints of papers published by the author on the subject matter being presented in the thesis.

ABSTRACT

An investigation has been carried out into the effect of rapid solidification on the microstructure and structural order present in dilute Au-Ti alloys, and the subsequent evolution of these properties on post-solidification heat treatment. Alloys of compositions 1wt.% Ti, 2wt.% Ti, 3wt.% Ti and 5wt.% Ti have been rapidly solidified by a technique known as chill block melt spinning (CBMS). The microstructure and structural order present in the alloys both directly on solidification and after post-solidification heat treatment have been characterised using optical microscopy, scanning electron microscopy and transmission electron microscopy; the evolution of the mechanical properties on post-solidification heat treatment has been determined by means of microhardness tests.

The flow characteristics of the molten alloys are observed to deteriorate with increasing Ti content resulting in an increase the cooling rate experienced by the alloys during rapid solidification with increasing solute concentration. The as-solidified alloy microstructures are therefore rationalised on the basis of variations in both cooling rate during CBMS and solute content. TEM examination of the as-solidified ribbons demonstrates that alloys containing up to 3wt.% Ti exhibit little evidence of either solute segregation or the formation of the equilibrium, long-range-ordered (D1a) Au_4Ti phase. In a 5wt.% Ti alloy the (D1a) Au_4Ti phase is observed to nucleate during processing.

Long-exposure electron diffraction patterns from 2wt.% Ti, 3wt.% Ti and 5wt.% Ti alloys reveal diffuse intensity maxima consistent with the presence of $<1^1/_20>$ special-point order, a state of order which has not been identified previously in Au-Ti alloys. On the basis of electron diffraction patterns taken from these alloys the incorporation of elements of both DO_{22} and D1a structures within the lattice is appropriate in the description of the structural order giving rise to special-point reflections. The state of

order present in the as-solidified 2wt.% Ti and 3wt.% Ti alloys is shown to be best described by incorporating both elements of $<1^1/_20>$ special-point order and elements of the (D1a) long-range-ordered structure. In addition, the nature and distribution of the three-dimensional diffuse streaking observed in zone-axis patterns from a variety of different orientations is discussed and interpreted. This state of order is observed to be stable up to a temperature of 335°C.

The 1wt. % Ti alloy contained only 0.65wt.% Ti after processing. This loss of Ti results in extensive grain growth on heat treatment at temperatures above 350°C with no detectable second phase formation; as a result the alloy microhardness decreases on heat treatment. In the 2wt.% Ti and 3wt.% Ti alloys no grain growth is observed to occur on heat treatment at temperatures of up to 500°C. On heat treatment at 350°C the Au_4Ti phase is shown to precipitate in these alloys with a commensurate increase in the alloy microhardness. However, extended heat treatment at 500°C results in the coarsening of the Au_4Ti precipitates and is associated, in some instances, with a loss of precipitate coherency and an annealing out of orientational variants of the Au_4Ti phase.

ACKNOWLEDGEMENTS

I would like to thank the following:

Professor M.P. Shaw, my supervisor, for his guidance and encouragement;

Professor D. Shechtman of the Department of Materials Engineering, Technion: Israel Institute of Technology, Haifa, Israel for his support and guidance and for his assistance with the compilation of this thesis;

The George Sachs and Louis Edelstein Research Centres of the Technion for providing experimental facilities in Israel;

Mr. T. Aboud and the staff and students at the Department of Materials Engineering at the Technion for their assistance with the execution of the melt spinning experiments;

Professor C. Allen for his assistance with the submission of this thesis;

Ms. C. Lang for useful discussions and suggestions;

The staff of the Electron Microscope Unit for their technical support;

Dr. A. Bentley for his useful suggestions in the preparation of this thesis;

Mr B. Greeves and Mr. J Petersen for their photographic expertise and assistance and Mrs. M. Hoosen for her technical assistance;

The staff and students of the Department of Materials Engineering at the University of Cape Town for their support and encouragement;

Ms. M. Rose-Innes for moral support and her assistance in compiling this thesis.

The financial support of the FRD (Foundation for Research and Development) is gratefully acknowledged.

Dedicated to the memory of my supervisor Professor Martin Shaw.

CONTENTS

-oo0oo-

CHAPTER 1

INTRODUCTION

The basic philosophy underlying the work presented in this thesis centres on the ability of the rapid solidification process to enhance the mechanical properties of relatively dilute gold alloys. Rapid solidification enhances the mechanical properties by its influence on microstructure: rapid solidification results in refined grain sizes, metastable phase formation and enhanced terminal phase solute solubility. The latter effect is of particular interest as it allows the formation of highly supersaturated single phase solid solutions which, when allowed to decompose, can form very fine dispersions of the equilibrium second phase with a resultant enhancement of mechanical properties.

After a preliminary investigation, the Au-Ti alloy system was selected for detailed study. This choice was based largely on the ease of rapid-solidification of these alloys, and the potential demonstrated for property enhancement. In the recent past dilute Au-Ti alloys became the subject of considerable commercial interest when they were shown to produce high caratage alloys with good mechanical properties; indeed an alloy of composition Au-1wt.% Ti (4at.% Ti) has been marketed as an age-hardenable jewellery alloy (see e.g. [1]). Graham [2, 3] showed that quenching a 1wt.% Ti alloy from 800°C produced a single phase random f.c.c. solid solution. Subsequent heat treatment resulted in the precipitation of a long-range-ordered Au_4Ti phase, with commensurate mechanical property enhancement. Graham's study, however, was limited to this single alloy composition and was predominantly concerned with the serrated flow observed on deformation.

The long-range-ordered Au_4Ti phase which occurs at equilibrium in dilute Au-Ti alloys is body centred tetragonal with Strukturbericht designation D1a. A number of other alloy systems which at equilibrium possess a long-range-ordered phase with this structure form a transitional metastable state of order known as special-point order on quenching from high temperatures. At high temperatures these alloys exist as random substitutional solid solutions and, on cooling slowly to room temperature, the equilibrium long-range-ordered phase forms. However, rapid quenching from high temperatures suppresses the nucleation of the equilibrium phase and results in the formation of special-point order. This state of order is of importance in the theoretical understanding of structural order, and its characterisation and structural interpretation have been the subject of considerable controversy (see e.g. [4, 5]). Although dilute Au-Ti alloys possess the requisite D1a phase, no previous studies have been undertaken into the existence of this special-point order in these alloys.

In the work that follows a much wider range of Au-Ti alloy compositions is examined than has been studied previously. The alloys were rapidly solidified in order to produce highly supersaturated single phase solid solutions by suppressing the nucleation of the equilibrium (D1a) Au_4Ti phase. Post-solidification heat treatment of the rapidly solidified alloys should result in controlled precipitation of the Au_4Ti phase with a commensurate enhancement of mechanical properties. In addition, the suppression of the nucleation of a D1a structure during solidification increases the likelihood of retaining special-point order in Au-Ti alloys at room temperature. The characterisation of the structural order and microstructure of these as-solidified alloys, and the subsequent microstructural and structural evolution on post-solidification heat treatment, will constitute a major part of this thesis.

In Chapter 2 a review covering the existing literature on prior research on rapid solidification and the Au-rich portion of the Au-Ti alloy system is presented. The review of rapid solidification will be predominantly concerned with the physical processes behind, and microstructural consequences of, the processing technique used to prepare the materials studied in this thesis, namely chill block melt spinning. Following this review of rapid solidification the Au-rich portion of the Au-Ti alloy system is discussed. In this section of Chapter 2 the currently accepted equilibrium binary phase diagram of the system is presented, after which literature concerning the metastable state of order (known as special-point order) which has been seen in related alloy systems on quenching from high temperatures is discussed. The final section of

the chapter is an overview of the issues pertinent to the present work.

The experimental procedure, presented in Chapter 3, was to rapidly solidify alloys with a number of different compositions under standard processing conditions and then to determine changes in mechanical properties, microstructure and structural order on heat treatment. The evolution of the mechanical properties as a function of heat treatment was determined by means of microhardness measurements. Changes in microstructure were determined using metallography, where optical and electron microscopy were extensively employed. The evolution of structural order in the alloys as a function of heat treatment was interpreted by utilising zone-axis selected area electron diffraction patterns obtained by transmission electron microscopy. The results of these experiments are presented in Chapter 4, and are grouped according to experimental procedure. The more detailed results pertaining to the structural order present in the alloys directly on solidification form, by their nature, a separate section and are thus presented at the end of Chapter 4. In Chapter 5 the changes in mechanical properties on heat treatment are rationalised on the basis of the observed microstructural and structural evolution. The state of order in the as-solidified and subsequently heat treated alloys is interpreted from diffuse scattering present in zone-axis electron diffraction patterns produced by transmission electron microscopy. On the basis of this discussion, conclusions are drawn in Chapter 6, and in Chapter 7 possible future work is suggested.

-ooOoo-

CHAPTER 2

LITERATURE REVIEW

The work that follows is primarily concerned with the effect of a rapid solidification technique known as chill block melt spinning (CBMS) on microstructure and mechanical properties of dilute Au-Ti alloys. This chapter serves to review a broad range of existing literature covering the physical processes behind, and microstructural consequences of, rapid solidification by means of CBMS. The Au-Ti alloy system is then discussed and the current literature on the structural order seen in related alloy systems on quenching from high temperatures is reviewed. An overview of the issues central to the present work is presented in the final section of this chapter.

2.1 RAPID SOLIDIFICATION PROCESSING

"Rapid solidification" is a term used to describe a process in which solidification is carried out under high cooling rates, typically above 10^5 K/s [6]. Materials produced by rapid solidification have been the subject of considerable interest as they possess enhanced mechanical, electrical, magnetic and other properties (see e.g. [6, 7, 8]). These enhanced properties are due to the ability of the rapid solidification process to modify the microstructure of materials by refining grain sizes, enhancing solute solubility, reducing solute segregation and forming metastable phases.

The high cooling rates associated with rapid solidification processes are achieved by rapidly forming a thin molten layer in good thermal contact with an effective heat sink. Under these conditions, heat flows quickly from the melt, causing rapid cooling and solidification. Techniques for achieving rapid solidification conditions can be classified as weld methods, spray methods or chill methods [6, 7]. In weld methods a thin, molten layer is formed on the surface of a substantial sample by means of a high energy, short duration pulse from a laser beam, electron beam, or plasma beam. The molten layer is

in intimate contact with the bulk of the sample and is rapidly cooled in situ on the chill surface. Cooling rates of between 10^6 K/s and 10^8 K/s are achieved by means of this process (see e.g. [8]). Weld methods are used commercially for modifying the surface properties of materials via surface alloying, surface cladding, or by surface homogenization [8, 9].

In spray methods rapid solidification is obtained via the fragmentation of a molten metal stream into droplets which cool and solidify; an example of a typical spray method, atomization, is illustrated in fig. 2.1(a). During atomization, a stable molten metal stream is impinged upon by several high-velocity gas or liquid jets, thereby breaking up the stream into small droplets. The droplets are cooled in flight by both convection and radiation and solidify into small particles. The final product of the process is thus a rapidly solidified powder, which may be consolidated into nett shapes of utility. Typical cooling rates achieved by the atomization process are between 10^2 K/s and 10^4 K/s [10].

In chill methods of rapid solidification the melt retains its integrity throughout solidification; an example of a chill method, chill block melt spinning (CBMS), is illustrated schematically in fig. 2.1(b). In CBMS molten metal is expelled through a small nozzle in the base of a reservoir onto the surface of a swiftly rotating disk or drum. On impact the molten metal jet spreads into a transient metal puddle. As the melt in the puddle is in intimate contact with the substrate surface, it is rapidly cooled, solidifying into a thin ribbon. Cooling rates of up to 10^6 K/s have been reported for CBMS (see e.g. [11, 12]). This technique has been used widely on a laboratory scale to research the effect of rapid solidification on alloy systems, as it allows the production of rapidly solidified products from relatively small quantities of material. In addition, the continuous ribbon product resulting from CBMS is readily handled subsequent to solidification (see e.g. [13]). Indeed, it was for these reasons that the alloys examined here were prepared using this technique. A review of the current literature on the CBMS rapid solidification process and the influence of this process on microstructure is presented in the sections that follow.

(a)

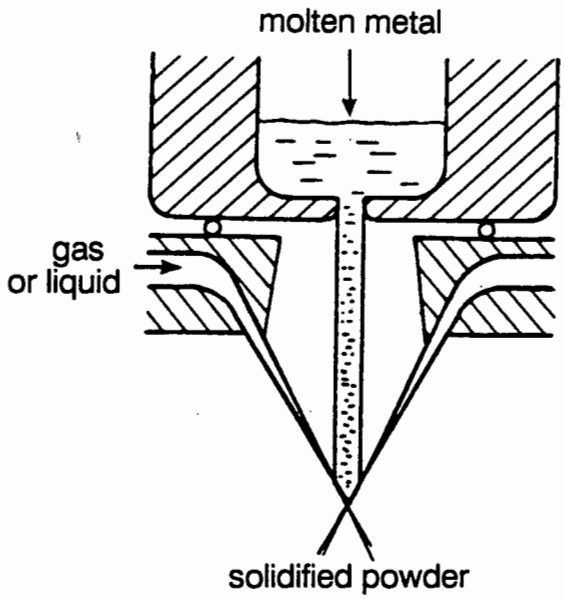

(b)

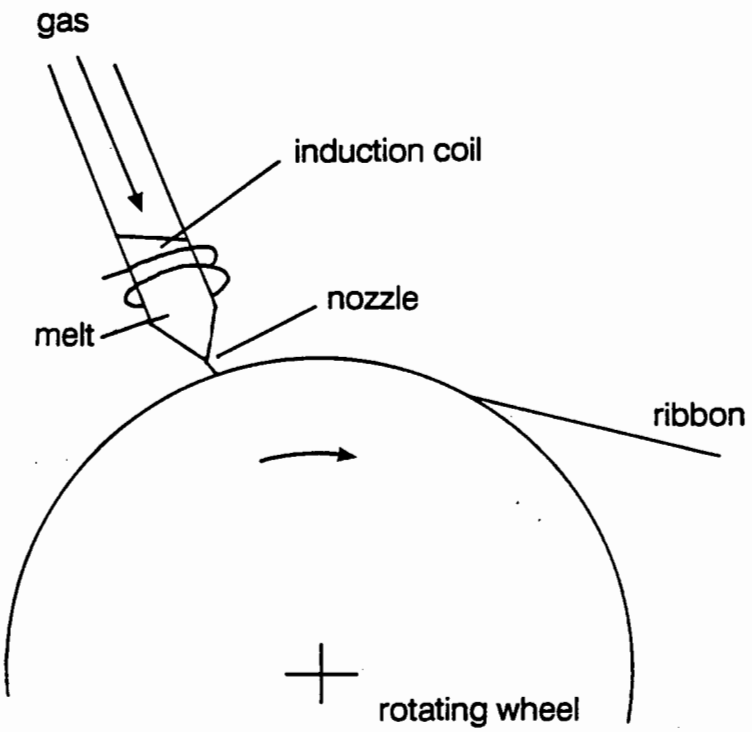

Fig. 2.1 Schematic illustrations of (a) the atomization and (b) the chill block melt spinning rapid solidification techniques (after Jones [7]).

2.1.1 The Chill Block Melt Spinning Process

This method of rapid solidification was first developed in 1908 [14] and subsequently reinvented in 1958 by Pond [15]. The most common configuration for CBMS is illustrated schematically in fig. 2.1(b). The alloy charge is placed in a crucible and induction-melted to a temperature in excess of the alloy liquidus. The melt is then expelled by gas overpressure through a nozzle in the base of the crucible. The molten metal jet impinges on the circumference of a rapidly rotating high thermal conductivity wheel forming a turbulent, although dimensionally fairly stable, melt puddle. On striking the wheel, heat is extracted from the melt and the alloy solidifies into a thin ribbon. After travelling a short distance on the wheel surface, the ribbon breaks free by differential thermal contraction [16].

CBMS has been extensively modelled in order to establish the range of process parameters over which stable ribbon formation occurs, as well as the effect of the various processing parameters on both the cooling rate of the alloy during CBMS and on the geometry of the final ribbon product. One of the earliest models was developed by Liebermann and Graham [17] who, by applying Bernoulli's equation to the column of liquid metal during ejection from the nozzle, showed that the dependence of the cross-sectional area of the ribbon (A_r) on the processing parameters was:

$$A_r = (\pi\phi^2 P^{1/2})/(2^{3/2} V_s \rho^{1/2}) \qquad (2.1)$$

where ϕ is the liquid jet diameter (taken as the nozzle diameter), P is the expulsion gas overpressure, V_s is the surface velocity of the wheel and ρ is the melt density. In addition, Liebermann and Graham showed that, in metallic glass forming alloys, the ribbon thickness was primarily determined by the wheel speed, while the ribbon width was predominantly determined by the diameter of the nozzle. However, they did not attempt to determine the controlling physical processes behind rapid solidification. The use of equation (2.1) was subsequently generalised by Charter *et al.* [18] to crystalline systems by the incorporation of an additional term which allowed for energy losses in the nozzle during melt expulsion.

One of the first attempts at a detailed analysis of the physical processes during CBMS was by Kavesh [19]. He suggested that ribbon formation in CBMS occurs as a result of the effect of heat transfer and momentum transfer on the molten metal in the puddle.

Should momentum transfer be the dominant mode of ribbon formation, a liquid layer will be dragged out of the melt puddle by the rapidly moving chill surface, with solidification occurring at some distance "downstream" from the puddle. However, should thermal transport be more efficient in the melt, a solid boundary layer travelling at the chill surface speed will form adjacent to the chill surface and grow into the melt. Provided that minimal momentum transfer occurs between the solidified material and the puddle, the ribbon emerging from the melt pool is thus entirely solidified. Kavesh suggested that, as thermal transport propagation in molten metals (as given by the diffusive constant of heat) is generally between three and nine times faster than momentum transport (as given by the diffusive constant of vorticity or kinematic viscosity), ribbon formation during CBMS should be controlled by thermal transport. Kavish was primarily concerned with the modelling of ribbon formation in metallic glasses; consequently he devised a model based on the propagation of a thermal boundary layer corresponding to the glass transition temperature of the alloy. From this model the dependence of the width (w) and thickness (X) of the ribbons on processing parameters was shown to be given by:

$$w = c'' Q^n / V_s^{1-n} \qquad (2.2(a))$$

$$X = (c'')^{-1} Q^{1-n} / V_s^n \qquad (2.2(b))$$

where c" is a material-dependent constant, Q is the volumetric flow rate of the melt, and n is a constant with a value between 0.75 and 1. Applying his formulation to the experimental results of Lieberman and Graham [17] for a metallic glass, Kavesh showed that equation (2.2(a)) fitted the data well, while equation (2.2(b)) was somewhat less successful. Charter *et al.* [18] later showed that these equations were also applicable to the rapid solidification of alloy systems forming crystalline products. However, the validity of Kavesh's model was questioned by Vincent and Davies[20], who subsequently successfully fitted the data of Liebermann *et al.* to a model which used momentum transport as the dominant mode of ribbon formation. Vincent and Davies [20] argued that there exists considerable resistance to heat flow between the melt pool and the substrate, inhibiting the heat flow during solidification and thus necessitating the incorporation of momentum transport in the modelling. Solidification during CBMS has also been modelled using a combination of momentum and thermal transport, with the two transport mechanisms interacting closely with one another (see e.g. [21, 22, 23]). These models show that the relative contributions of momentum and thermal transport in ribbon formation are influenced by factors such as the nature of the alloy being

solidified and the processing parameters.

In spite of objections to Kavesh's model, equations of the form of equation (2.2(a)) and equation (2.2(b)) have proved to be extremely useful in describing the effect of processing parameters on the ribbon geometry. Studies on a large number of crystalline and metallic glass forming systems have shown empirically that the ribbon thickness (X) is given by [20, 24, 25, 26]:

$$X = a_1 Q^n / V_S^{2n} \qquad (2.3)$$

where a_1 is a material dependent constant and n is a constant with value between 0.3 and 0.4; w may be calculated from equation (2.3) by continuity considerations (i.e. $Q = V_S w X$).

The dominant mechanism of ribbon formation is influenced by the prevalent mode of heat transfer during solidification [21, 22]. If the heat flow is Newtonian during solidification, the rate of heat extraction is determined by the flow of heat across the ribbon-substrate interface and is consequently dependent upon the temperature difference across the interface. Under Newtonian heat flow conditions there are no thermal gradients in the melt prior to solidification, nor are there temperature gradients generated in either the solidified material or the melt on the commencement of solidification. As the resistance to heat flow is predominantly at the ribbon-wheel interface, there should be little difference in temperature between the solidified ribbon and the remainder of the melt. During solidification there is, however, a decrease in the measured cooling rate due to the generation of the latent heat of solidification. Once solidification is complete the ribbon continues to cool without any thermal gradients (see e.g. [27]). Standard analysis for Newtonian heat flow conditions shows that the instantaneous ribbon cooling rate (dT/dt) is given by [7, 28, 29]:

$$dT/dt = B_1 h (T - T_w)/X \qquad (2.4(a))$$

where B_1 is a material constant, T is the instantaneous ribbon temperature, h is the heat transfer coefficient at the ribbon/wheel interface, T_w is the wheel temperature and X is the ribbon thickness. The solid-liquid interfacial velocity (R) during plane-front solidification is then given by [7, 21]:

$$R = B_2h/(T_f - T_w) \qquad (2.4(b))$$

where B_2 is a material constant and T_f is the alloy freezing temperature. Integrating equation (2.4(a)) shows that the ribbon temperature decays exponentially with time.

For non-Newtonian cooling the thermal gradients in the alloy and substrate must be considered when calculating the ribbon cooling rate (see e.g. [27, 30]). In the extreme case of non-Newtonian cooling, namely ideal cooling, there is effectively no resistance to heat flow across the liquid metal-substrate interface and thermal diffusion is determined entirely by the thermal gradients in the ribbon and in the substrate. As a result, the analytical expression for the cooling rate (dT/dt) is now dependent upon distance from the ribbon-wheel interface (x) [30, 31]:

$$dT/dt = B_3/x^2 \qquad (2.5(a))$$

and the interfacial velocity is given by [7]:

$$R = B_4/x \qquad (2.5(b))$$

where B_3 and B_4 are functions of relevant temperature intervals and material properties, but are independent of h. The criterion for determining which type of heat flow prevails during solidification is the Nusselt number (N), which is given by hX/k_s (where k_s is the thermal conductivity of the ribbon). When N is greater than approximately 30, heat flow is ideal, while when N is less than approximately 0.015 the heat flow is Newtonian [24, 27]. At N values between these extremes cooling is termed intermediate. The dependence of the Nusselt number on the ribbon thickness implies that in thinner ribbons the heat flow may be Newtonian, while in the same alloy thicker ribbons may cool under ideal cooling conditions.

The average cooling rate and the prevalent heat flow mode during CBMS have been determined using both indirect and direct methods. When using indirect methods the size of features such as secondary dendrite spacing, eutectic phase spacing or grain size in the rapidly solidified products are correlated with previously determined calibrations of these features at known cooling rates (see e.g. [32, 33]). However, the calibrations for these methods are generally taken at low cooling rates and then extrapolated; as a result the reliability of the cooling rates determined by indirect methods has been

questioned [24]. Direct methods make use of calibrated photographic or video techniques to determine the cooling rates "in situ" during solidification (see e.g. [24, 34]). Still photography was used by Hillman and Hilzinger [35] to determine the thickness (X) of a metallic glass ribbon as a function of melt pool length (l_{pool}) and substrate velocity (V_s). They showed that the ribbon thickness was given by:

$$X = C_1(l_{pool}/V_S)^m = C_1(\theta_R)^m \qquad (2.6)$$

where C_1 is a proportionality constant, m is constant (approximately equal to 0.5) and θ_R is the residence time of the melt in the puddle; Huang *et al.* [36] and Thoma *et al.* [37] obtained similar expressions for crystalline alloys. Assuming that the melt puddle length defines the solidification time in which a ribbon of a particular thickness is formed, the relationship between the residence time and ribbon thickness allows direct derivation of the propagation velocity of the solid-liquid interface. As equation (2.6) gives the measured ribbon thickness as a function of the melt puddle residence time (θ_R), differentiating this equation defines the rate of propagation of the solidification front during CBMS. By differentiating equation (2.6) and substituting time (t) for θ_R, the rate of interface propagation is shown to be inversely proportional to solidified thickness (i.e. 1/x). The velocity of the growth front shows the same inverse dependence on solidified thickness when solidification is occurring under ideal heat flow conditions (equation (2.5(b))) and it was therefore argued that during CBMS solidification occurs under ideal heat flow conditions. The relationship between melt pool length and solidification time proposed by Hillman and Hilzinger was, however, disputed by Vincent and Davies[20], who suggested that a significant proportion of the material leaving the puddle was still liquid, and hence that the "residence time" did not represent the time taken for the melt to solidify into a ribbon.

Cantor and his co-workers have shown by means of a photocalometric technique [11, 24, 25, 28] that heat flow during CBMS of a crystalline alloy system occurs under near-Newtonian conditions (Nusselt number 0.02 to 0.08). In order to determine the cooling rate of the alloy at various distances from the melt pool, still colour photography was used and the temperature of the ribbon determined from the photographic colour density by comparison with a calibrated standard. Gillen and Cantor [24], however, showed from dimensional analysis of the melt spun ribbons that heat flow during solidification was ideal. They attributed this change in heat flow during CBMS, from ideal during solidification to Newtonian on leaving the melt puddle, to a deterioration

in thermal contact between the ribbon and the substrate immediately after solidification as a result of solidification shrinkage. The near-ideal heat flow conditions during solidification suggested by Cantor *et al.* are consistent with the results of Huang *et al.* [36] and Thoma *et al.* [37] and are supported by independent theoretical and experimental evidence [21, 22, 34, 38].

Using their photocalometric technique, Cantor and his co-workers also studied the effect of various processing parameters on the cooling rate during CBMS. They showed that the cooling rate varies linearly with wheel speed, and is virtually independent of all other processing parameters. Cantor *et al.* suggested that this dependence is in part due to an increase in the heat transfer coefficient between the alloy and the substrate with increasing wheel speed. This increase in the heat transfer coefficient is believed to be due to a decrease in the incorporation of ambient gas between the ribbon and the wheel with increasing wheel speed, resulting in greater contact area at the interface between the alloy and the wheel (as was suggested previously by Huang and Fiedler [39]). In addition, as heat flow during much of the rapid solidification is near-Newtonian, from equation (2.4(a)) the average ribbon cooling rate is inversely proportional to the ribbon thickness. The average ribbon cooling rate would thus also be expected to increase with increasing wheel speed from heat flow arguments.

Although the dependence of the cooling rate is simply (and rather conveniently) related to the processing parameters, it is apparent from the above discussion that ribbon formation during CBMS occurs as a result of the interaction of a number of complex physical processes. As a result, an explicit mathematical model of CBMS of crystalline materials incorporating thermal transfer and momentum transfer phenomena has not as yet been satisfactorily derived, although considerable progress has been made towards this end [40, 41]. Ultimately, the major limitation on the modelling will be the uncertainty associated with key parameters such as the kinematic viscosity as a function of melt supercooling (in the modelling of momentum transfer phenomena), and the heat transfer coefficient (in the modelling of thermal transport). Relating these factors to the phenomena which determine the microstructure of rapidly solidified materials, such as the stability of the solid-liquid interface, is not possible at this stage. Consequently, the local conditions at the solid-liquid interface during CBMS are largely unknown and the current understanding of the solidification process is based mainly on empirical studies of the solidification process [40].

2.2 MICROSTRUCTURAL CONSEQUENCES OF RAPID SOLIDIFICATION

In spite of the difficulties associated with modelling CBMS, considerable advances have been made recently towards understanding the microstructural consequences of this rapid solidification technique. In this section the current literature concerning the physical principles underlying the microstructural modifications resulting from CBMS such as reduced microsegregation, the refinement of grain size and the formation of metastable phases is reviewed. The review is confined to the more salient aspects of the theory which are of particular relevance to rapid solidification by CBMS; for more general reviews of this rather complex and topical field see Jones [40], Kurz and Fisher [42] and Kurz and Trivedi [43].

2.2.1 The Effect of Rapid Solidification on Microsegregation

A common characteristic of rapidly solidified alloys is enhanced terminal phase solute solubility and the refinement of microsegregation [44]. The classical theory for considering microsegregation is the principle of constitutional supercooling as originally proposed by Rutter and Chalmers [45] and subsequently interpreted quantitatively by Tiller, Rutter, Jackson and Chalmers [46]. The principle, while predicting the refinement of microsegregation associated with rapid solidification, does not predict the enhanced solute solubility which is characteristic of these microstructures [31, 47]. This discrepancy occurs as a number of assumptions behind this principle are invalid under the solidification conditions prevalent during rapid solidification. In this section the principle of constitutional supercooling is described along with a discussion of the limitations of the theory when applied to rapid solidification. The additional factors which should be taken into account when modelling rapid solidification are then discussed. The modern theory of solidification (which incorporates these factors) is reviewed with particular emphasis on the application of the theory to rapid solidification. Finally, the predictions of the modern theory with respect to interface stability during rapid solidification by means of CBMS are discussed and the available experimental evidence supporting the theory presented.

The principle of constitutional supercooling predicts the morphological stability of the advancing interface by determining the thermodynamic stability of the liquid ahead of the solidification front. Provided that local equilibrium exists at the solid-liquid

interface and that the equilibrium partition coefficient (k) is less than unity, solute build-up will occur in the melt ahead of the advancing growth front during solidification. When the system reaches steady state, the solid forming will be of composition C_0, the composition of the liquid far ahead of the interface, while the liquid at the interface will be of composition C_0/k (fig. 2.2(a)). The concentration of solute decreases exponentially with distance from the interface; the thickness of this boundary layer is inversely proportional to interface velocity. The variation in solute content in the liquid as a function of distance from the interface results in the local equilibrium solidification temperature of the melt varying as a function of distance from the interface (shown as T_l in fig. 2.2(b)). If the temperature gradient in the melt ahead of the advancing interface (G_L) is positive, the temperature of the melt varies as a function of distance from the interface. Should the local temperature (T_q) of an element of melt be below its equilibrium solidification temperature (T_l), the liquid is supercooled with respect to its composition and hence the interface is morphologically unstable. The interface will therefore solidify with a dendritic or cellular microstructure with solute-enriched microsegregation between the cells or dendrite arms. The stability parameter that emerges from the principle of constitutional supercooling is the ratio of the temperature gradient in the liquid ahead of the advancing interface (G_L) to the interface velocity (R); the dependence of the morphology of the interface on G_L and R is illustrated in fig. 2.3. The criteria for the formation of a planar solid-liquid interface during solidification (i.e. for the formation of microsegregation-free microstructures) from the principle of constitutional supercooling is [48]:

$$G_L \geq m_L G_C = m_L R C_0 (k - 1)/D_L k \qquad (2.7)$$

where m_L is the slope of the liquidus line†, G_C is the unperturbed solute gradient at the interface, R is the interface velocity and D_L is the diffusivity of the solute in the melt.

When the melt is supercooled prior to solidification, G_L will be negative, and thus (as may be deduced from fig. 2.2(b)) the principle of constitutional supercooling predicts that the interface will be morphologically unstable, irrespective of the value of G_C. The solidification of an undercooled alloy melt will thus invariably result in the formation of a microsegregated microstructure.

† m_L is defined as being positive when k is greater than unity, and negative when k is less than unity [42].

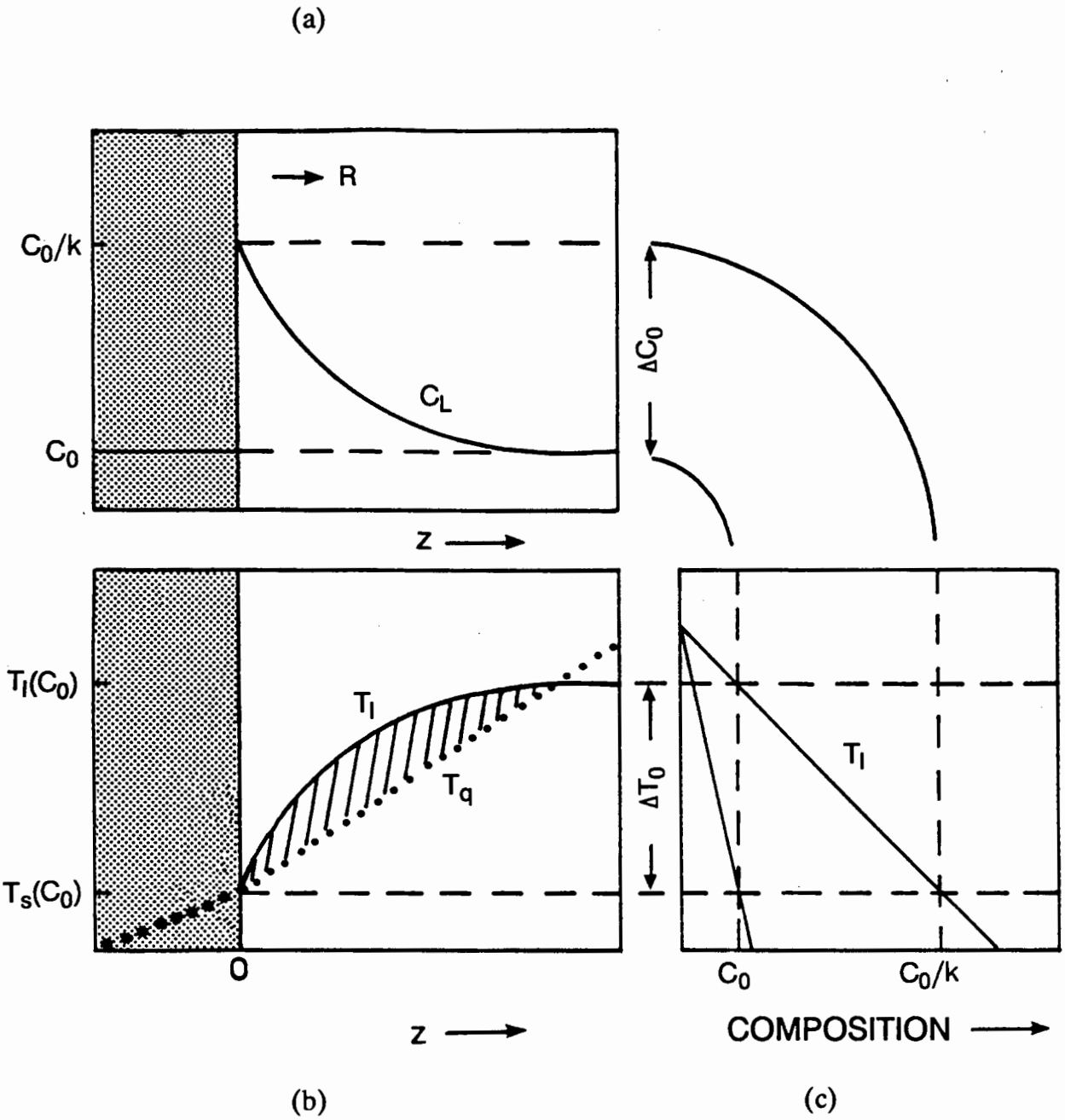

Fig. 2.2 Schematic illustration of the principle of constitutional supercooling; (a) graph of the composition (C_L) of liquid ahead of the advancing planar interface (velocity R) as a function of distance (z) from the interface. (b) Graph showing the equilibrium solidification temperature (T_l) of the liquid ahead of the interface as a function of distance from the interface. Also shown in the graph is the temperature (T_q) at which each element of the melt finds itself as a result of heat flow from the melt into the solid. (c) Equilibrium binary phase diagram of the solidifying alloy system (after Kurz and Fisher [42]).

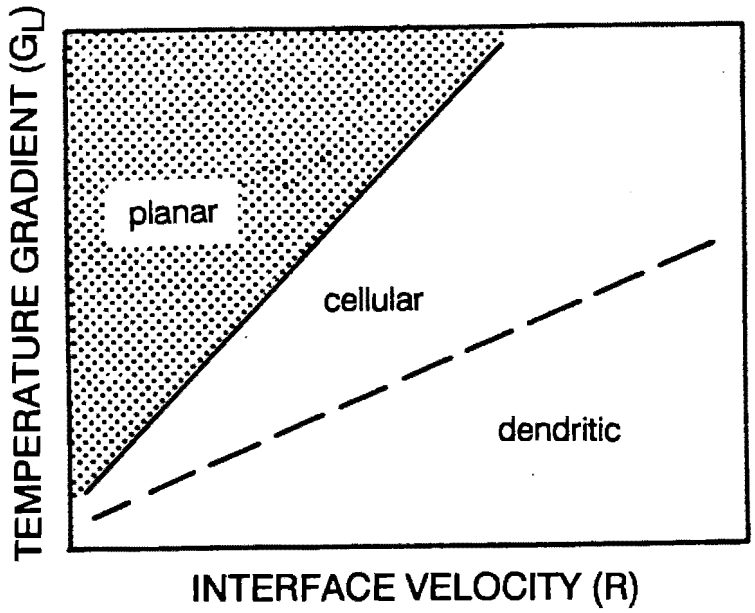

Fig. 2.3 The morphology of the advancing solid-liquid interface as a function of temperature gradient in the liquid ahead of the advancing interface (G_L) and interface velocity (R) as predicted by the principle of constitutional supercooling (after Mehrabian [31]).

The principle of constitutional supercooling predicts that under rapid solidification conditions microsegregation should invariably occur, i.e. the principle does not predict the enhanced terminal phase solute solubility characteristic of rapid solidification. However, there are a number of assumptions made in this principle that are not valid under rapid solidification conditions (see e.g. [31, 47, 49]). The equilibrium partition coefficient, for example, is assumed to describe the distribution of solute at the interface, surface tension (or capillarity) at the growth front is assumed to be negligible and the effects of the evolution of latent heat of solidification are ignored. The influence of each of these factors on the stability of the interface is discussed in the following sections.

(a) The influence of interface velocity on the partition coefficient.

In the principle of constitutional supercooling local equilibrium was assumed to describe the amount of solute rejected by the advancing interface. However, when R is comparable to the rate of diffusion D_L/δ (where δ is the characteristic diffusion length) local equilibrium can no longer be maintained at the interface [50]. This deviation from equilibrium occurs as the solute atoms, in order to avoid being trapped by the advancing interface, diffuse ahead of the advancing interface; the more rapidly the interface advances the more difficult this becomes. If the interface is moving rapidly enough for there to be insufficient time for the solute atoms to diffuse away, these atoms must be taken up by the interface. This occurs because the incorporation of solute atoms in the interface requires only short-range atomic rearrangements, rather than the long range diffusion required for the atoms to escape. Thus, at these interface velocities, the advancing solidification front does not have sufficient time to rearrange the atoms in such a way as to ensure that the chemical potentials of the solid and of the liquid ahead of the interface are equal (as is required for equilibrium to be maintained at the interface). With increasing interface velocity the number of solute atoms able to escape from the advancing solidification front decreases, and hence the number of solute atoms taken up by the interface will increase. This increase in partition coefficient toward unity during solidification is termed solute trapping* (see e.g. [49]).

A number of models have been devised to describe the partition coefficient as a function of R [49, 51, 52]. The most widely applied of these models was developed by Aziz using an atomistic diffusional model at the solid-liquid interface, and solving the flux, continuity and thermodynamic equations associated with high interface velocities [52]. Aziz showed that for dilute alloys the velocity-dependent partition coefficient (k_v) is given by :

$$k_v = (k + \delta_i R/D_i)/(1 + \delta_i R/D_i) \qquad (2.8)$$

* The term solute trapping was originally applied only to situations where the chemical potential of the solute increases on solidification, but is now commonly used in any situation where the partition coefficient deviates toward unity from the equilibrium value, independent of the sign of the change in chemical potential.

where D_i is the interface diffusion coefficient and δ_i is a length of interatomic dimensions which characterises compositional rearrangement at the solid-liquid interface. From equation (2.8) it may be seen that when R = 0, $k_v = k$; when R = D_i/δ_i, k_v is the average of k and unity. At larger values of R the value of k_v increases rapidly to unity. Solute trapping is thus characterised by a rapid increase in the value of k_v at growth rates above the characteristic interface solute trapping velocity (R_{trap}):

$$R_{trap} = D_i/\delta_i \qquad (2.9)$$

At interface velocities in excess of R_{trap} solidification is partitionless, as the interface velocity is sufficient to overtake any compositional gradient in the liquid due to solute partitioning at the interface. The interface velocity dependence of the partition coefficient has been experimentally observed in a number of alloy systems (refer to the review by Jones [40]), although the lack of *a priori* measured values for δ_i limits the predictive capabilities of equation (2.8).

Partitionless solidification can, however, only occur if there is a thermodynamic driving force for the formation of a solid with the same composition as the liquid. This implies that there must be sufficient driving force to overcome the additional energy associated with the chemical potentials of the solid and liquid not being equal. These thermodynamic aspects of solute trapping were examined by Baker and Cahn [53]; the critical parameter to emerge from this study was the T_0 temperature, which is defined as the temperature at which the free energies of the solid and liquid phases are equal for a particular alloy composition. The value of T_0 as a function of alloy composition when plotted on the equilibrium phase diagram of the alloy system (fig. 2.4) indicates (by the definition of T_0) the locus of temperatures below which there is a thermodynamic driving force for the formation of solid with the same composition as the melt. This implies that, should the solidification of an alloy occur at a temperature below its T_0 temperature, there is a thermodynamic driving force for complete solute trapping or partitionless solidification. However, should solidification of an alloy occur at a temperature above its T_0 temperature, there is no thermodynamic driving force for partitionless solidification, and hence complete solute trapping is not thermodynamically allowed. The T_0 curve thus specifies the minimum undercooling required for partitionless solidification from the melt and marks the bound on solid compositions which can form from liquid of any composition at a particular

(a)

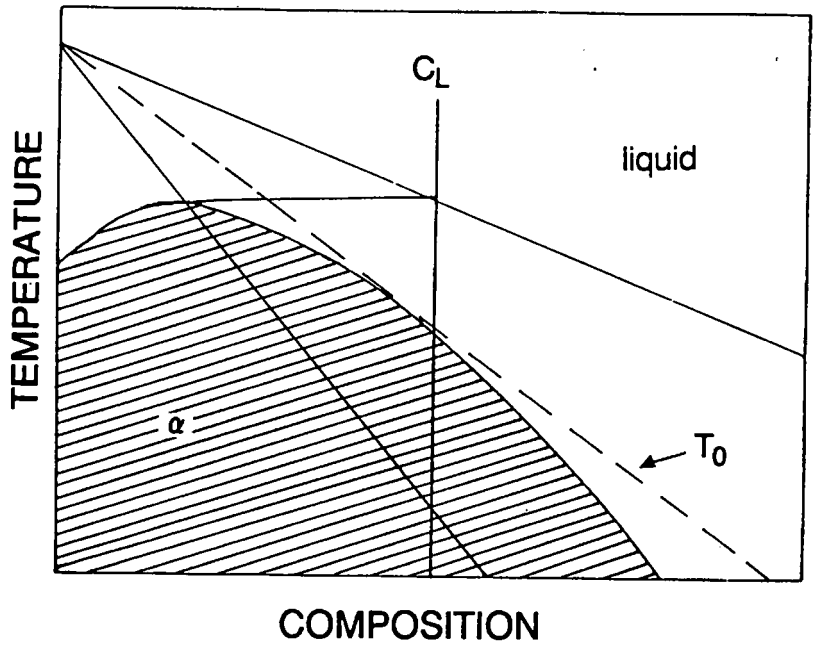

(b)

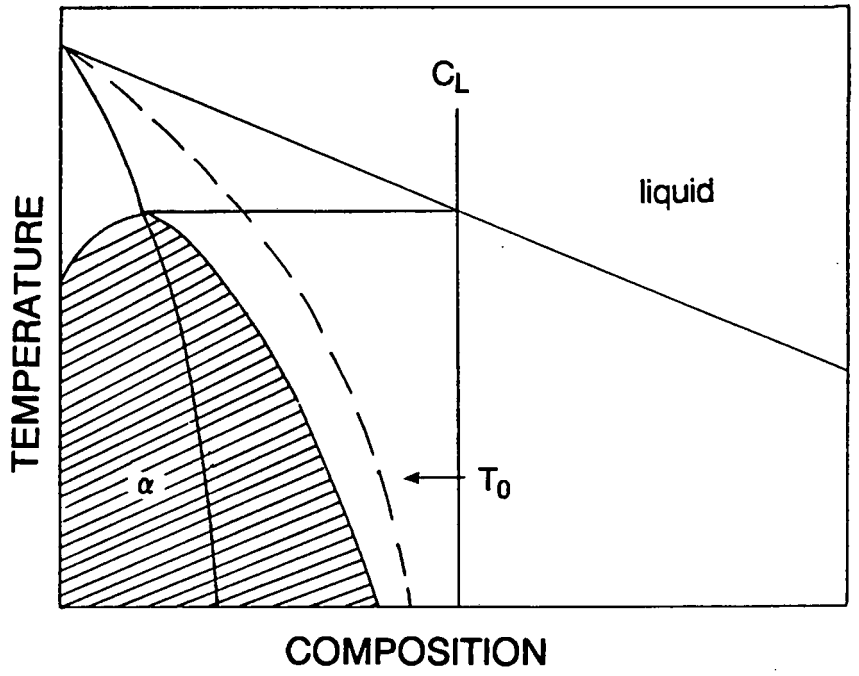

Fig. 2.4 Equilibrium binary phase diagrams showing the solid compositions which are allowed to form from a liquid of composition C_L. Also plotted on the diagrams is the T_0 temperature, the highest temperature at which the solid can form with the same composition as the liquid. In (a) partitionless solidification is thermodynamically possible, whilst in (b) partitionless solidification is thermodynamically precluded (after Boettinger *et al.* [66]).

temperature. However, should the free energy curves of the solid and liquid phases fail to intersect for a particular alloy composition, there is no thermodynamic driving force for the formation of solid of this composition, irrespective of the undercooling achieved (fig. 2.4(b)). In this case the T_0 temperature curve plotted on a phase diagram shows the bound for diffusionless solidification in which the solid and liquid can have the same composition, i.e. no solid can form with a composition at which the free energy curves of the solid and liquid phases fail to intersect no matter how rapidly cooled during solidification, unless local equilibrium ceases for the liquid phase itself [49]. Alloy compositions in which the free energy curves do not intersect have, on occasion, been associated with the formation of glasses (see e.g. [31, 54]).

(b) The influence of surface tension and the evolution of latent heat of solidification on interface stability.

In addition to the effect of interface velocity on the partition coefficient, the principle of constitutional supercooling does not take into consideration the additional solid-liquid interfacial energy associated with the formation of a protuberance at the interface. The change in free energy associated with the presence of a curved surface at the interface is given by (see e.g. [42]):

$$\Delta G_r = \nu_m \gamma K \qquad (2.10)$$

where ν_m is the molar volume of the solid, γ is the solid-liquid interfacial energy and K, the interface curvature, is given by:

$$K = 1/r_1 + 1/r_2$$

where r_1 and r_2 are the principal radii of the curved surface. The presence of an interfacial protuberance is thus associated with an increase in the solid-liquid surface energy and hence an increase in the free energy of the system. The inclusion of surface energy effects (also referred to as capillarity effects) in the modelling of morphological stability of the solid-liquid interface results in a greater stabilisation of the interface than predicted by the principle of constitutional supercooling.

The evolution of the latent heat of fusion can generally be ignored at low interface velocities. However, at high interface velocities it significantly influences the thermal

fields present at the interface. The liberation of the latent heat of fusion has a stabilizing influence on the morphology of the interface (see e.g. [31, 47, 49]).

In addition to ignoring these factors, the principle of constitutional supercooling did not attempt to rigorously solve the equations for the solute and thermal field at the solid-liquid interface. This has been done in the modern theory of interface stability (known as the perturbation theory, or linear stability criteria) which is briefly reviewed in this section, along with a discussion of the application of this theory to rapid solidification via CBMS.

(c) The perturbation theory of interface stability.

Beginning with the work of Mullins and Sekerka [55], a rigorous method of modelling solidification known as the perturbation theory of morphological stability (or linear morphological stability theory) has been developed. The theory was extended and discussed in more detail for rapid solidification by Coriell and Sekerka [56] and Cahn *et al.* [49]. In this theory a sinusoidal perturbation of initially infinitesimal amplitude is introduced on a planar solid-liquid interface and the stability of the interface ascertained by determining the growth or decay of the amplitude of perturbation. The perturbation introduced is of the form:

$$z = \epsilon \exp(\sigma t + i w_x x + i w_y y) \qquad (2.11)$$

where z is the direction of advance of the interface, $\epsilon \exp(\sigma t)$ is the perturbation amplitude, x and y are directions contained in the plane of the solidification front, w_x and w_y are the wave numbers (or spatial frequencies) of the perturbation. The range of wavelengths ($\lambda = 2\pi/(w_x^2 + w_y^2)^{1/2}$) over which the sinusoidal perturbations would be stable and grow for a particular combination of interface velocity and thermal gradient in the liquid are determined by rigorously solving the equations for heat transport and solute gradients at the interface. Assuming the partition coefficient k to be constant, and the solid-liquid interface to be isotropic, the criterion for the formation of a planar interface from the perturbation theory is given by ([55] as rearranged in [31]):

$$m_L G_C(\omega^*-R/D_L)/[\omega^*-(1-k)R/D_L] - T_M\gamma\omega^2/(\Delta H_f\rho_S) - (k_S G_S+k_L G_L)/[(k_S+k_L)] < 0 \quad (2.12)$$

always > 0 (solute field); always < 0 (capillary force); < 0 or > 0 (thermal field)

where $\omega^* = R/2D_L + [(R/2D_L)^2 + \omega^2]^{1/2}$, $\omega^2 = \omega_x^2 + \omega_y^2$, T_M is the melting point of the interface in the absence of solute and curvature, ΔH_f is the latent heat of fusion per unit mass, ρ_S is the solid density, k_S and k_L are the thermal conductivities of the solid and liquid respectively and G_S is the temperature gradient in the solid at the solid-liquid interface. Equation (2.12) is separable into a solute field term which is always destabilizing, a capillarity field term which is always stabilizing and a thermal field term which is stabilizing provided that the nett heat flow is into the solid during solidification (i.e. $G^* = (k_L G_L + k_S G_S)/(k_L + k_S) > 0$) [56]. Thus, provided that heat flow is into the solid during solidification, interfacial instability occurs when the destabilizing solute gradient term is sufficiently large to overcome the stabilizing influence of the temperature gradients and capillarity. In the linear stability criteria (unlike the principle of constitutional supercooling) small negative values of G_L will not necessarily result in morphological instability, provided that G_S is sufficiently positive to ensure that the thermal field term is positive.

At low interface velocities, provided that ΔH_f is small, the criteria for the formation of a planar interface in equation (2.12) are similar to those predicted from the principle of constitutional supercooling (equation (2.7)) but with G_L replaced by G^* [55, 56]. This has the effect of slightly increasing the amount of interfacial stability predicted at low interface velocities [56]. At high interface velocities, however, the predictions of the perturbation theory differ considerably from those of the principle of constitutional supercooling. The theory predicts that, at growth rates above a critical value known as the absolute interface velocity (R_{abs}), the interface will be stable for perturbations of all possible wavelengths [55]. At high interface velocities there is a limited amount of time available for diffusion of the solute in the liquid and hence a limit to the distance the solute atoms can diffuse. The higher the interface velocity, the less lateral segregation of the solute in the liquid can occur and as a result the shorter the wavelengths of the stable perturbations. The range of wavelengths over which the interface is morphologically unstable thus decreases with increasing interface velocity. The formation of small wavelength perturbations, however, requires a large increase in solid-liquid interfacial surface area and hence a large increase in interfacial energy. At

growth velocities above R_{abs} the perturbation wavelengths permitted by diffusion requirements are so short that their formation is prohibited by surface energy considerations and hence the interface is morphologically stable. The threshold velocity (R_{abs}) that must be exceeded for absolute stability of the interface is given by [55]:

$$R_{abs} = \Delta T_0 D_L / k\Gamma = m_L D_L (1 - k) C_0 / k^2 T_m \Gamma \qquad (2.13)$$

where ΔT_0 is the alloy freezing range, Γ is the Gibbs-Thomson coefficient. When R exceeds R_{abs} the interface is predicted to be planar.

The morphological stability of the solidification front (from the perturbation theory) as a function of R and G_L (i.e. neglecting G_S) is shown in fig. 2.5 [56, 57]. A comparison between fig. 2.3 (the morphological stability predicted by the principle of constitutional supercooling) and fig. 2.5 shows that the extent of planar-front solidification predicted by the morphological stability theory is considerably larger than that predicted by the constitutional supercooling criteria. The practical predictions of the perturbation theory, and in particular the existence of R_{abs}, have been extensively investigated experimentally (see Jones [40] for review); although absolute stability has been observed in a number of alloy systems, the predictive value of the theory is severely hampered by a dearth of independently determined material constants. The predictions of the theory and the interpretation of microstructures purported to support the perturbation theory have, however, been questioned by Laxmanan [58], although his interpretation of the evidence has not been widely accepted.

In the above discussion only the limit of stability has been estimated - nothing has been said about the form and scale of perturbations which develop if the interface is unstable. While the steady state growth of dendrites or cells is a complex field which falls beyond the scope of this review (for a recent review see [43]), the scale of the initial perturbation which forms at the unstable interface and the subsequent instability of the dendrite tip region are readily considered by means of the perturbation theory. Both the scale of the perturbation and the instability of the dendrite tip will influence the rate of advance of the interface and the scale of the final microstructure. However, these perturbations are only transient and will disappear once a steady state cellular or dendritic morphology is established.

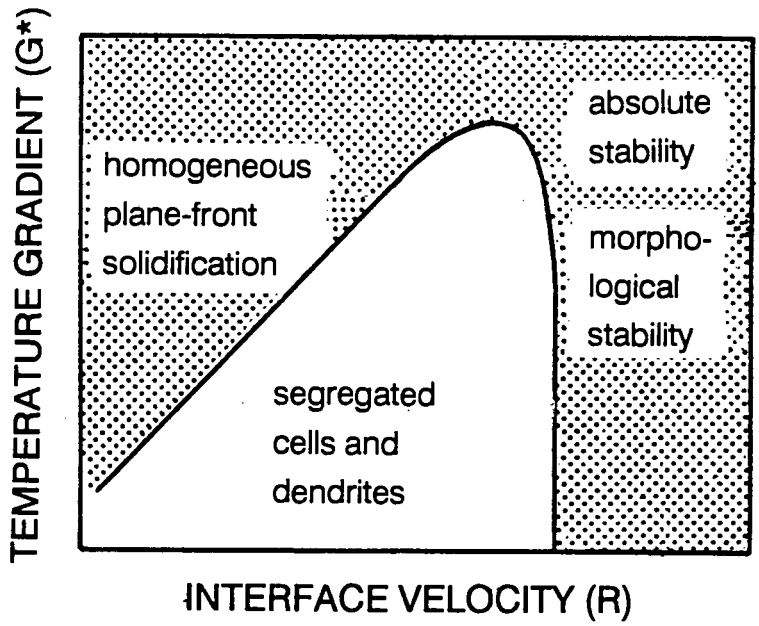

Fig. 2.5 The morphology of the advancing interface as a function of temperature gradient at the interface (G*) and interface velocity (R) as predicted by the morphological stability criteria (after Mehrabian [31]).

In order to most efficiently reject solute at its tip a dendrite would be expected to assume as sharp a geometry as possible (see e.g. [42]); the minimum sustainable dendrite tip radius is therefore expected to be the critical radius of nucleation. However, Langer and Müller-Krumbhaar [59, 60] have shown that in practice dendrite tips grow with a radius approximately equal to the wavelength of the shortest wavelength perturbation for which the interface is unstable. This value of λ is known as the critical wavelength for interface instability and is given by [61]:

$$\lambda_i = 2\pi (D_L\Gamma/R\Delta T_0)^{1/2} \qquad (2.14)$$

where ΔT_0 is the alloy freezing range (i.e. $m_L C_0(1 - k)/k$; refer to fig. 2.2(c)). Although this relationship has been superseded by a solvability criteria [62, 63] the fundamental relationship remains the same. By solving for λ_i under conditions where the heat flow is into the solid, Kurz *et al.* [61] determined the dendrite tip radius (r_d) as a function of tip velocity (R). A typical calculated plot of r_d against R is shown in fig. 2.6. Assuming k to

be constant, the dendrite tip radius (equal to λ_i) decreases with increasing interface velocity (as would be expected from equation (2.14)). However, from fig. 2.6 it may be seen that with increasing tip velocity there is a minimum achievable tip radius, and that at tip velocities above this value the tip radius increases rapidly. This minimum is a result of the effect of capillarity and lateral solute segregation on the value of λ_i. In practice, at tip velocities approaching this minimum value the solidification microstructure changes from dendritic to cellular (see e.g. [64]); the current theories concerning the formation of these cellular structures has been critically reviewed by Laxmanan [65]. Recent work has shown that a good correlation exists between the theoretically predicted dendrite (or cell) tip radius (r_d) with R at velocities approaching R_{abs} (refer to equation (2.14)) and experimentally observed values (for review see Jones [40]).

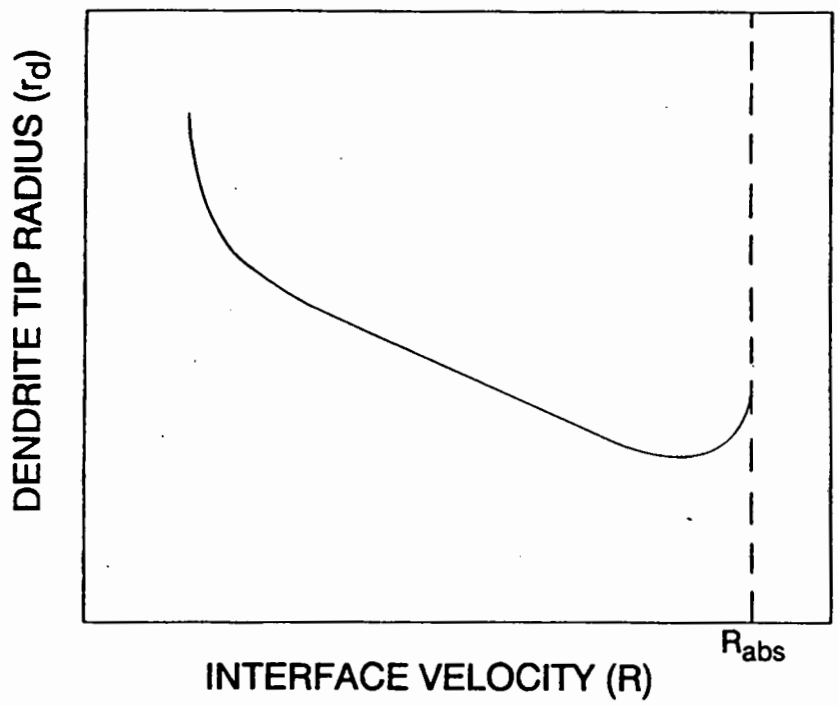

Fig. 2.6 Dendrite tip radius (r_d) as a function of interface velocity (R) from linear stability analysis (after Kurz *et al.* [61]).

Depending upon the nucleation characteristics of the melt, the rapid advance of the solid-liquid interface during rapid solidification occurs either as a result of a large undercooling of the melt prior to solidification, or as a result of rapidly moving temperature fields (see e.g. [42, 66]). Thus rapid solidification via CBMS may result in the melt being considerably undercooled prior to solidification commencing. The growth rate which will produce a morphologically stable interface in an undercooled melt has been shown to be given by [42]:

$$R_{abs} = (R_{abs})_c + (R_{abs})_t \qquad (2.15)$$

where $(R_{abs})_c$ is given by equation (2.13) and

$$(R_{abs})_t = a\theta_t/\Gamma$$

where a is the thermal diffusion coefficient, $\theta_t = \Delta h_f/C$, Δh_f is the volumetric heat of fusion and C is the volumetric specific heat. Solidification into an undercooled melt thus introduces an additional term into the equation for absolute interface velocity. For metals this $(R_{abs})_t$ term is generally considerably larger than $(R_{abs})_c$ as the thermal diffusion coefficient (a) is much larger than D_L. Consequently, the morphological stabilisation of the growth front during solidification from undercooled alloy melts occurs at a much higher interface velocity than when the heat flow is into the solid; the calculated dependence of the tip velocity (R) is shown in fig. 2.7(a) [67]. Thus the modern theory, unlike the principle of constitutional supercooling, predicts that the interface can be stable during solidification into an undercooled melt. The increasing interface velocity with increasing undercooling results in the dendrite tip radius decreasing with increasing undercooling until (Rabs)c is reached, whereafter the behaviour becomes more complex due to the change from almost purely solute diffusion controlled to a mixed solute and thermal diffusion control: the behaviour is illustrated in fig. 2.7(b) [68].

Rigorously solving the solute and thermal fields thus results in a much greater stability of the interface than is predicted by the principle of constitutional supercooling. However, implicit in the preceding discussion is the assumption that the evolution of latent heat at the solid-liquid solidification front does not substantially change the thermal conditions at the interface as a function of time. This assumption is not generally valid during rapid solidification by CBMS; the implications of this are

discussed in the next section.

(a)

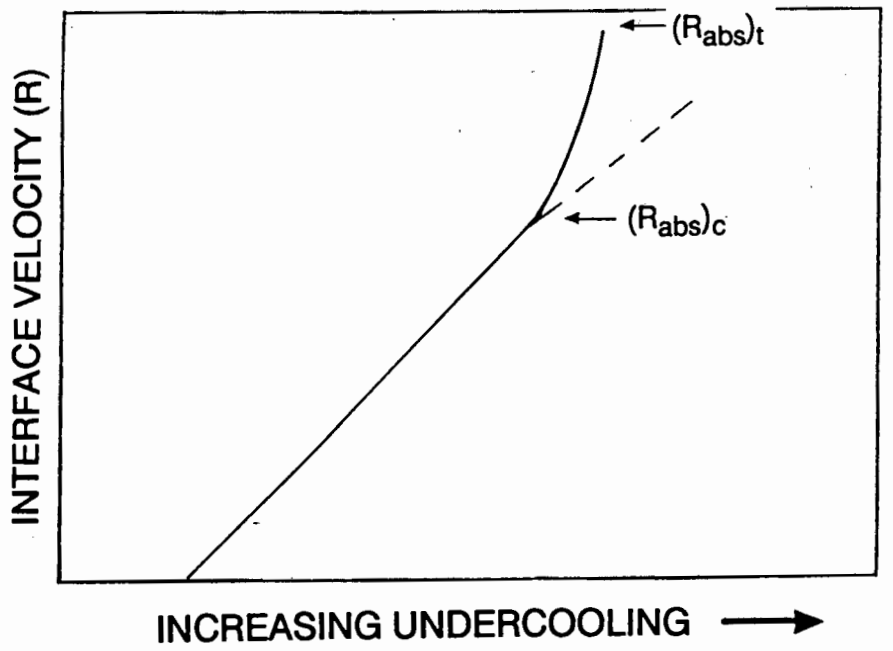

(b)

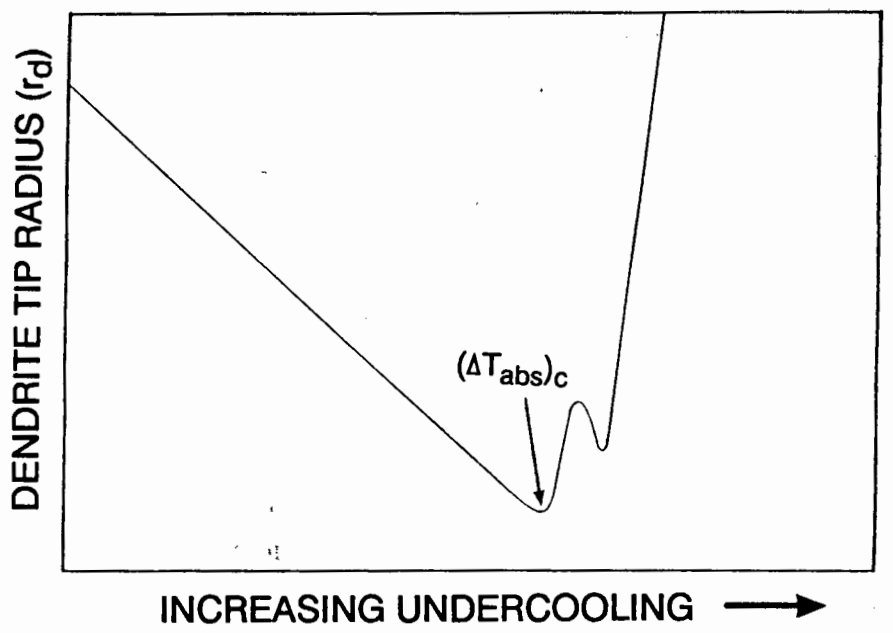

Fig. 2.7 The calculated dependence of (a) the dendrite tip velocity (R) and (b) the dendrite tip radius (r_d) on the undercooling in the melt (after Lipton *et al.* [67]).

(d) Microsegregation during rapid solidification by means of CBMS.

A number of studies have shown that an undercooling of up to a few hundred degrees is achieved in the melt during CBMS prior to the commencement of solidification (see e.g. [11]). On the basis of the preceding discussion on solidification in an undercooled melt, the conditions prevalent during CBMS should result in the formation of dendrites. In practice, the microstructures of CBMS ribbons often consist of segregation-free columnar grains extending for much of the ribbon thickness. Should microsegregated regions be present, these tend to occur in the areas of the ribbon which were most distant from the wheel surface during solidification (see e.g. [11]). The presence of these columnar grains is believed to be associated with absolute stability at high interface growth rates and suggests that, in spite of considerable undercooling achieved in the melt, the temperature gradient ahead of the interface during solidification is either positive or slightly negative (but with the heat flow into the solid during solidification, i.e. $G^* > 0$) [69].

The latent heat liberated during CBMS is dissipated both into the wheel surface and into the supercooled melt. The former results in a negligible rise in the temperature of the wheel (see e.g. [41]). However, the flow of heat into the melt results in a considerable increase in ribbon temperature. During CBMS heat flow is generally near-Newtonian (see section 2.1) and therefore the rate of heat removal from the ribbon is determined by the resistance to heat flow across the ribbon-wheel interface. A schematic illustration of the ribbon temperature of a pure material as a function of time under Newtonian heat flow conditions during solidification is shown in fig. 2.8 [28]. The figure shows that prior to the commencement of nucleation the melt is supercooled to a temperature T_N below the equilibrium melting point T_M. Once solidification has commenced, recalescence results in a dramatic increase in the ribbon temperature due to the rapid evolution of latent heat. The rate at which the latent heat is liberated at the interface is proportional to the interface velocity, which is itself inversely dependent on the interface temperature (see e.g. [70, 71]). Thus, during the initial stages of solidification the rate of evolution of latent heat is high and results in a dramatic increase of the ribbon temperature from T_N to T_G. The increase in ribbon temperature results in a decrease in interface velocity with time until temperature T_G is reached. At this temperature the system is at steady state as the ribbon (and melt) temperatures have increased to a value at which the heat liberated at the interface is dissipated almost exclusively through the substrate-ribbon interface and solidification proceeds

isothermally (the amount of heat lost by radiation at the ribbon-air interface is normally negligible [72]). Assuming that all of the heat liberated during the initial stages of recalescence is taken up by the ribbon, the fraction of the ribbon cross-sectional thickness solidified from nucleation to the commencement of steady state growth is given by $C'\Delta T_N/\Delta H_f$, where C' is the ribbon specific heat modified to allow for the evolution of the latent heat of solidification and ΔT_N is the nucleation undercooling $(T_M - T_N)$ [28].

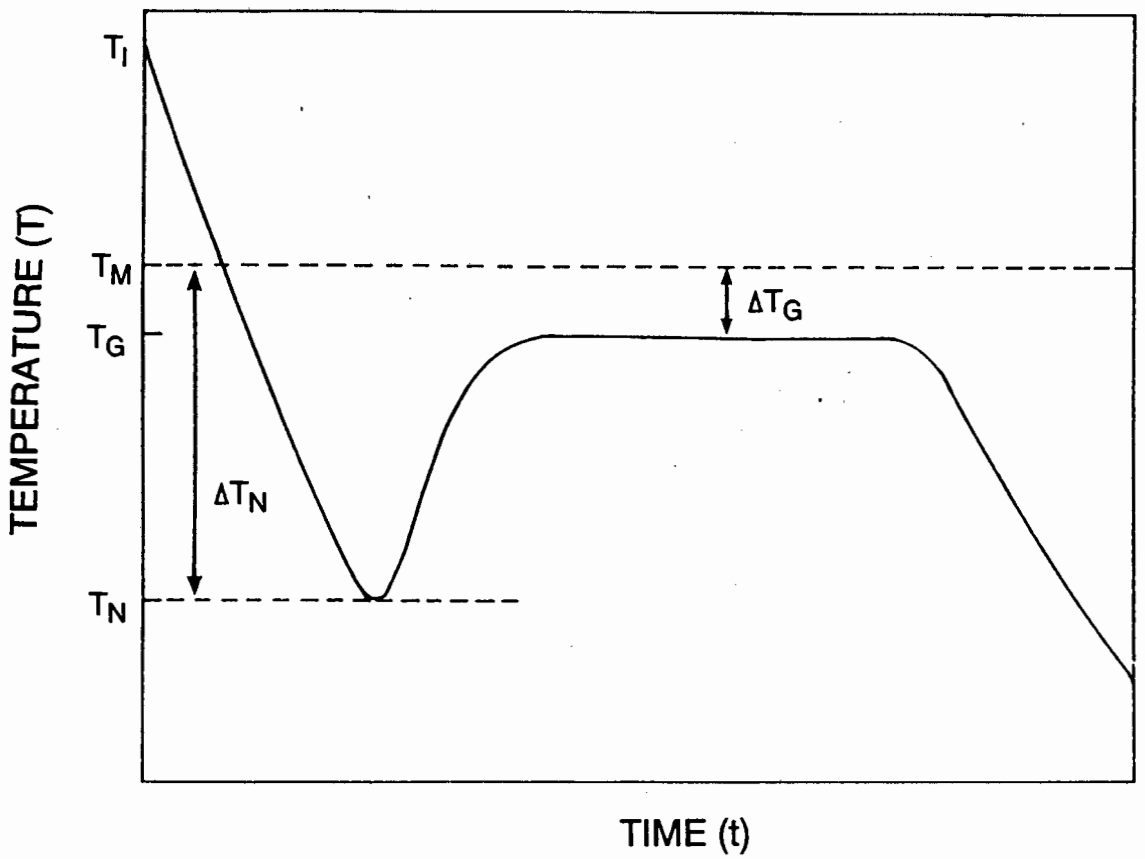

Fig. 2.8 Schematic graph showing the ribbon temperature as a function of time during CBMS of a pure material under Newtonian heat flow conditions; T_I is the initial temperature of the melt, T_N is the temperature at which nucleation occurs, T_G is the ribbon temperature when steady state is achieved and T_M is the equilibrium solidification temperature of the material (after Cantor *et al.* [28]).

Non-Newtonian heat flow conditions during solidification would imply that the resistance to heat flow is not only determined by the ribbon-substrate heat transfer coefficient (h), but is also dependent upon the resistance to heat flow in both the melt and solid, and results in thermal gradients in both of these. The effect of this resistance on heat flow would be to concentrate the latent heat evolved in the region of the interface [28, 72]. As there is considerable undercooling in the melt prior to nucleation, the inhibition of the flow of latent heat from the interface may result in the formation of a temperature inversion ahead of the solid-liquid interface (i.e. negative thermal gradient in the liquid) and consequently in the formation of thermal dendrites at the interface [28].

The effect of the dependence of the partition coefficient on the interface velocity (equation (2.8)) is only significant at interface velocities of approximately R_{trap} (equation (2.9)). Solute trapping is thus only significant at relatively high interface velocities and of importance only during the initial stages of solidification. Should the interface velocity fall below that of the absolute interface velocity (equation (2.13)) during solidification, cellular or dendritic breakdown of the interface will occur, with the associated formation of a microsegregated microstructure.

Few studies have been performed to test the validity of solidification theory with experimental results during CBMS. In a recent study, however, Chu and Granger [73] studied the scale of microsegregation in dilute Al-Fe alloys (prepared by CBMS) and compared it to that predicted theoretically for solidification in an undercooled melt [67]. The Al-Fe system was in many respects atypical of CBMS microstructures as segregation occurred through the entire thickness of the ribbon and the assumption of nett heat flow into the melt was therefore possibly justified. As shown previously in fig. 2.7(b), the tip radius of a dendrite growing into an undercooled melt increases with decreasing undercooling, thus the decreasing undercooling of the melt associated with recalescence during solidification is expected to be accompanied by an increase in tip radius (and hence in the scale of microsegregation) as a function of distance from the wheel surface. Once recalescence is complete and steady state is reached, the tip radius should remain approximately constant for the remainder of the solidification of the ribbon thickness. Chu and Granger were able to observe the expected initial coarsening of segregation as a function of distance from the wheel surface followed by a fairly uniform segregation pattern formed once steady state was achieved. Somewhat surprisingly, however, they found no evidence of solute trapping, although the diffusive

velocity of the solute in the melt had apparently been exceeded by the interface velocity. Nevertheless, their study offered experimental support for the theoretical predictions of Lipton *et al.* [67].

Thus the effect of the evolution of latent heat at the solid-liquid interface during CBMS is to change the conditions at the interface as a function of distance from the wheel-side surface of the ribbon. As a result the stability of the interface (and hence the degree and scale of segregation) may be dependent upon position in the ribbon. Nevertheless, the modern theory of interface stability predicts solute trapping and the refinement of segregation during rapid solidification by CBMS.

2.2.2 The Effect of Rapid Solidification on Grain Size

In addition to reduced solute segregation, rapid solidification is associated with a considerable refinement of grain size. Only the refinement resulting from rapid solidification by means of CBMS will be considered here; for a more general review of the current understanding of the effect of rapid solidification on grain size see Greer [69].

It is generally found that the microstructures formed by melt spinning consist of a fine equiaxed zone at the chill surface with columnar grains extending from this region across the ribbon thickness (see e.g. [13, 99]). These columnar grains form from the melt by the heterogeneous nucleation of solid on the wheel surface, followed by lateral growth until the entire wheel surface is covered. The grains then continue to grow into the melt in a columnar fashion until they occupy the entire ribbon thickness [28]. As a limited amount of competitive growth occurs during the solidification of the columnar grains, coarsening of the these grains occurs across the ribbon thickness. However, Cantor and co-workers [28, 74] have shown that the grain size in melt spun ribbons is determined primarily by the competition between the rate of nucleation at the wheel surface and the lateral growth of the nucleated grains. Modelling of this phenomena predicts that the natural logarithm of the grain size (ln d) is inversely proportional to the square of the cooling rate (dT/dt) which is proportional to the wheel speed (V_s) (see section 2.1.1) i.e.

$$\ln d \propto 1/(dT/dt)^2 \propto 1/V_s^2 \qquad (2.16)$$

Cantor and his co-workers have shown that such a correlation was manifested experimentally in the size of the columnar grains adjacent to the wheel surface. A more recent model by Greer [69] of grain size as a function of cooling rate during CBMS regarded heterogeneous nucleation at the wheel surface as the primary factor determining the grain size and yielded the expression:

$$d \propto 1/(dT/dt) \propto 1/V_s \qquad (2.17)$$

Cantor's data for grain size as a function of cooling rate, when plotted using the above relationship, was again found to yield a satisfactory correlation. Greer argued that nucleation was the dominant factor, as a large undercooling is known to occur at the interface during CBMS and the nucleation rate is more sensitive to undercooling than lateral growth.

2.2.3 Metastable Phase Formation

Metastable phase formation has been the subject of theoretical and experimental interest for an extended period of time (see e.g. [75, 76]). Rapid solidification has been of considerable interest in the study of metastable phase formation, as it has been shown to produce structures which are further from equilibrium than is possible using more conventional processing techniques [7, 76] such as metallic glasses and missing Hume-Rothery electron phases (for examples see [77]). For general reviews of metastable phase formation via rapid solidification see e.g. Jones [7] and Turnbull [76].

There is, as yet, no comprehensive theory which can predict the formation of metastable phases, and thus much of the present understanding of the formation of metastable phases is either empirical or semi-empirical [75]. A number of different types of metastability are known; in order to discuss possible metastable phase formation in Au-Ti alloys an appreciation of the alloy system is required. In the sections that follow the Au-rich portion of the Au-Ti phase diagram is reviewed, followed by an in-depth review of the metastable structural order which has been noted in related alloy systems on quenching from high temperatures.

2.3 THE Au-Ti ALLOY SYSTEM

2.3.1 The Au-Ti Equilibrium Binary Phase Diagram

The Au-rich portion of the Au-Ti equilibrium phase diagram is shown in fig. 2.9(a) [78]. The figure shows that Ti has a maximum solubility of 3.5wt.% (13at.%) at 1123°C in the terminal α f.c.c. solid solution. The equilibrium solubility of Ti declines rapidly with decreasing temperature to approximately 0.62wt.% (2.5at.%) at 500°C and subsequently to 0.25wt.% (0.1at.%) at 350°C [79]. At Ti contents above these solubility limits the long-range-ordered intermediate phase, Au_4Ti, is reported to be in equilibrium with the α solid solution. Au_4Ti is isostructural with Ni_4Mo with space group ($I4/m$) and Strukturbericht designation D1a; the crystal structure is shown in fig. 2.9(b). The Bravais lattice is ordered body centred tetragonal (b.c.t.), and may be generated from the f.c.c. parent matrix by replacing every fifth $(420)_{f.c.c.}$ plane of Au-atoms with a layer of Ti atoms (see fig. 2.10) [80]. A view of the ordered Au_4Ti structure along [001] for the case where the c-axis of the long-range-ordered structure is oriented to coincide with the $[001]_{f.c.c.}$ cube axis is shown in fig. 2.10(a) and (b) [81]. As is apparent, for a given choice of c-axes the Au and Ti atoms can be arranged in two distinct ways; the two arrangements are related by an anti-parallel twin relationship [82]. The presence of both of these orientational variants generates a characteristic octahedral motif of superlattice reflections between the parent f.c.c. reflections in [001] zone-axis electron diffraction patterns (fig. 2.11(a)); the two in-plane orientational variants are distinguished for clarity.

Orientating the c-axis of the b.c.t. structure along either the $[010]_{f.c.c.}$ or $[100]_{f.c.c.}$ directions generates additional distinguishable orientational variants of the structure. The six orientational variants (two for each c-axis direction) generated by the insertion of layers of Ti atoms constitute the total number of distinguishable orientational variants of the (D1a) Au_4Ti structure (see e.g. [81]). The three-dimensional reciprocal lattice of the fully ordered D1a structure containing all six orientational variants is shown in fig. 2.11(b).

Thus, at equilibrium, dilute Au-Ti alloys possess a long-range-ordered (D1a) Au_4Ti phase. A number of other alloy systems which at equilibrium possess a long-range-ordered phase with a D1a structure form, on quenching from high temperatures, a

(a)

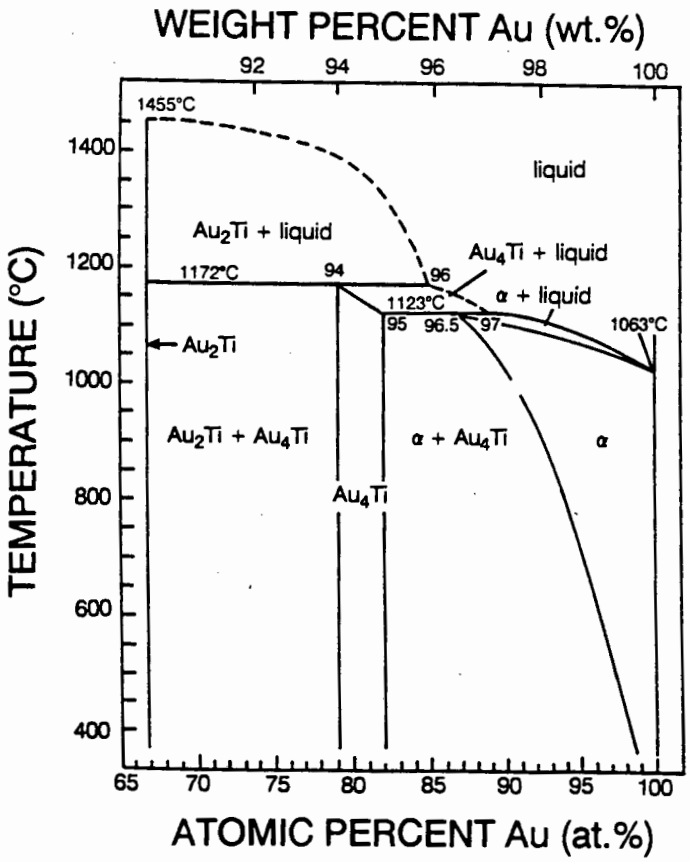

(b)

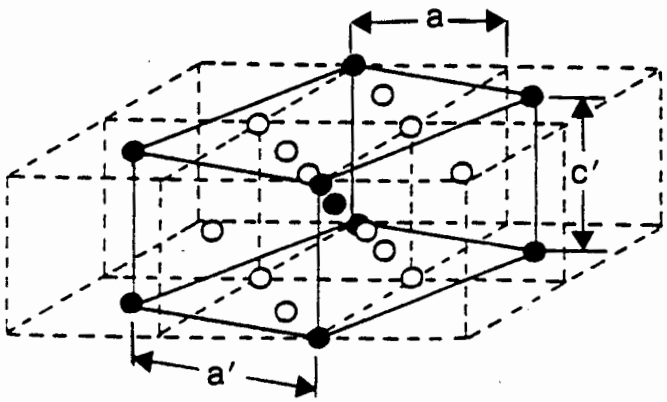

Fig. 2.9 (a) The gold-rich region of the Au-Ti equilibrium binary phase diagram (after Murray [78]). (b) The crystal structure of the long-range-ordered (D1a) Au_4Ti phase; the positions of the Au atoms are indicated by unshaded circles while the positions of the Ti atoms are indicated by shaded circles (after Dutkiewicz and Thomas [80]).

metastable state of order known as "special-point" order. The existing literature covering prior research on this state of order is reviewed in the following section.

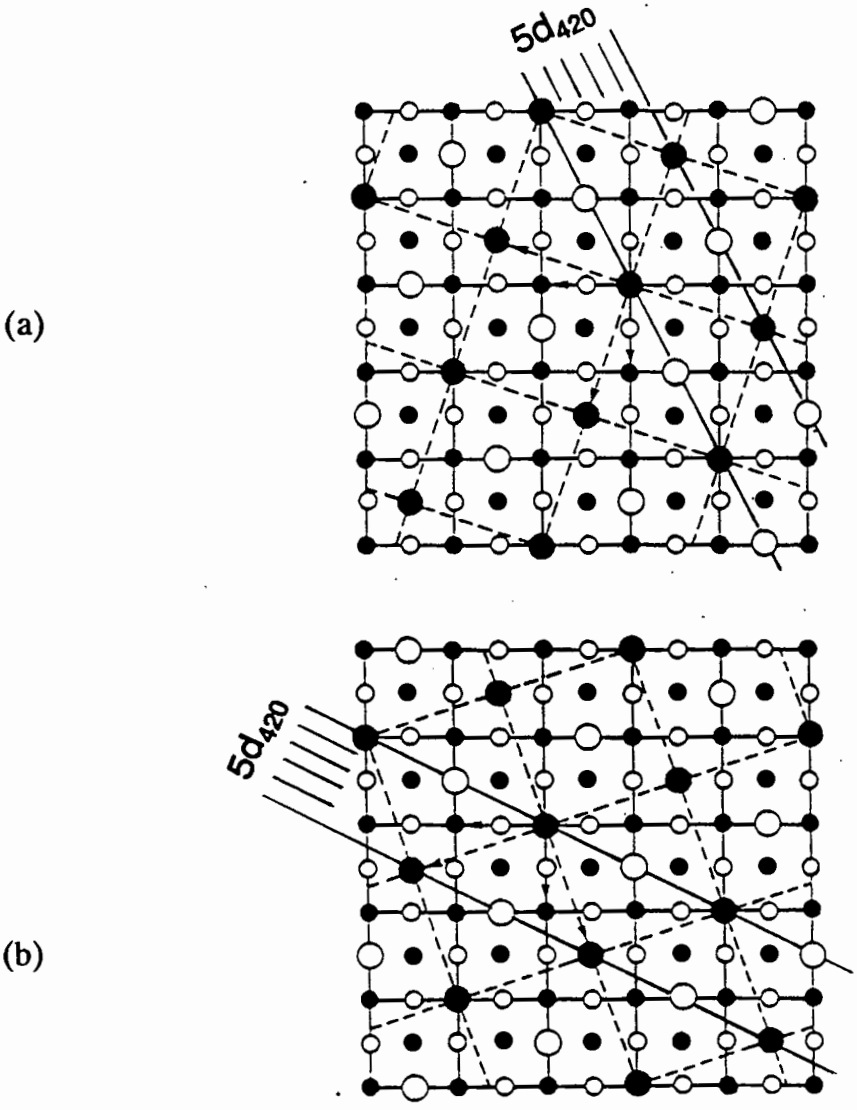

Fig. 2.10 Schematic illustration of the atomic arrangement in the (110) plane of the (D1a) Au_4Ti phase showing two distinct orientational variants of the structure ((a) and (b)). The large circles indicate the positions of the Ti atoms, the small circles the positions of the Au atoms; the shaded circles are situated in the zeroth layer and the unshaded circles are in the $^1/_2$ layer. The b.c.t. unit cell is outlined by the dashed lines (after Okamoto and Thomas [81]).

(a)

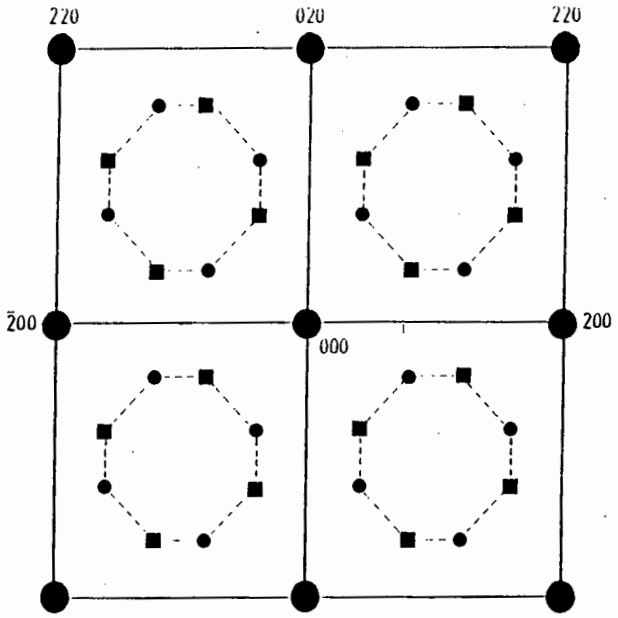

(b)

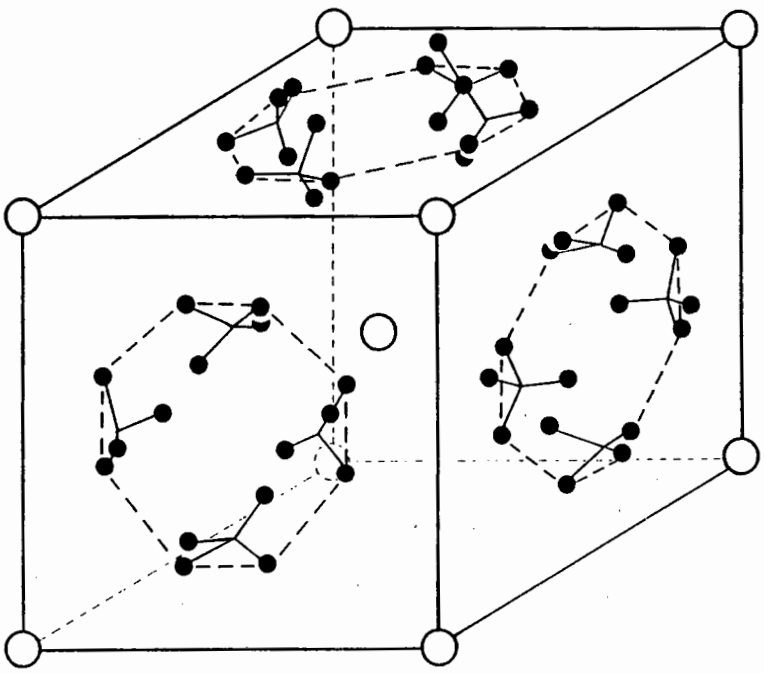

Fig. 2.11 (a) Schematic indexed [001] zone-axis diffraction pattern showing the orientation relationship between the α (f.c.c.) matrix (●) and two orientational variants (● and ■) of the (D1a) Au_4Ti phase. (b) A schematic three-dimensional representation of the reciprocal-lattice reflections arising from the presence of all possible variants of the long-range-ordered (D1a) structure (●) together with reflections from the f.c.c. lattice (◯). The faces of the cube represent zero-order reciprocal lattice planes of the f.c.c. structure; off-plane reflections from some D1a variants are evident.

2.3.2 Metastable Phase Formation in Alloy Systems Related to the Au-Ti System

Metastable phase formation in alloys which are long-range-ordered at equilibrium, but which have been quenched from high temperatures, has been extensively studied; for reviews see Khachaturyan [83] and de Fontaine [84]. A number of alloy systems which possess an equilibrium long-range-ordered (D1a) structure - namely Ni_4Mo, Au_4Cr and Au_4V - have, on quenching from high temperatures, been shown to possess a transitional metastable state of order known as $<1^1/_20>$ special-point order [85, 86, 87]. At high temperatures these alloys exist as random substitutional solid solutions and, on cooling slowly to room temperature, the equilibrium long-range-ordered phase forms. However, rapid quenching from high temperatures can suppress the formation of the equilibrium phase, in which case the resulting state of order may be characterised by the presence of diffuse diffracted intensity maxima in electron diffraction patterns at the $1^1/_20$ reciprocal lattice positions [88]†.

The state of order giving rise to $<1^1/_20>$ special-point order has been described by de Fontaine [89] using the static concentration wave formalism. This approach to structural order in solid solutions describes the order present by means of a series of static concentration waves, which characterise the local variation of the probability of finding a particular atomic species on a specific lattice site. On the basis of Khachaturyan's mean-field free energy model [90], de Fontaine has shown that the behaviour of a system where fully developed long-range order is absent (i.e. at high temperatures and during the early stages of ordering) is governed by the second-order term of a Taylor series expansion expressed in terms of concentration wave amplitudes. This second-order term contains the Fourier transform of the pair interaction function which, for symmetry reasons, has its minima at so-called special-points of the reciprocal lattice. Special-points occur at positions in reciprocal space where two or more symmetry elements intersect. For the f.c.c. structure, one such special-point is located at the $1^1/_20$ reciprocal lattice position. A minimum in the Fourier transform of the pair interaction parameter thus occurs for a particular wave vector (described by the special-point) and corresponds to a minimum in the free energy of the system. De Fontaine suggested that as a result, at high temperatures and during the early stages of ordering, systems showing special-point order minimise their free energy by forming concentration waves with the $<1^1/_20>$ special-point wave vectors. He then showed,

† The convention $1^1/_20$ is used to signify a position in reciprocal space with particular reference to the f.c.c. structure, whereas $<1^1/_20>$ is used to refer to this particular type of special-point order.

using Landau's criteria [91], that the formation of $<1^1/_20>$ concentration waves occurs via a second-order transformation, whilst the formation of the long-range-ordered (D1a) phase occurs via a first-order transformation, i.e. via nucleation and growth. De Fontaine subsequently introduced the concept of the ordering spinodal temperature, below which the alloy would be unstable with respect to the formation of special-point order. This implies that on quenching, provided the nucleation of the long-range-ordered (D1a) phase is suppressed, $<1^1/_20>$ concentration waves will form and will be amplified as the temperature decreases below that of the ordering spinodal temperature.

The concentration wave approach translates conveniently to a reciprocal space interpretation; for every concentration wave there is a corresponding superlattice reflection, the intensity of which is dependent upon the amplitude of the associated concentration wave. The presence of $<1^1/_20>$ concentration waves in a particular alloy may thus be characterised by the presence of diffuse reflections at the $1^1/_20$ reciprocal lattice positions. A schematic [001] zone-axis electron diffraction pattern illustrating the relative positions of reflections due to the $<1^1/_20>$ special-point order, the equilibrium (D1a) long-range order, and the fundamental f.c.c. reflections is shown in fig. 2.12(a). However, the concentration wave description of structural order does not lend itself readily to real space interpretation, as descriptions of atomic distributions are couched in terms such as "occupation probabilities" and as a result the real space interpretation of $<1^1/_20>$ special-point order has been the subject of considerable controversy in the recent past [92, 93].

Okamoto and Thomas [81] have suggested that the $1^1/_20$ reflections, which are characteristic of special-point order, can be explained by the presence of imperfectly ordered domains of DO_{22} structure containing non-conservative anti-phase boundaries. The DO_{22} structure is body-centred tetragonal and may be generated from the f.c.c. parent phase by replacing every fourth $(420)_{f.c.c.}$ plane by a layer of minority atoms. There are three distinguishable orientational variants of the DO_{22} structure relative to the parent f.c.c. structure, one with its c-axis parallel to the $[001]_{f.c.c.}$ zone-axis and two with their c-axes perpendicular to this orientation. As illustrated in fig. 2.12(b), the 101 and 103 first-order reflections of the variants with their c-axes perpendicular to the zone-axis orientation may be used to generate the characteristic $1^1/_20$ special-point reflections illustrated in fig. 2.12(a). However, the second-order 202 and 002 reflections from these variants of the DO_{22} structure are absent in diffraction patterns from

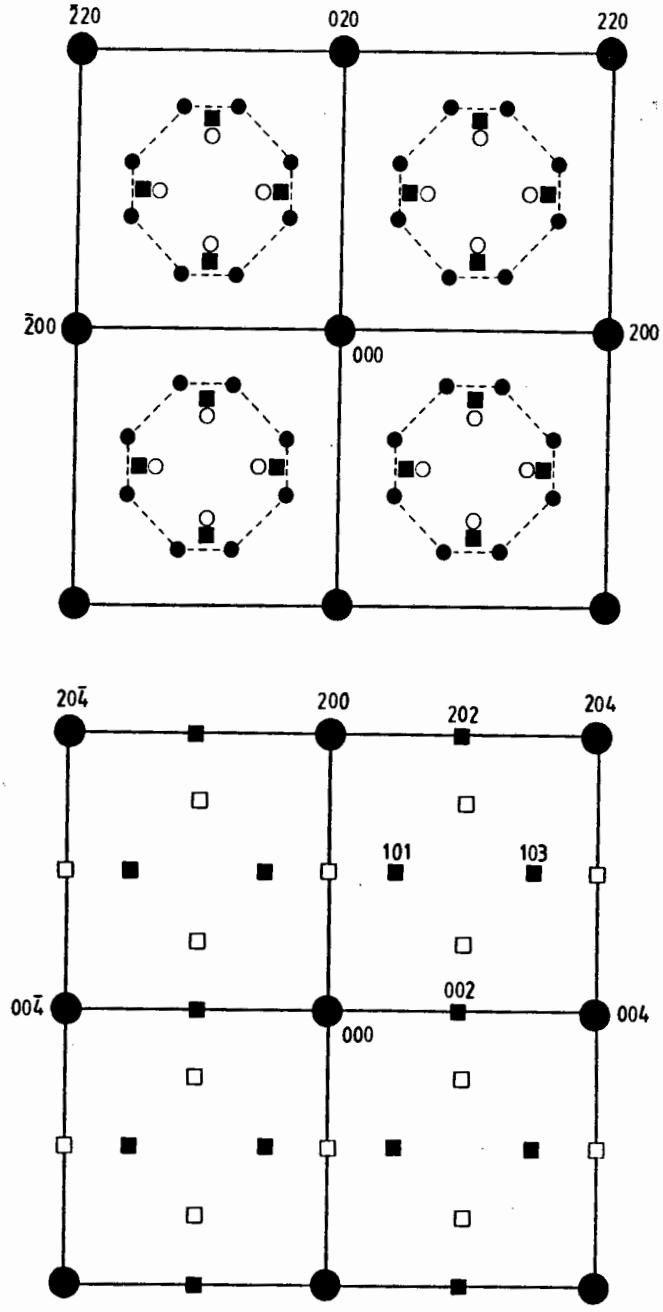

Fig. 2.12 Schematic representation of [001] zone-axis diffraction patterns showing the positions of all reflections expected to arise from the structures associated with special-point order. (a) Parent f.c.c. matrix reflections (●), $<1^1/_20>$ special-point order reflections (■) and long-range order (D1a) Au_4Ti reflections (•). The projected D1a out-of-plane reflections are indicated by (○). (b) Parent f.c.c. matrix reflections (●), the shaded and unshaded squares (■ and □) represent reflections from two distinguishable orientational variants of the DO_{22} structure, with a common c-axis, arising from precipitates (after Van Tendeloo [92]).

structures exhibiting $<1^1/_20>$ special-point order. Okamoto and Thomas suggested that the absence of these second-order reflections was due to the presence of non-conservative anti-phase boundaries parallel to the $\{420\}_{f.c.c.}$ planes in the DO_{22} structure. An alternative approach was used by Van Tendeloo *et al.* [92], who suggested that anti-phase boundaries in the DO_{22} structure could be created by the insertion of slabs of the D1a structure into the {110} planes of the DO_{22} phase. The use of imperfectly ordered microdomains in the description of special-point order was, however, dismissed by Stobbs and Stobbs [93] as being somewhat artificial and potentially misleading, since there exists no direct evidence for their presence. They preferred a concentration wave approach, but with the concentration waves attenuated into concentration wave packets.

A real space interpretation of special-point order using the cluster variation approach due to Kikuchi [94] was suggested by de Ridder, Van Tendeloo and Amelinckx [87]. On the basis of various cluster configurations of the minority atoms, they modelled diffuse scattering in electron diffraction patterns arising from a number of quenched alloys that exhibited special-point order. Van Tendeloo *et al.* [92] subsequently recognised that the clusters which are most appropriate for the description of the observed diffuse scattering occur in the DO_{22} structure and that the cluster variation approach mirrors the static concentration wave approach in real space. However, it has been pointed out by Stobbs and Stobbs [93] that the success of modelling particular scattering events by using a particular cluster does not necessarily imply that microdomains of this structure are appropriate in describing the order present.

The shapes of the $1^1/_20$ reflections appear to be characteristic of the particular alloy system; Ni_4Mo and Au_4Cr show relatively discrete, spherically symmetrical reflections, whilst Au_4V shows streaked reflections. De Ridder *et al.* [87] interpreted the streaking as being the result of different types of clusters formed on quenching, whilst Stobbs and Stobbs [93] have suggested that the streaking may be produced by long-range interactions between the localised static concentration wave packets associated with the as-quenched state of order. Interestingly, the intensity of the reflections produced by the alloys referred to above is the inverse of that which may be expected from structure factor considerations [92].

Dilute Au-Ti alloys, although known to possess a long-range-ordered (D1a) phase, have not been studied previously with a view to investigating the existence of $<1^1/_20>$

special-point order on quenching; the identification and characterisation of this state of order in dilute Au_4Ti alloys will constitute a major portion of the work that follows.

2.4 OVERVIEW

Considerable progress has been made toward understanding the physical processes behind ribbon formation during CBMS. However, the interactions between the physical processes during rapid solidification have not been successfully modelled and as a result the present understanding of conditions at the solidification front is largely based on conjecture from indirect evidence such as photocalometric observations and microstructural examination.

The effects of rapid solidification on alloy microstructure include enhanced terminal phase solute solubility, the refinement of segregation, the refinement of grain size and the formation of metastable phases. Of these effects the effect of rapid solidification on solute segregation has been the subject of particular theoretical interest as the traditional theory for understanding the formation of microsegregation during solidification (i.e. the principle of constitutional supercooling) has been proved to be invalid under rapid solidification conditions. This occurs because a number of assumptions made in the principle of constitutional supercooling are not valid under rapid solidification conditions. These include the assumption that the partition coefficient at the solid-liquid interface is equal to the equilibrium partition coefficient and independent of interface velocity. In addition, the effects of capillarity at the solid-liquid interface are assumed to be negligible, and the evolution of latent heat at the solidification front is assumed to have no effect on the stablity of the interface. These effects become significant at the high interface velocities associated with rapid solidification. These factors are taken into account in the modern theory of interface stability, known as the perturbation theory. This theory predicts a much wider range of solidification conditions under which the interface is stable (and hence no microsegregation occurs) than does the principle of constitutional supercooling. In particular it predicts that at interface velocities above a critical value (known as the absolute interface velocity) the solidification front will be stable with respect to the formation of solutal dendrites, irrespective of the thermal gradient at the interface.

CBMS is a relatively simple technique to achieve rapid solidification and as a result it is used widely to determine the effect of rapid solidification on the microstructure of

materials. However, although some of the effects of rapid solidification have been observed in the microstructure of CBMS materials, the identification of the effects is hindered by a dearth of information about the conditions at the solid-liquid interface as well as the fact that the microstructures observed during CBMS are strongly influenced by the evolution of latent heat at the solidification front. The latter effect results in solidification conditions (and hence microstructures) varying through the thickness of materials produced by CBMS. Thus while CBMS is a relatively easy and convenient technique to achieve rapid solidification, the solidification conditions prevalent are rather complex, and as a consequence the microstructures formed do not readily lend themselves to theoretical modelling.

The alloys considered in the work that follows are CBMS dilute Au-Ti alloys. At equilibrium Au-Ti alloys exhibit a decreasing terminal phase solubility for Ti with decreasing temperature. The phase in equilibrium with the terminal phase is Au_4Ti, a long-range-ordered phase with Strukturbericht designation D1a. A number of other alloy systems which, at equilibrium, possess a phase of this structure exhibit, on quenching from high temperatures, a metastable state of order known as $<1\frac{1}{2}0>$ special-point order. This state of order has not been observed previously in Au-Ti alloys and thus its characterisation in the as-solidified alloys and the subsequent transformation route on post solidification heat treatment is of considerable interest.

-ooOoo-

CHAPTER 3

EXPERIMENTAL PROCEDURES

This chapter describes the experimental approach adopted in the work that follows. In addition, the experimental methods utilised in the preparation of the rapidly solidified alloys and the methods used for the characterisation of the microstructures, structural order and mechanical properties directly on solidification and after post-solidification heat treatment are detailed.

3.1 EXPERIMENTAL APPROACH

The effects of rapid solidification on the microstructures of materials are all directly or indirectly dependent upon the cooling rate achieved during solidification (see Chapter 2), thus in order to systematically study the effects of rapid solidification on the microstructure and properties of alloys it is necessary to study materials which have all been produced with the same cooling rate [20]. However, when rapidly solidifying by means of CBMS the cooling rate achieved is dependent on the processing parameters, and this dependence is a function of both the alloy system and the alloy composition. Thus, in order to study the effects of CBMS on a particular alloy system, the dependence of the cooling rate on processing parameters as a function of alloy composition should be determined prior to assessing the effects of rapid solidification on the alloy microstructures.

The CBMS experiments were carried by the author on brief research visits to Israel, severely restricting number of CBMS experiments possible. As a result the influence of

the various processing parameters could not be evaluated individually in order to ascertain the processing conditions which will produce similar cooling rates during rapid solidification of each alloy composition. It was thus necessary to compromise and rapidly solidify all of the alloys using the same processing parameters and to anticipate that the cooling rate during rapid solidification may indirectly be a function of alloy composition.

The experimental program was designed to determine the effect of rapid solidification on the microstructures, structural order and mechanical properties of dilute Au-Ti alloys as a function of solute concentration, and to determine the thermal stability and property development of these as-solidified alloys on post-solidification heat treatment. Alloys of four different nominal compositions were prepared, namely 1wt.% Ti, 2wt.% Ti, 3wt.% Ti and 5wt.% Ti. From the equilibrium binary phase diagram shown in fig. 2.9(a) the 1wt.% Ti, 2wt.% Ti and 3wt.% Ti alloys at equilibrium contain varying amounts of f.c.c. solid solution and Au_4Ti; the amount of Au_4Ti present in the alloy increases with increasing Ti content. Au-5wt.% Ti corresponds to stoichiometric Au_4Ti. The alloy compositions were chosen in order to determine the degree to which the nucleation of the long-range-ordered (D1a) Au_4Ti can be suppressed by rapid solidification. The range of compositions prepared allowed the structural order present in the rapidly quenched alloys to be ascertained as a function of alloy composition.

Samples were rapidly solidified using a technique known as chill block melt spinning (CBMS), the principles of which were discussed in section 2.1.1. Differential scanning calorimetry (DSC) was used to determine the temperatures at which transformations occurred in the rapidly solidified alloys. The microstructural evolution resulting from heat treatment at these transformation temperatures was studied by means of light microscopy, scanning electron microscopy (SEM) and transmission electron microscopy (TEM). In addition, the structural order present in the as-solidified alloys and the subsequent transformation during heat treatment was determined by studying selected area diffraction patterns taken in the diffraction mode of the TEM. The changes in microstructure were correlated to the mechanical properties of the heat treated alloys.

3.2 EXPERIMENTAL METHODS

3.2.1 Alloy Processing

Prior to rapid solidification, the samples were pre-alloyed to ensure thorough mixing of the alloy constituents. Pre-alloying was carried out by melting together the components of alloy using induction heating under an Ar atmosphere. To prevent contamination, the alloy was contained within an Al_2O_3 tube during melting. Thorough mixing of the alloy constituents was ensured by repeating this melting step a number of times. A limited amount of oxidation of the surface of the sample occurred during pre-alloying; this oxide layer was removed by immersing the sample in a 30wt.% solution of $K_2S_2O_7$ in water and heating the solution to 400°C [95]. The water boiled off, leaving behind a molten salt flux. The sample was removed from the molten flux and quenched into water. Adhering residues of flux were removed by boiling the sample in water.

The melt spinning apparatus used to rapidly solidify the samples is illustrated schematically in fig. 3.1. The inner surface of the quartz tube was covered with a protective coating to prevent contamination of the molten sample. The coating was applied in the form of a layer of zirconium diboride suspension, which was baked onto the tube surface at 760°C for 30 min. The base of the tube contained a 0.75 mm diameter nozzle which was positioned 1 mm from the wheel surface at the apex of the wheel (refer to figure). The surface of the wheel was polished with 1000 grit emery paper and degreased with acetone to ensure intimate contact between the melt and the wheel surface. A 5 g pre-alloyed sample charge was inserted into the quartz tube, and pure Ar streamed into the tube until a protective atmosphere had developed. The sample was then induction melted to a temperature of approximately 1400°C; this temperature was chosen as it ensured that all of the alloys were completely molten prior to expulsion from the quartz tube (fig. 2.9(a)). The temperature of the melt was monitored by means of an optical pyrometer. The molten sample was expelled, by a burst of Ar, through the nozzle in the base of the tube and onto the circumference of a brass wheel rotating with a surface speed of 26 m/s. This speed was chosen as it is in the middle of the range generally used during CBMS (see e.g. [28]). Identical processing conditions were used for melt spinning all of the alloys prepared.

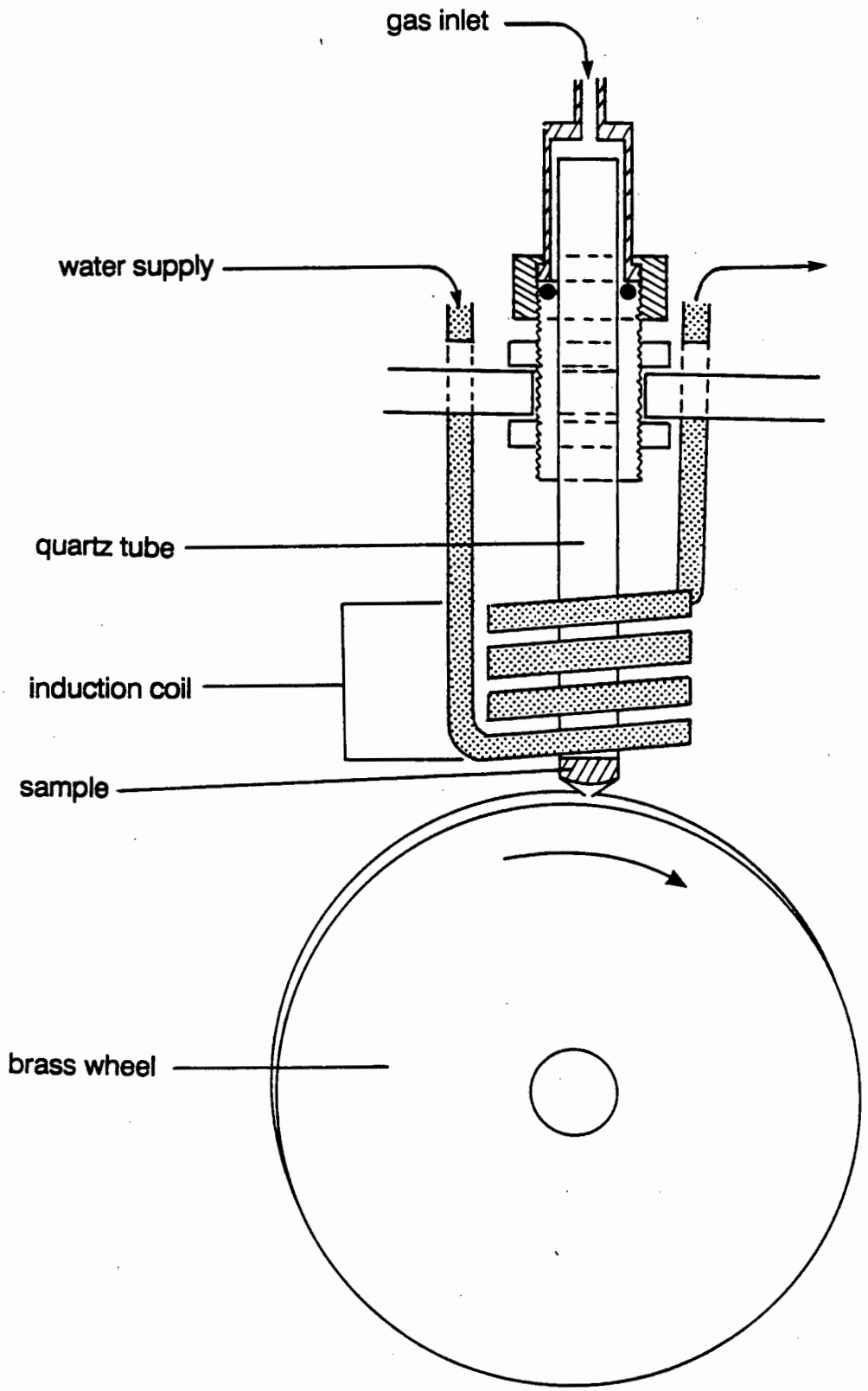

Fig. 3.1 Schematic diagram of the CBMS apparatus used to prepare rapidly solidified samples.

3.2.2 Alloy Thermal Stability and Heat Treatment

Temperatures at which transformations occurred in the rapidly solidified alloys were determined by means of differential scanning calorimetry (DSC) using a Mettler TA3000 DSC instrument. The output from the DSC instrument is a signal (as a function of time) which is proportional to the difference in heat input required to keep the sample and a reference at the same, constantly rising, temperature. Transformation temperatures in a particular alloy are derived from the DSC traces by determining the temperatures at which changes in the gradient of heating or cooling curves occur [96].

A sample mass of 11.4 mg was used for all DSC runs: the mass was chosen as a compromise between the need to produce detectable thermodynamic peaks on heating, and the need to conserve material. The holder containing the sample and an empty holder which served as a reference were placed within the DSC cell, which was continually purged with Ar to prevent oxidation. DSC traces were obtained over the temperature range 50°C to 600°C, the upper temperature being limited by oxidation of the Al sample holder. A relatively high programmed heating rate of 20°C/min was used, as previous studies in other alloy systems had shown that this rate increased the detectability of low enthalpy transformations (see e.g. [97]). However, the high heating rate used may adversely influence the accuracy of the transformation temperatures determined from the DSC traces. Specimens were heated, cooled and reheated to determine the reversibility of the detected transformations; the cooling curve was found to be of little value, as the instrument was unable sustain a controlled cooling rate of 20°C/min. DSC traces were obtained from two samples of each alloy in order to determine the reproducibility of the curves.

Heat treatments were subsequently carried out at the transformation temperatures determined by DSC. All of the post-solidification heat treatments were performed under vacuum in a horizontally supported tube furnace. The furnace was repeatedly flushed with Ar and then evacuated to a pressure of less than 1.3×10^{-3} Pa (10^{-5} Torr). A standard heating rate of 6°C/min was used for all heat treatments. After the required time at temperature, the specimens were furnace cooled under vacuum by switching off the furnace. The average uncontrolled cooling rate was measured to be above 4.5°C/min above 300°C, and gradually decreasing at temperatures below this value.

3.2.3 Mechanical Testing

All of the melt spun ribbons were less than 35 μm thick and showed large variations in ribbon dimensions; consequently the mechanical properties of the as-solidified and heat treated samples were determined by means of microhardness tests performed on polished cross-sections of the ribbons. Prior to indentation, the polished samples were lightly etched in order to remove any residual surface deformation, and then repolished (see section 3.2.4 for details of polishing procedure and etches used). The small ribbon thickness limited the maximum size of the indentations; a Knoop indenter with a load of 15 g (the minimum load available on the Shimatzu microindentation instrument used) was found to produce indentations of suitable dimensions (fig. 3.2).

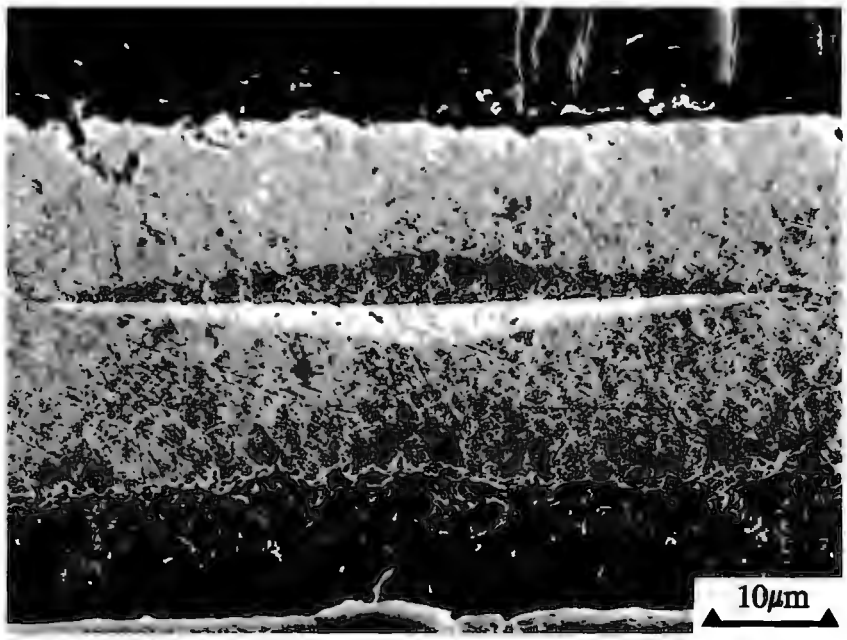

Fig. 3.2 Secondary electron SEM image of a Knoop microhardness indentation in a polished ribbon cross-section of a Au-1wt.% Ti as-solidified ribbon.

Twelve microhardness indents were performed on each specimen in order to characterise each material. On one specimen from each alloy the number of indents was increased from 12 to 50; however, the increased number of indents did not

significantly change the mean microhardness value or the associated standard deviation in any of the alloys studied. The microhardness of a standard sample was determined prior to each series of microhardness tests; the measured sample hardness did not vary significantly (less than 6%) between series of tests.

3.2.4 Metallography and Structural Characterisation

The microstructures of the as-solidified and post-solidification heat treated ribbons were characterised by studying etched sections of the samples using both light and electron microscopy. The ribbon samples were mounted in a slow setting araldite resin; this resin was used as it assisted edge retention of the sample during polishing. The mounted samples were then ground on SiC pads before being mechanically polished using diamond paste. The final surface polish for Au-1wt.% Ti was obtained by mechanically polishing with 0.05 μm Al_2O_3, while for the remainder of the alloys a final polish with 0.25 μm diamond paste produced a satisfactory finish. The polished samples were chemically etched using (a) 1 part HCl, 1 part HNO_3 and 1 part water, or (b) 0.1 g CrO_3, 10 ml HNO_3 and 100 ml of HCl [98]. The latter solution was preferred for the higher caratage alloys as the etching process was more rapid than for solution (a).

Microstructures resulting from CBMS are generally highly directional (see eg. [37, 99]) and thus, in order to obtain a three-dimensional appreciation of the microstructure, it was necessary to obtain metallographic sections from several different ribbon orientations. Longitudinal cross-sections (or transverse sections) and tapered sections of the ribbons were studied: the relative orientations of the sections are shown in fig. 3.3. The process used for preparing tapered sections is illustrated in fig. 3.4.

Light microscopy on the etched samples was carried out on a Reichert MeF2 metallograph in the bright-field mode with Nomarsky interference contrast added to improve grain boundary visibility. Electron optical metallography was conducted on a Cambridge S200 SEM with a conventional tungsten filament, typically operated at a primary accelerating voltage of 20 kV. Compositional microanalyses were obtained by means of a Tracor Northern TN5400 energy dispersive X-ray microanalyser attached to the SEM and on a Cameca Camebax/Microbeam microprobe.

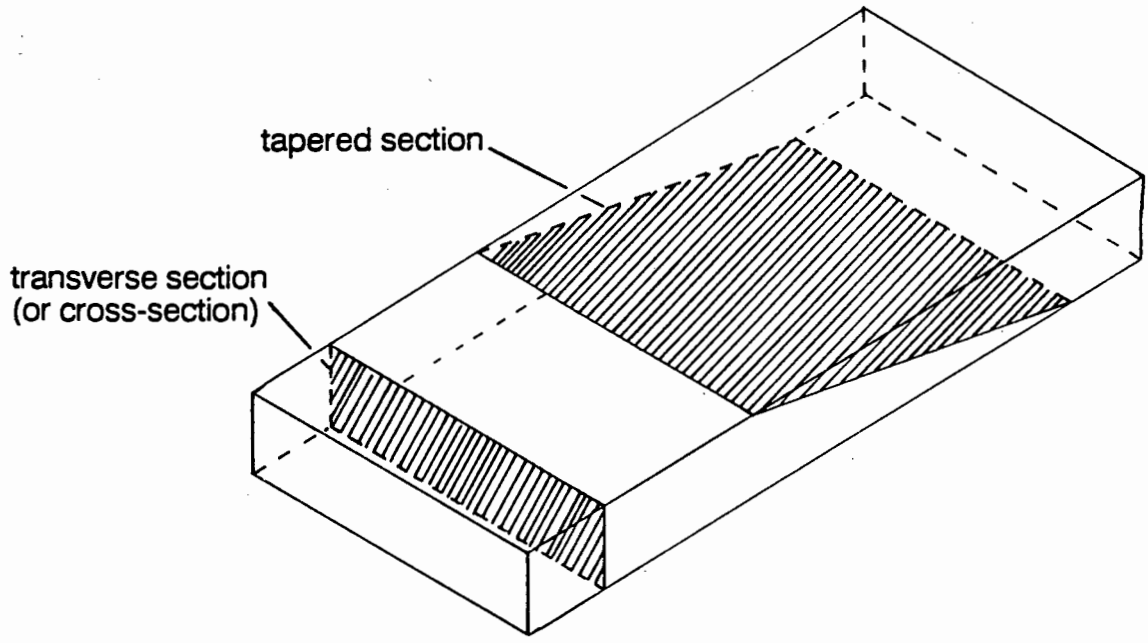

Fig. 3.3 Schematic illustration of the orientations of metallographic sections taken from the rapidly solidified ribbons.

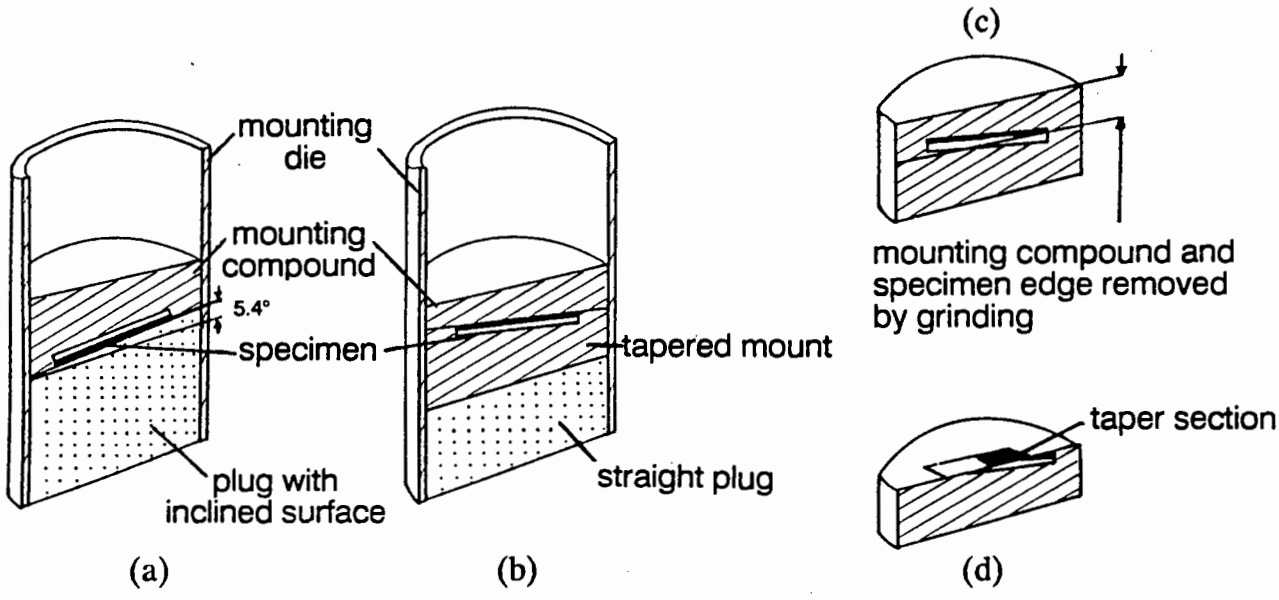

Fig. 3.4 Schematic illustration of the procedure for preparing tapered sections of the alloy ribbons.

TEM examination of the microstructures and the structural order present in the samples was carried out using a JEOL 200 CX TEM with a twin tilt facility at an accelerating voltage of 200 kV. For those alloys which formed high quality ribbons during melt spinning, TEM specimens were prepared with a Struers Tenupol twin jet polishing apparatus. The specimens were polished in a 1 molar LiCl solution in methanol with a voltage of 52.5 V and flow rate of 6 [100]. In order to obtain electron transparent regions from different areas within the thickness of the alloy ribbons, the ribbons were electropolished from the opposite side of the ribbon to the side of interest. Alloys for which the ribbon quality was too poor to allow conventional electropolishing were found to contain areas that were sufficiently oxide-free and electron transparent in both as-solidified and heat treated ribbons to enable direct observation of the microstructure without prior thinning. A bright-field TEM image from a typical "as-solidified" electron transparent area is shown in fig. 3.5.

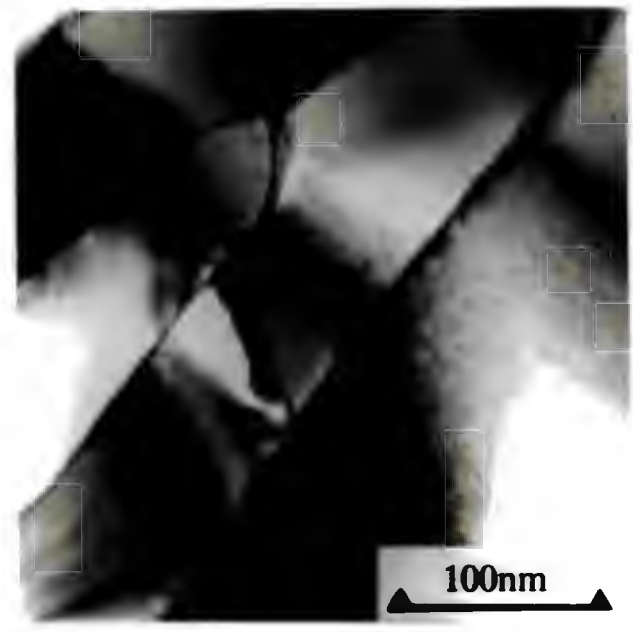

Fig. 3.5 * Bright-field transmission electron micrograph from a typical as-solidified electron transparent region in a Au-3wt.% Ti ribbon.

* All bright-field TEM images shown were taken under multiple beam diffraction conditions, unless otherwise indicated.

The state of order in the alloys was characterised by studying the diffuse scattering present in selected area diffraction patterns taken at a number of different zone-axis orientations. One of the advantages of studying these "as-solidified" electron transparent regions was that they were extremely thin, resulting in relatively few Kikuchi lines, which would tend to mask the detail of diffuse elastic scattering in the diffraction patterns. The fine grain sizes resulting from the rapid solidification process required the use of the smallest available selected area aperture when taking diffraction patterns. The resultant reduced diffracted intensities, coupled with the necessity for a well-defocussed second condenser lens in order to resolve the diffuse scattering, necessitated long exposure times; the optimum exposure times varied between 15 and 30 min. In spite of these long exposure times, sample drift was not generally found to be a limiting problem, although beam drift occasionally caused asymmetry in the intensities of the reflections.

-ooOoo-

CHAPTER 4

RESULTS

The experimental results presented in this chapter are grouped according to experimental procedure. In section 4.1 the macroscopic differences between the melt spun ribbons from various alloys are discussed, and the compositional analyses of the ribbons are detailed. Results from a differential scanning calorimetry (DSC) study into the thermal stability of the rapidly solidified ribbons are presented in section 4.2, while in section 4.3 the response of the mechanical properties of the various ribbons to heat treatment is detailed. This is followed in section 4.4 by the outcome of an investigation into the response of the alloy microstructures to post-solidification heat treatment. In section 4.5 the results from the characterisation of the structural order present in the alloys directly on solidification, and the subsequent evolution of the order on post-solidification heat treatment, are discussed. Section 4.6 is a summary of the effect of heat treatment on the microstructure, structural order and properties of each of the rapidly solidified alloys.

4.1 MACROSCOPIC CHARACTERISATION

Alloys of nominal compositions Au-1wt.% Ti, Au-2wt.% Ti, Au-3wt.% Ti and Au-5wt.% Ti were prepared by means of chill block melt spinning (CBMS) under processing conditions detailed in section 3.2.1. Increasing alloy solute content resulted in a tendency for the nozzle at the base of the quartz tube to become blocked during melt spinning. Subsequent examination of the rapidly solidified products revealed that increasing solute content was associated with a deterioration in the geometrical and visual uniformity of the rapidly solidified products. CBMS of Au-1wt.% Ti formed high

quality ribbons (fig. 4.1(a)), Au-2wt.% Ti solidified into poorer quality ribbons (fig. 4.1(b)), Au-3wt.% Ti formed short, narrow ribbons (fig. 4.1(c)) and CBMS of Au-5wt.% Ti produced small flakes of material (fig. 4.1(d)).

(a)

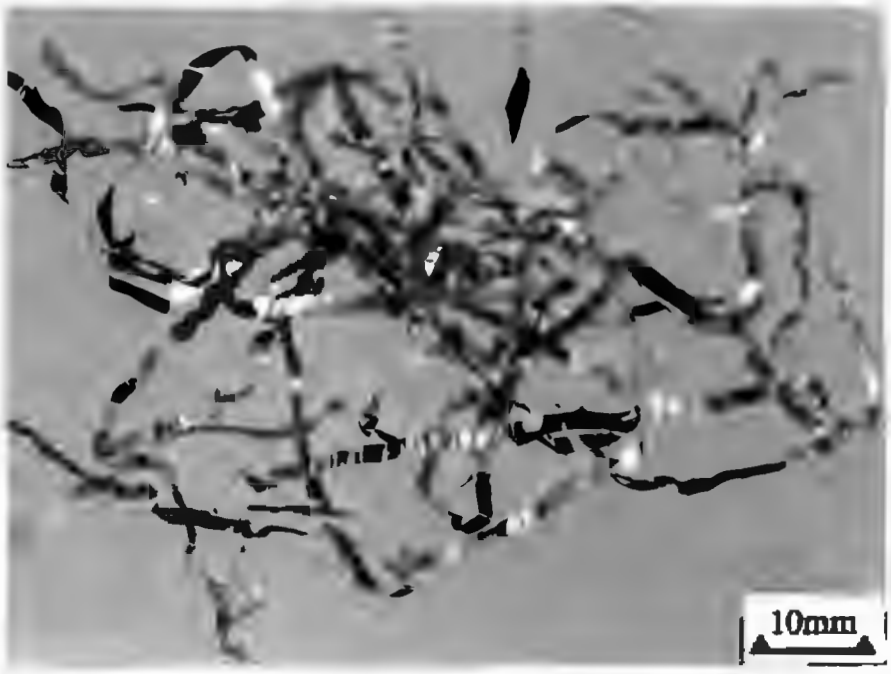

(b)

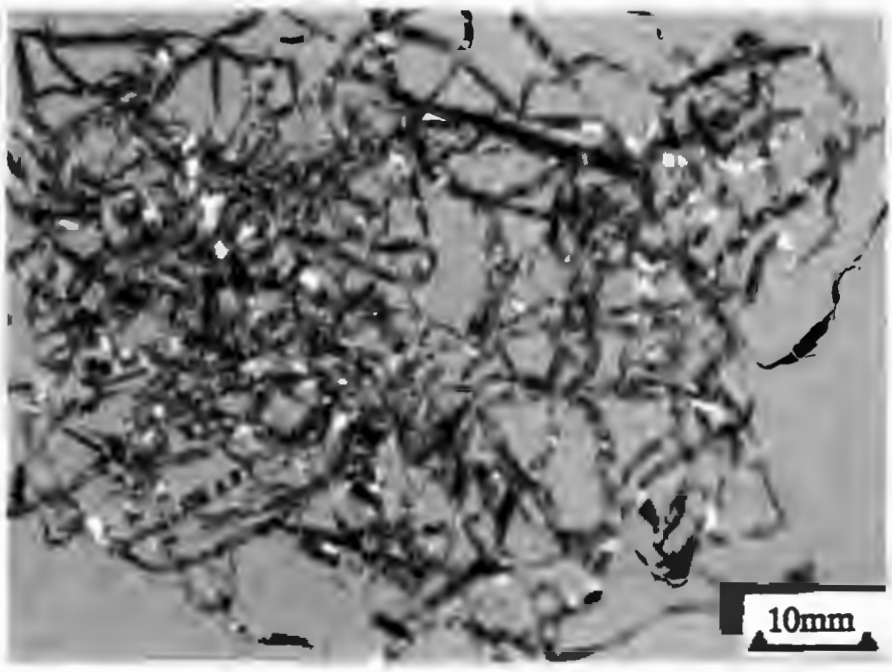

Fig. 4.1 Light micrographs of the rapidly solidified products produced by CBMS: (a) Au-1wt.% Ti; (b) Au-2wt.% Ti.

(c)

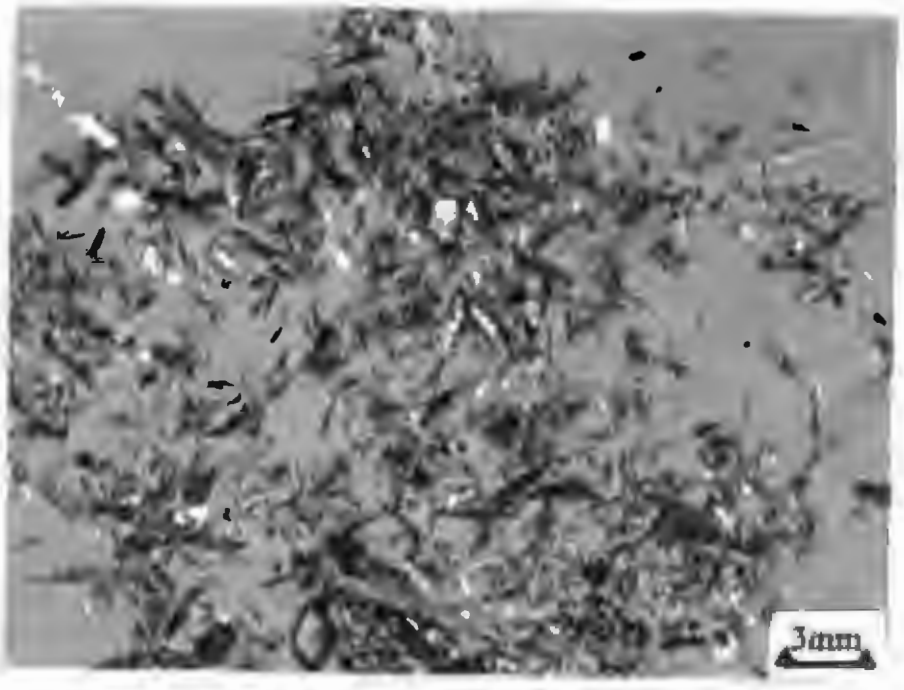

(d)

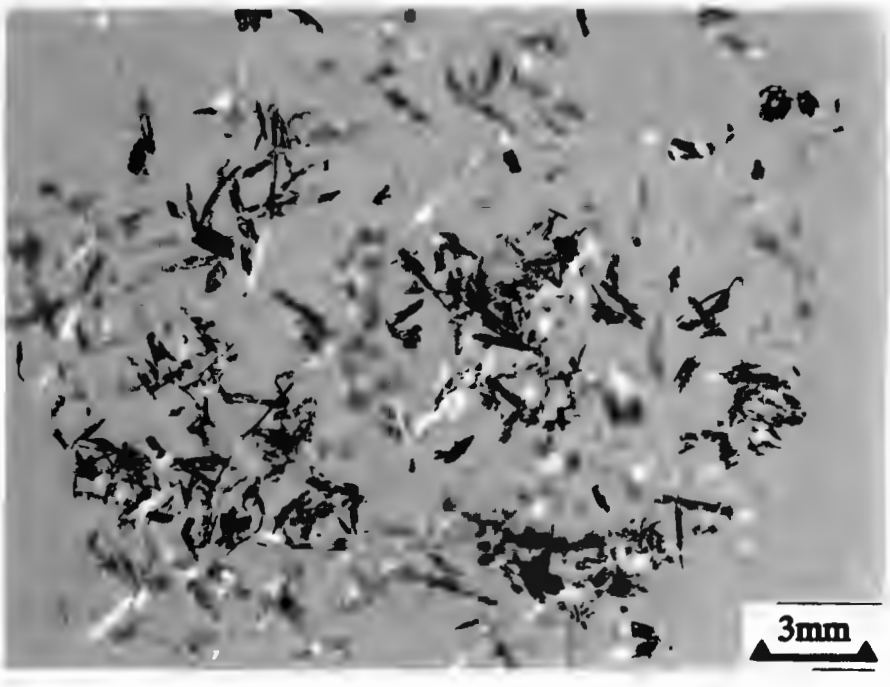

Fig. 4.1 (cont.) Light micrographs of the rapidly solidified products produced by CBMS: (c) Au-3wt.% Ti; (d) Au-5wt.% Ti.

The average widths (w) of the 1wt.% Ti, 2wt.% Ti and 3wt.% Ti alloy ribbons were determined by averaging 20 measurements obtained using a calibrated graticule in an optical microscope. Au-5wt.% Ti was not examined as this alloy did not form ribbons during rapid solidification. From these measured widths (given in table 4.1) it is apparent that the deterioration in ribbon quality with increasing Ti content was accompanied by a decreasing average ribbon width and an increasing associated standard deviation.

The macroscopic roughness of the interfaces of the rapidly solidified ribbons prevented the average ribbon thicknesses from being measured directly. However, by determining the average width (w), length (l) and mass (W_r) of several sections of ribbon and assuming theoretical density* (ρ_r) for the particular alloy, the average ribbon thicknesses (X_{ave}) was calculated from:

$$X_{ave} = W_r/\rho_r wl \qquad (4.1)$$

The X_{ave} values for the Au-1wt.% Ti and Au-2wt.% Ti ribbons are given in table 4.1; each value quoted is the average of the X_{ave} calculated from four ribbons. It was not possible to determine the average thickness of the Au-3wt.% Ti ribbons by means of this technique due to the small dimensions of the ribbons and the considerable variation of these dimensions within a length of ribbon. The average ribbon thickness of the 3wt.% Ti ribbons was estimated by taking the mean of 20 thickness measurements from polished ribbon cross-sections (X_{meas} in table 4.1). However, the X_{meas} values for Au-1wt.% Ti and Au-2wt.% Ti ribbons are larger than the calculated X_{ave} values for these alloys, suggesting that X_{meas} is an overestimate for X_{ave} for the 3wt.% Ti alloy.

From the average ribbon widths and thicknesses given in table 4.1, the average volume of material being delivered from the nozzle onto the wheel per second (or volumetric flow rate, Q) may be calculated from:

$$Q = wX_{ave}V_s \qquad (4.2)$$

where V_s is the surface velocity of the wheel (which, from section 3.2.1, was 26 m/s). The calculated values of Q (given in table 4.1) decrease with increasing Ti content,

* The densities were calculated from weighted ratios of the densities of pure Au and pure Ti.

suggesting that the observed deterioration of ribbon quality with increasing solute content is the result of a decrease in the flow rate of the melt from the nozzle as a function of alloy Ti content.

Table 4.1 Dimensions of the as-solidified CBMS ribbons.

Alloy	Au-1wt.% Ti	Au-2wt.% Ti	Au-3wt.% Ti
Average Width (w) (mm)	1.18 ± 0.046	0.88 ± 0.082	0.35 ± 0.132
Calculated Average Thickness (X_{ave}) (μm)	24.5 ± 1.86	10.5 ± 1.56	(9.51 ± 4.39)*
Measured Cross-Sectional Thickness (X_{meas}) (μm)	32.1 ± 2.02	13.5 ± 2.65	9.51 ± 3.39
Volumetric Flow Rate (Q) (cm^3/s)	0.758 ± 0.0643	0.240 ± 0.0421	0.086 ± 0.0513

* refer to page 56.

Optical examination of the wheel-side surfaces of the melt spun ribbons (fig. 4.2(a) and fig. 4.3(a)) shows that all of the alloy ribbons replicated the morphology of the wheel surface, i.e. the morphology resulting from polishing the wheel surface with emery paper prior to CBMS. The surface of the Au-3wt.% Ti ribbon which was exposed to the air during rapid solidification (the free surface) exhibits a streaked morphology reminiscent of the wheel-side interface of this alloy (fig. 4.3(b)). However, the free surfaces of the Au-1wt.% Ti (fig. 4.2(b)) and 2wt.% Ti ribbons are similar in appearance and relatively smooth.

A secondary electron SEM image of the wheel-side surface of a 1wt.% Ti ribbon (fig. 4.4(a)) shows that, although the surface contains a number of air-pockets and inclusions, some of the morphology of the wheel surface has been reproduced. The morphology of the wheel-side ribbon interface suggests that there was good wetting of the wheel surface by the melt, and therefore good thermal contact was achieved at the interface. The wheel-side surfaces of both the 2wt.% Ti and 3wt.% Ti alloy ribbons are

(a)

(b)

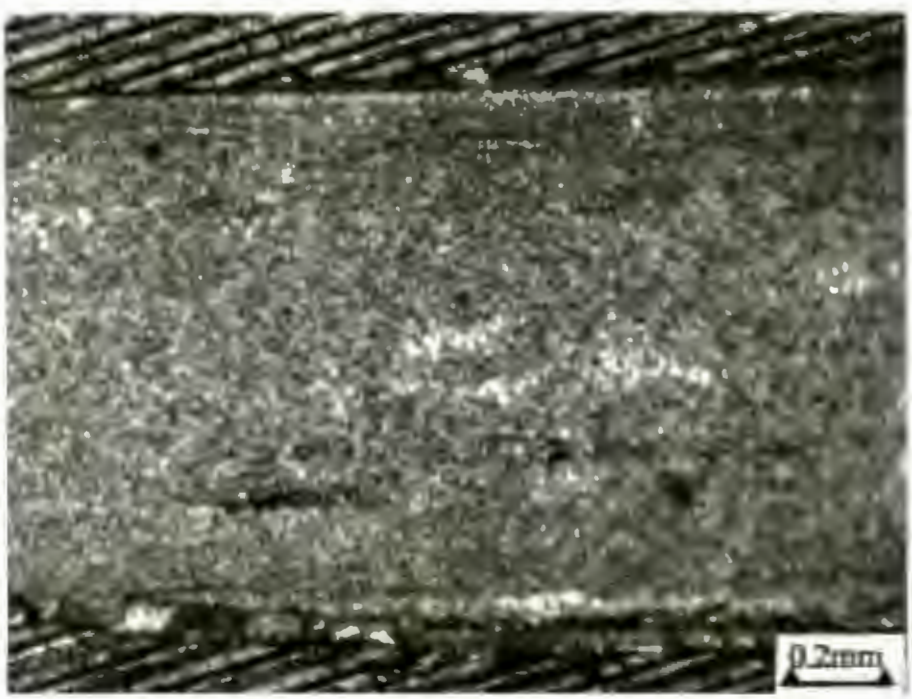

Fig. 4.2 Light micrographs of the wheel-side and free surfaces of the as-solidified ribbons: (a) wheel-side surface of Au-1wt.% Ti; (b) free surface of Au-1wt.% Ti.

(a)

(b)

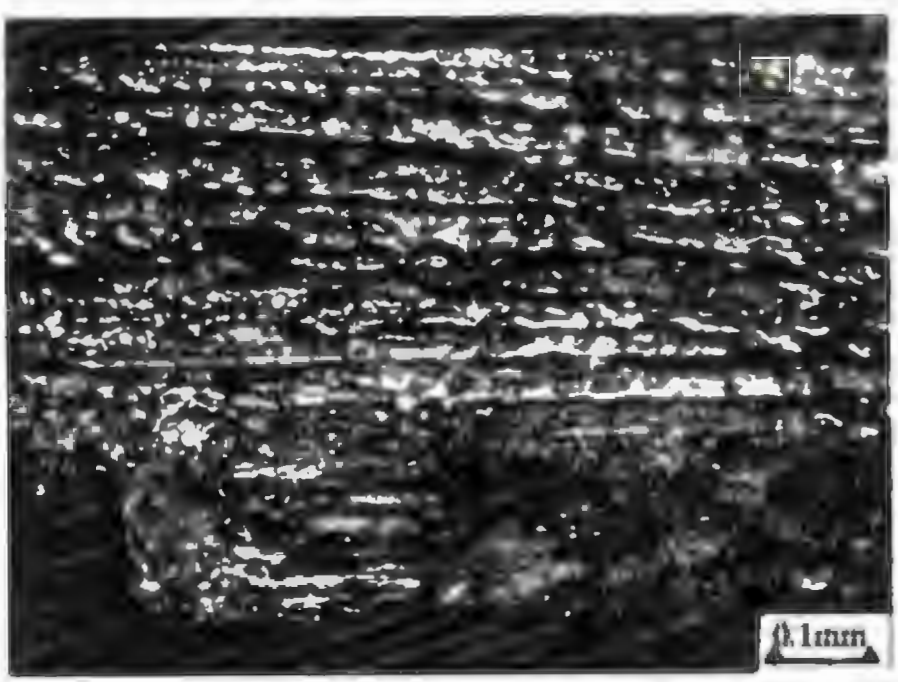

Fig. 4.3 Light micrographs of the wheel-side and free surfaces of the as-solidified ribbons: (a) wheel-side surface of Au-3wt.% Ti; (b) free surface of Au-3wt.% Ti.

similar in appearance to that of Au-1wt.% Ti. The free surface of a 1wt.% Ti ribbon consists of small, relatively evenly sized grains and shows no indication of the direction of the wheel motion during solidification (fig. 4.4(b)). The morphology of the free surface of a 2wt.% Ti alloy ribbon is similar to that of the 1wt.% Ti alloy ribbon. The morphology of these surfaces suggests that the free surfaces of the ribbons were fully solidified on emerging from the melt pool, implying that there was no significant momentum transfer to the melt during CBMS of these alloys (see section 2.1.1). SEM examination of the free surface of a 3wt.% Ti ribbon shows that, although the surface is somewhat streaked, the microstructure observed is not consistent with that expected from solidification of a rapidly moving liquid (fig. 4.4(c)). The streaked morphology of the free surface is probably the result of the morphology of the wheel-side interface of the ribbon being propagated through the ribbon interface by the solidification front. The replication of the wheel-side morphology on the free surface is not seen in the 1wt.% Ti and 2wt.% Ti alloy ribbons, as the thickness of these ribbons would tend to suppress the effect.

(a)

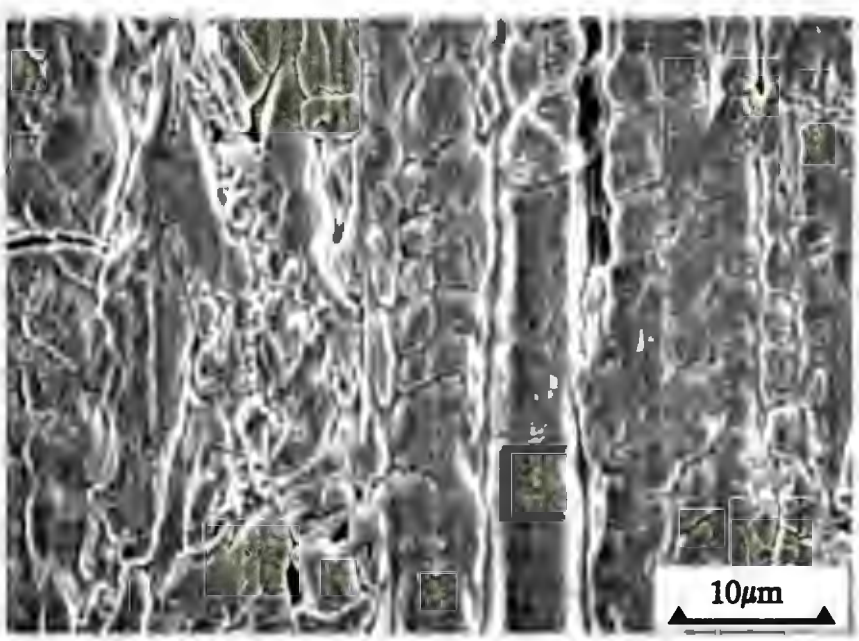

Fig. 4.4 Secondary electron SEM image of the (a) wheel-side surface of Au-1wt.% Ti ribbon.

(b)

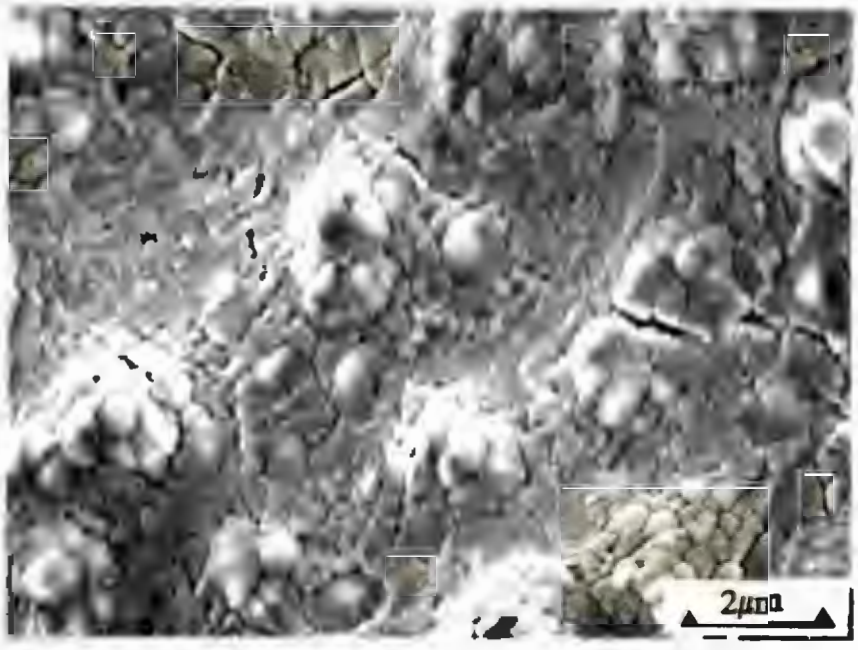

(c)

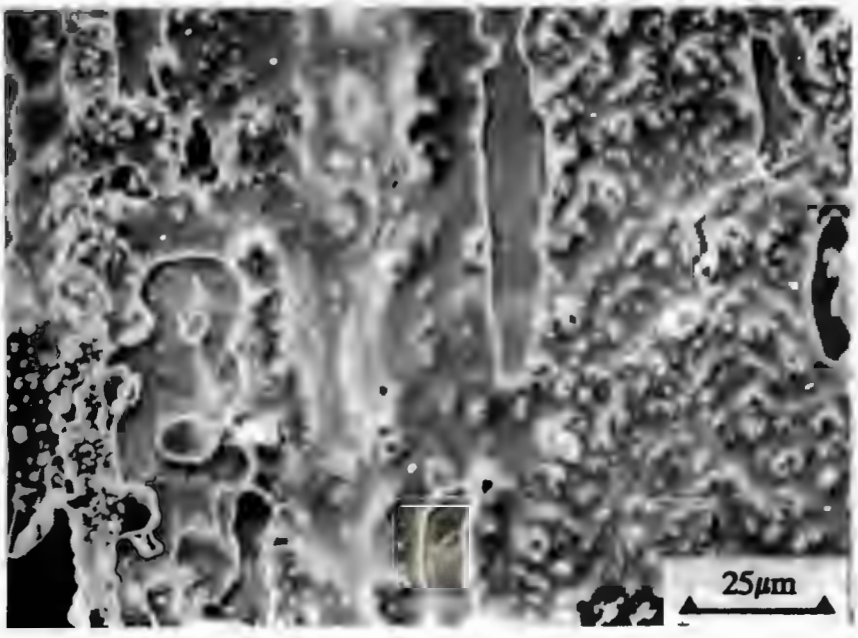

Fig. 4.4 (cont.) Secondary electron SEM image of (b) the free surface Au-1wt.% Ti and (c) the free-surface of the Au-3wt.% Ti melt spun ribbon.

The ribbon compositions were determined by means of both wavelength dispersive spectroscopy (WDS) using an electron microprobe and energy dispersive spectroscopy (EDS) analyses on polished ribbon cross-sections. The WDS analyses were based on standards, while the EDS analyses were semi-quantitative. The results of the analyses are given in table 4.2; the quoted values are the average of five analyses. In the WDS analyses the only elements detected were Au and Ti. When analysing the 5wt.% alloy using WDS, the diameter of the electron probe was of the same order of magnitude as the ribbon thickness and considerable charging occurred during the analyses of these ribbons; as a result no WDS analyses of the 5wt.% Ti were possible.

Table 4.2 Microanalyses of the as-solidified Au-Ti alloy ribbons.

Nominal Alloy Composition (wt.%)	Microprobe Analysis (wt.%)	EDS Analysis (wt.%)
Au: 99	99.61 ± 0.01	97.82 ± 0.04
Ti: 1	0.65 ± 0.01	0.56 ± 0.03
Si:	Not Detected	1.57 ± 0.06
Au: 98	98.100 ± 0.04	96.58 ± 0.06
Ti: 2	1.91 ± 0.03	1.76 ± 0.03
Si:	Not Detected	1.63 ± 0.12
Au: 97	97.20 ± 0.11	96.15 ± 0.10
Ti: 3	2.56 ± 0.12	2.42 ± 0.05
Si	Not Detected	1.48 ± 0.06
Au: 95	--	94.07 ± 0.08
Ti: 5	--	4.64 ± 0.06
Si:	--	1.33 ± 0.10

The EDS system utilised is attached to a SEM; the small probe size and low current densities associated with SEM allowed EDS spectra to be obtained readily from all the alloys. The EDS spectra contained Au, Ti and Si peaks; however, on the basis of the

WDS analyses and from previous experience, the Si peak was ascribed to excitation of the Li-drifted Si detector. WDS analyses are expected to be more accurate than semi-quantitative EDS analyses, as the peak to background ratios in WDS are generally superior and background fitting in WDS is far simpler than for EDS. In addition, the EDS analyses are semi-quantitative, while for WDS the compositions are calculated from calibrations with standards. Nevertheless, the analyses are similar for both the WDS and EDS analyses (table 4.2). For all of the alloys, the measured Ti content is lower than the nominal alloy composition; the loss of Ti during processing was probably the result of the formation of oxide on the bulk sample surface during pre-alloying (refer to section 3.2.1). Although the measured compositions are consistently lower than the nominal compositions, in the work that follows the various alloys will for convenience be referred to by their nominal compositions.

4.2 DIFFERENTIAL SCANNING CALORIMETRY

Differential scanning calorimetry (DSC) was carried out on the rapidly solidified Au-1wt.% Ti, Au-2wt.% Ti and Au-3wt.% Ti ribbons in the manner detailed in section 3.2.2; DSC was not performed on Au-5wt.% Ti due to a shortage of rapidly solidified product of this material. Two DSC runs were performed on each sample: the first run was done while heating the sample from 50°C to 600°C, the sample was then allowed to cool to 50°C and a second run was done on reheating to 600°C. The differences between the two traces indicate the temperatures at which irreversible thermodynamic events occurred. The traces for Au-1wt.% Ti, Au-2wt.% Ti and Au-3wt.% Ti are shown in fig. 4.5(a), (b) and (c) respectively.

The two traces for Au-1wt.% Ti (fig. 4.5(a)) are virtually indistinguishable, implying that no irreversible thermodynamic events were detected on heating this alloy. However, in the DSC traces for Au-2wt.% Ti and Au-3wt.% Ti a number of irreversible thermodynamic events were detected (fig. 4.5(b) and (c) respectively). Both of these alloys exhibit an exothermic peak which is first detectable at approximately 320°C, but which is centred at approximately 370°C. A second peak is seen at approximately 480°C (centred at approximately 500°C) in the 3wt.% Ti alloy and some evidence of a similar peak is seen for the 2wt.% Ti alloy at a slightly higher temperature.

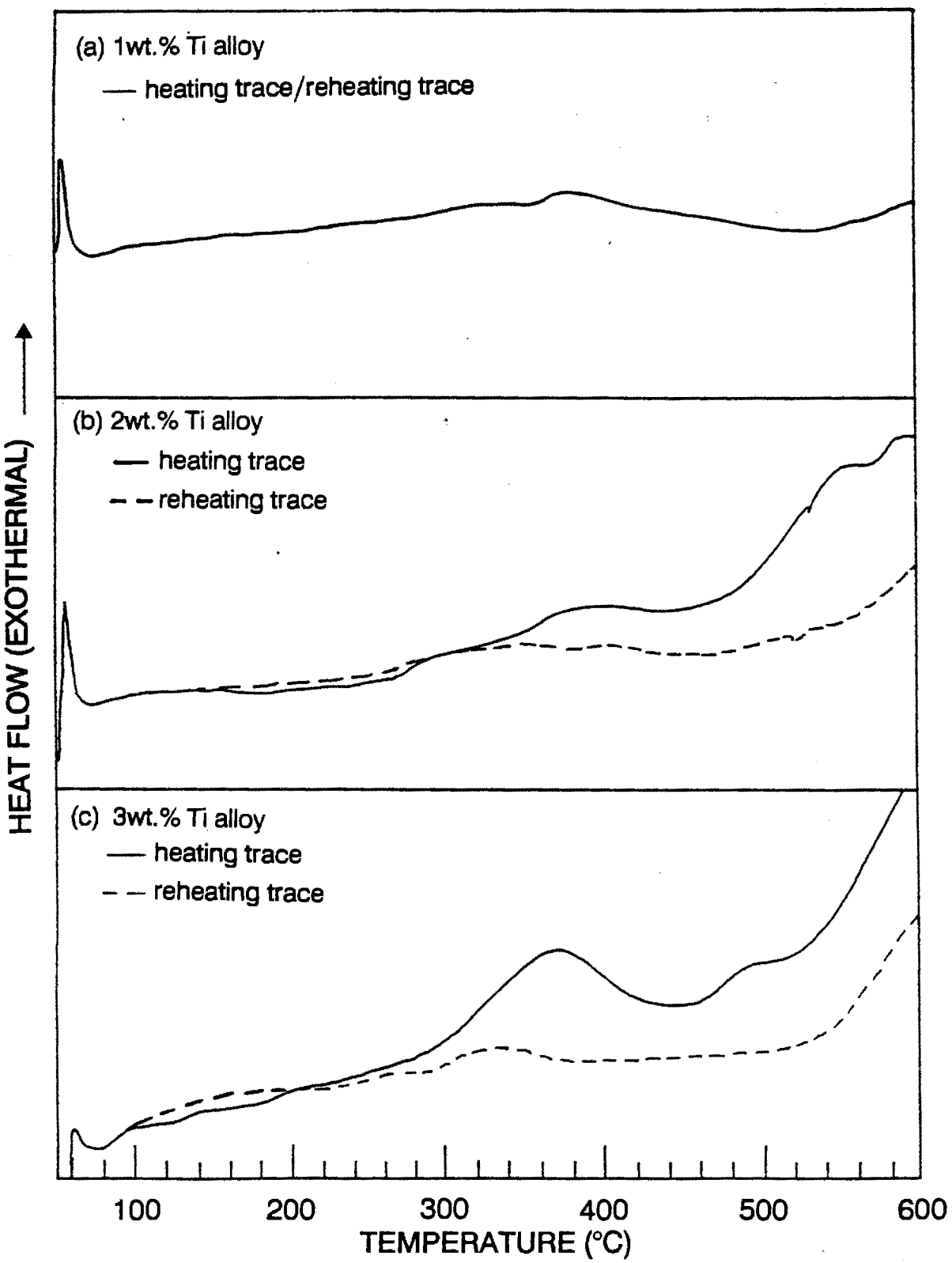

Fig. 4.5 Differential scanning calorimetry traces obtained on heating (solid line) and on reheating (dashed line) the rapidly solidified samples: (a) Au-1wt.% Ti; (b) Au-2wt.% Ti; (c) Au-3wt.% Ti.

A transformation is assumed to commence at the temperature at which the first suggestion of a thermal event is detected in a DSC trace (see e.g. [97]). It is thus this temperature, rather than the temperature at which the peak is centred, that is of importance when determining the thermal stability of a sample. On the basis of fig. 4.5, as well as previously published results on the heat treatment of Au-1wt.% Ti [1, 3], heat treatment temperatures of 350°C and 500°C were chosen for the initial investigation of the thermal stability of the rapidly solidified alloys. Heat treatments were carried out at these temperatures for 1 h and for 24 h, and the microstructures and microhardness of the alloys prior and subsequent to post-solidification heat treatment compared. Additional heat treatments were subsequently performed in order to clarify trends in the microhardness tests or features of the microstructures resulting from these initial heat treatments.

4.3 MICROHARDNESS

The Knoop microhardness of as-solidified and post-solidification heat treated samples was determined from polished ribbon cross-sections. The microhardness of Au-1wt.% Ti, Au-2wt.% Ti and Au-3wt.% Ti is plotted as a function of heat treatment in fig. 4.6(a), (b) and (c) respectively; the Au-5wt.% Ti ribbons were too thin to accommodate microhardness indentations. The microhardness of the 1wt.% Ti alloy decreased on heat treatment (fig. 4.6(a)); indeed, after 24 h at 500°C the alloy microhardness decreased to a value similar to that of annealed Au (i.e. 40.25 ± 4.58 kg/mm^2).

The microhardness of Au-2wt.% Ti and Au-3wt.% Ti increased on heat treatment, the hardness value being a function of both heat-treatment time and temperature (fig. 4.6(b) and (c)). The microhardness of the 2wt.% Ti alloy increased with increasing heat-treatment times at 350°C. However, the microhardness of the 3wt.% Ti alloy increased after 1 h at 350°C, but longer times at this temperature produced no significant increase in the alloy hardness. In order to clarify the trends seen for these alloys, additional heat treatments were done at 350°C for 12 h. The hardness of the 2wt.% Ti alloy after this heat treatment was 167.31 ± 12.54 kg/mm^2, suggesting that the hardness of this alloy at 350°C increased steadily with time. After 12 h at 350° the hardness of the 3wt.% Ti alloy was 170 ± 5.67 kg/mm^2, i.e. approximately the same as that produced after 1 h and 24 h at this temperature. Thus the microhardness achieved

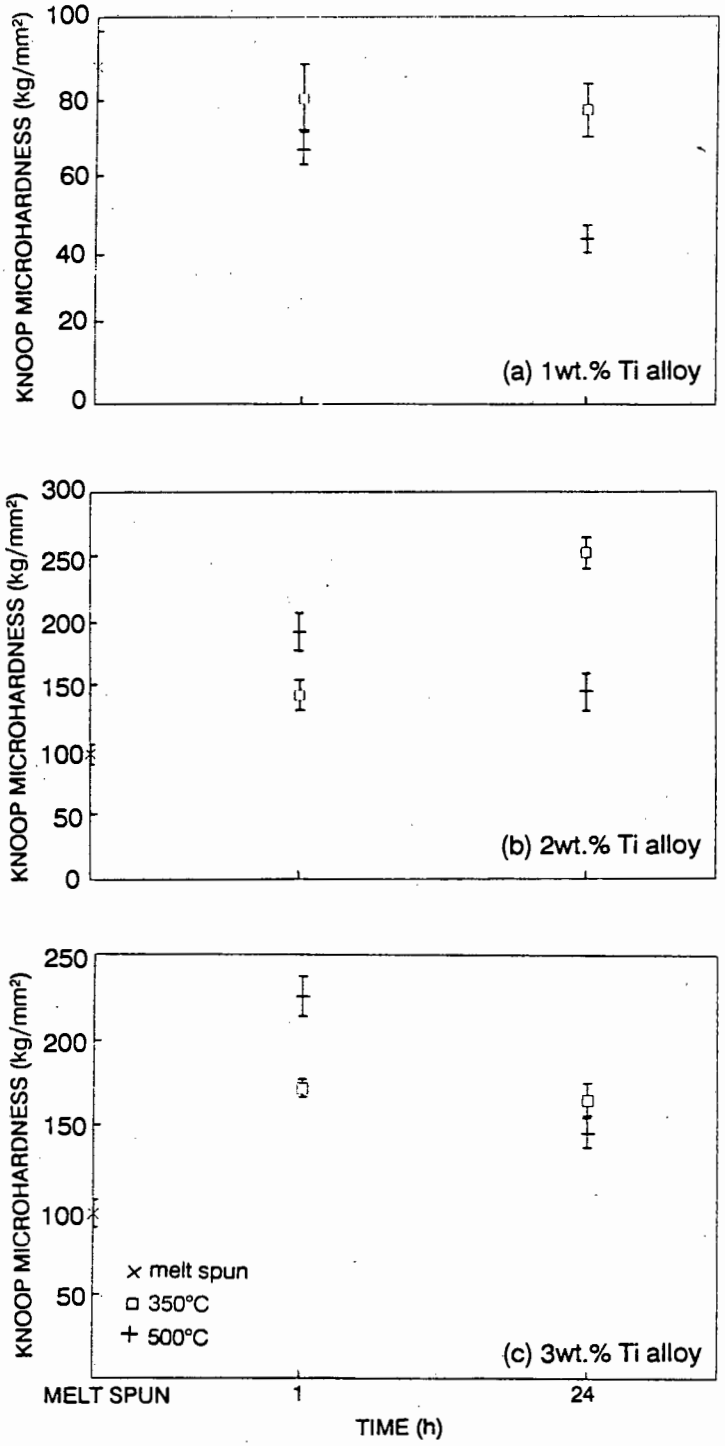

Fig. 4.6 The measured Knoop microhardness (15 g normal load) of the ribbon cross-sections as a function of time and heat treatment: (a) Au-1wt.% Ti; (b) Au-2wt.% Ti; (c) Au-3wt.% Ti.

in this alloy after 1 h at 350°C was unaltered by longer heat treatments at this temperature.

Heat treatment at 500°C considerably hastened the kinetics of the hardening of these alloys; the hardness of both the 2wt.% Ti and 3wt.% Ti alloys increased rapidly after 1 h at this temperature; however, longer heat-treatment times at this temperature resulted in a deterioration of the microhardness of both of the alloys. In order to rationalise the changes in microhardness in the various alloys on heat treatment, the evolution of microstructure as a function of heat treatment was determined.

4.4 MICROSTRUCTURAL CHARACTERISATION

The microstructures of the as-solidified alloys and their evolution on post-solidification heat treatment were studied using optical microscopy, SEM and TEM. The results are grouped according to alloy composition.

4.4.1 Au-1wt.% Ti

A variation in the etching response is observed across a ribbon section from as-solidified Au-1wt.% Ti in fig. 4.7(a). This variation is manifested as two distinct regions: a region adjacent to the wheel-side surface of the ribbon (arrowed in the figure) which shows little response to etching, and a second region which is darkened by etching. SEM examination of an etched ribbon cross-section reveals that the as-solidified microstructure consists of a variable grain size and morphology which is dependent upon the distance from the wheel-side surface of the ribbon (fig. 4.7(b)). The region immediately adjacent to the arrowed surface comprises columnar grains extending at right angles to the wheel-side surface. At a distance of approximately 10 μm from the wheel-side surface there is a transition from columnar grains to a fine equiaxed grain morphology. These equiaxed grains coarsen progressively with increasing distance from the arrowed surface until the free surface of the ribbon is reached.

An etched tapered section taken along the length of an as-solidified Au-1wt.% Ti ribbon (fig 4.8(a)) exhibits a gradual coarsening of the microstructure through the

(a)

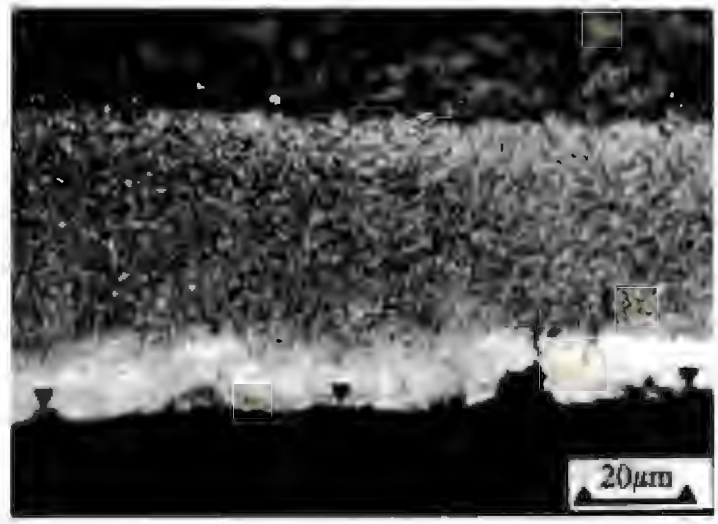

(b)

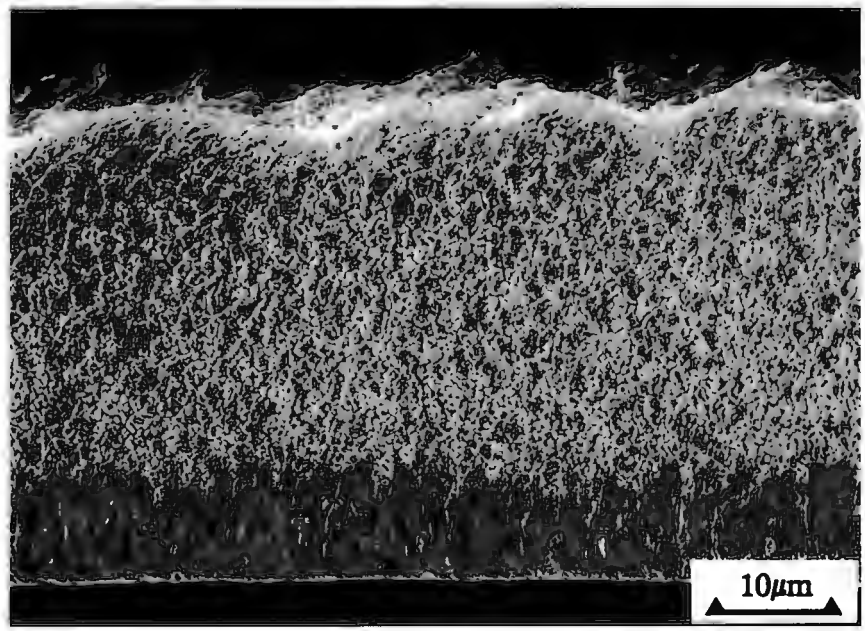

Fig. 4.7 Etched cross-sections from as-solidified Au-1wt.% Ti ribbons: (a) light micrograph; (b) secondary electron SEM image (the wheel-side surfaces of the ribbons are arrowed).

ribbon cross-section with no evidence of the transition in microstructure seen in fig. 4.7. The region immediately adjacent to the wheel-side surface of the ribbon, when examined at a higher magnification, consists of grains which exhibit a slightly different etching response to the rest of the section (fig 4.8(b)). Examination of a number of tapered sections confirmed that these grains are limited to a narrow region adjacent to the wheel-side surface and are thus clearly distinct from the transition in microstructure seen in fig. 4.7.

The variation in etching response across the ribbon cross-section is reminiscent of that seen by Jones [101] in splat quenched Al-Fe alloys and by Chu and Granger [73] in melt-spun Al-Fe alloys. In Al-Fe alloys this transition in microstructure is the result of a variation in the segregation of solute as a function of distance from the wheel-side surface. In order to study the distribution of solute in the 1% Ti alloy in different regions of the ribbons, TEM foils were prepared by electrothinning from the opposite side of the ribbon to the side of interest. A bright-field TEM micrograph of the as-solidified microstructure from within the columnar grain region (fig. 4.9(a)) shows that the microstructure in this region is fine grained with no evidence of strain contrast in the lattice arising from the presence of precipitates. In addition, selected area electron diffraction patterns contained no additional reflections attributable to the presence of precipitates. An electron transparent region from the equiaxed region of the ribbon shows the grain size in this region to be larger (fig. 4.9(b)) than in the columnar region; however, no evidence of second phase formation or solute segregation is seen. The absence of second phase was confirmed using selected area diffraction. The transition in microstructure in the as-solidified 1wt.% Ti alloy is thus not the result of a variation in segregation of Ti across the ribbon section.

As shown previously (fig. 4.6(a)), heat treatment of Au-1wt.% Ti resulted in a decrease in the ribbon microhardness. In fig. 4.10 the microhardness of Au-1wt.% Ti in the as-solidified condition and after post-solidification heat treatment at 350°C and 500°C (each for 1 h and 24 h) are replotted together with the microhardness values after heat treatment for 1 h and 24 h at 400°C. Etched cross- sections of the heat treated ribbons are shown in fig. 4.11. As seen from fig. 4.11, the grain size and morphology are dependent upon heat treatment temperature and time. A limited degree of grain growth occurred in the equiaxed regions of the microstructure after annealing at 350°C

(a)

(b)

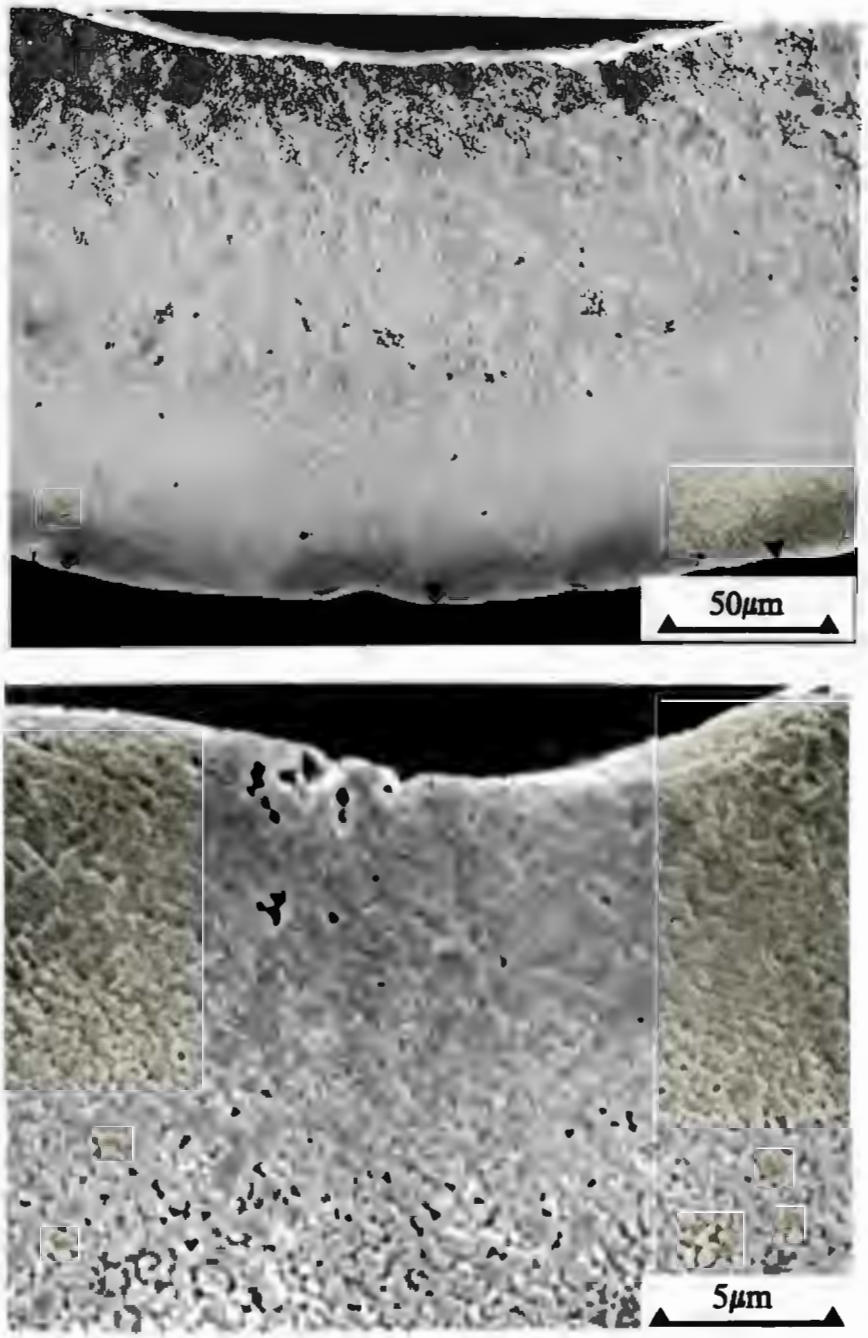

Fig. 4.8 Secondary electron SEM image of etched tapered section from as-solidified Au-1wt.% Ti alloy (the orientation of the section is illustrated in fig. 3.3): (a) microstructure of entire ribbon thickness (the wheel-side surface of the ribbon is arrowed); (b) microstructure immediately adjacent to the wheel-side surface.

(a)

(b)

Fig. 4.9 Bright-field TEM images from as-solidified Au-1wt.% Ti ribbons: (a) characteristic microstructure of region adjacent to the wheel-side surface; (b) region adjacent to the free surface.

and 400°C. However, exposure at 500°C resulted in marked grain growth. This response of the equiaxed grain size to heat treatment was quantified by establishing the average grain size from etched ribbon cross-sections using the mean linear intercept method. The average grain diameter (D_{ave}) was calculated from (see e.g. [102]):

$$D_{ave} \simeq 1.75\, d_{mean} \qquad (4.3)$$

where d_{mean} is the mean linear intercept i.e.

$$d_{mean} = 1/n$$

where n is the number of grain boundaries (or grains) per unit length of traverse. A minimum of four etched ribbon cross-sections per heat treatment were studied and in each condition a total of at least 500 boundaries were counted. The average grain sizes of the as-solidified and heat treated ribbons determined by the mean linear intercept method are given in table 4.3. The standard deviation associated with grain sizes (determined by the mean linear intercept method) has been shown to be given by [102]:

$$\sigma_d = \sigma_{int} / (n)^{1/2} \qquad (4.4)$$

where σ_{int} is the standard deviation of the individual intercept lengths. The values of σ_d for the various heat treatment conditions of the alloy are given in table 4.3. However, from the table, the measured average grain size after heat treatment at 350°C for 24 h is smaller and outside the standard deviation of the grain size after 1 h at this temperature. This suggests that in practice the standard deviation in the grain size is larger than that given by equation 4.4. The discrepancy probably arises as the determination of grain size by the mean linear intercept method implicitly requires that the grain size be constant within the area being studied. This condition was clearly not satisfied in the as-solidified sample (fig. 4.7) and those samples which had been heat treated at 350°C (fig. 4.11(a) and (b)). The standard deviations associated with the average grain sizes in these alloys are thus somewhat larger than those values given in table 4.3.

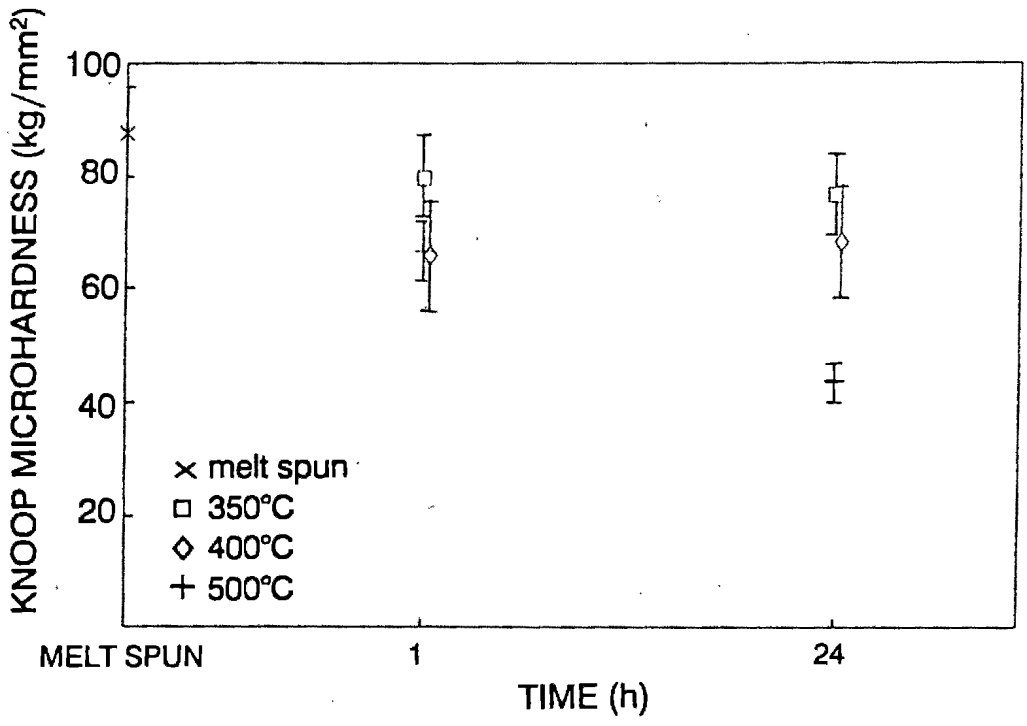

Fig. 4.10 The measured Knoop microhardness (15 g normal load) of the Au-1wt.% Ti ribbon cross-sections as a function of heat treatment time and temperature.

Table 4.3 The measured equiaxed grain size in rapidly solidified Au-1wt.% Ti as a function of heat treatment time and temperature.

Heat treatment	Average grain size (D_{ave}) (μm)	σ_d (μm)
as-solidified	1.50	0.023
350°C/1h	1.69	0.019
350°C/24h	1.56	0.028
400°C/1h	2.53	0.057
400°C/24h	2.54	0.039
500°C/1h	3.78	0.100
500°C/24h	5.79	0.190

The response of the equiaxed grain size to heat treatment temperature and time is plotted in fig. 4.12(a). The figure shows that little grain growth occurs on heat treatment at 350°C, even after 24 h. A limited amount of grain growth occurs after 1 h at 400°C, but for longer times at this temperature the grain size is stable. Grain growth thus commences in the Au-1wt.% Ti alloy at a temperature between 350°C and 400°C. Heat treatment at 500°C for 1 h results in a large increase in grain size, and grain growth continues for longer heat treatment times. The variation in the Knoop microhardness as a function of the limited changes in grain size is shown in fig. 4.12(b). Predictably, an inverse relationship between grain size and microhardness is indicated, although an insufficient number of statistically significant points were available to warrant a Hall-Petch plot.

Fig. 4.11 shows that, on heat treatment, the gradation in the equiaxed grain size across the ribbon section is progressively eliminated. The elimination of the gradation of the grain size by annealing is clearly demonstrated by comparing a tapered section taken from a ribbon heat treated at 400°C for 1 h (fig. 4.13) to that obtained from an as-solidified ribbon (fig. 4.8). In addition, the disappearance of the columnar grain structure adjacent to the wheel-side of the ribbon surface is a sensitive function of temperature and time. Coarsening of the columnar grains occurs after 1 h at 350°C (fig. 4.11(a)). However, heat treatment at 400°C for the same time (fig. 4.11(c)) results in the columnar structure starting to break down. After 1 h at 500°C the columnar structure is no longer distinguishable and the equiaxed grains present are of the same size and shape distribution as those throughout the ribbon. Heat treating for 24 h, at all of the temperatures used, results in the disappearance of the columnar grains; while some vestiges of their previous existence may be inferred from fig. 4.11(d), all evidence is absent after 24 h at 500°C.

The presence of two distinct regions in the as-solidified ribbon and the evolution of these structures on heat treatment has previously been associated with a difference in microhardness between the wheel-side and free surfaces (see e.g. Jones [101]). The microhardness of the ribbon surfaces was determined from sections of ribbon which had been glued onto a flat piece of aluminium and then mechanically polished. The microhardness of the wheel-side and the free-side ribbon surfaces is plotted as a function of heat treatment temperature and time in fig. 4.14(a) and (b). The figure shows that the microhardness values for the two surfaces are similar for the

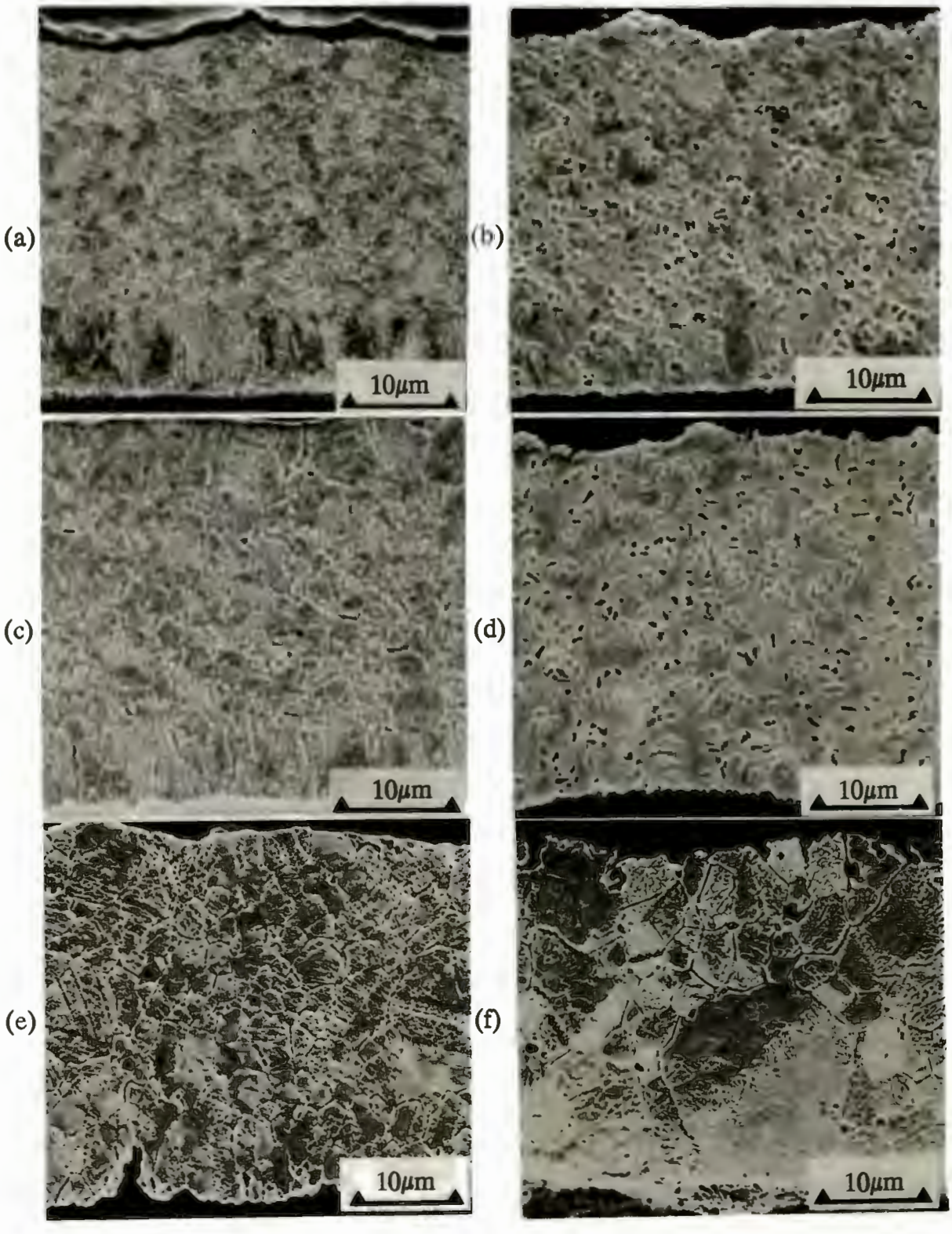

Fig. 4.11 Secondary electron SEM images of Au-1wt.% Ti ribbon cross-sections after heat treatment: (a) 350°C, (c) 400°C and (e) 500°C (all for 1 h); (b) 350°C, (d) 400°C and (f) 500°C (all for 24 h). The wheel-side surface corresponds to the bottom of the micrographs.

(a)

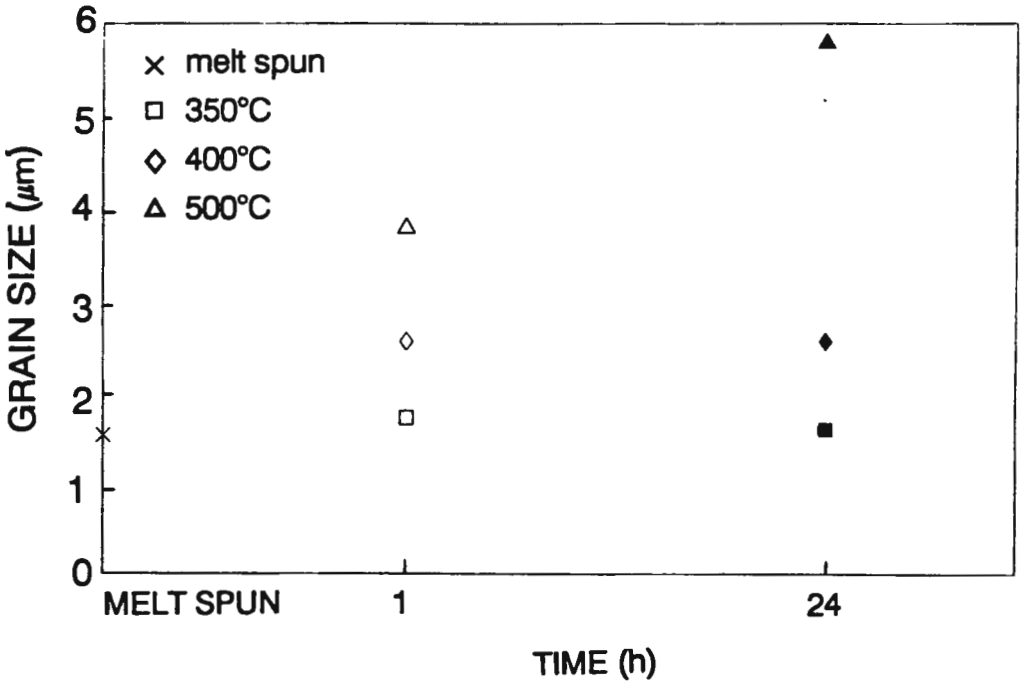

(b)

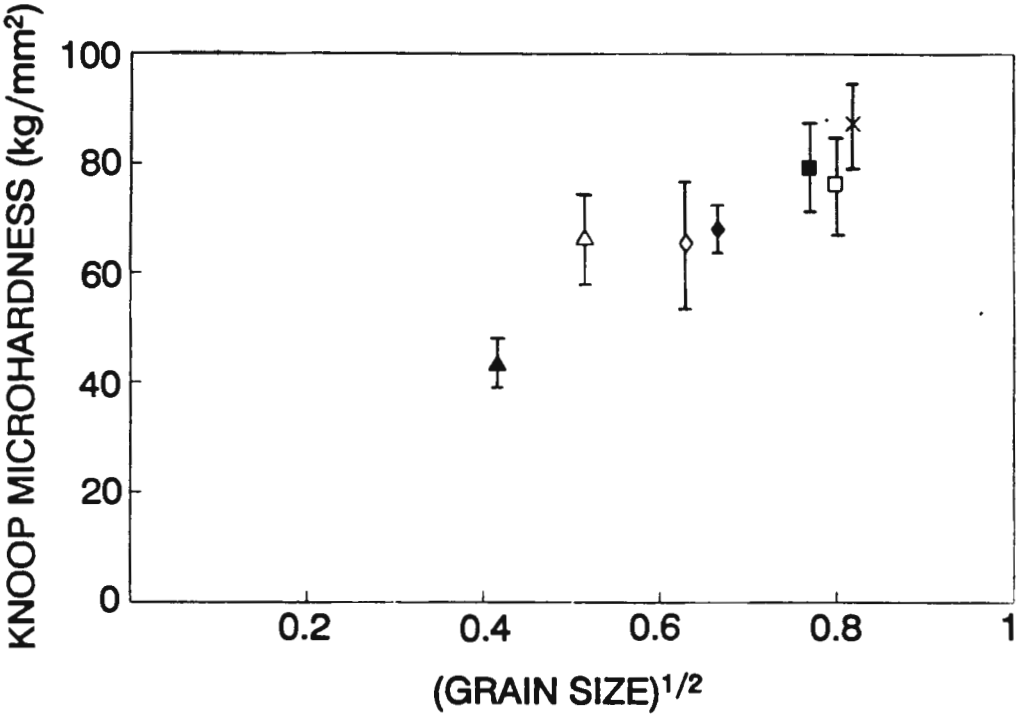

Fig. 4.12 (a) The measured equiaxed grain size of Au-1wt.% Ti as a function of heat treatment time and temperature; (b) the variation in Knoop microhardness (15 g normal load) as a function of grain size after heat treatment (open symbols 1 h, solid symbols 24 h).

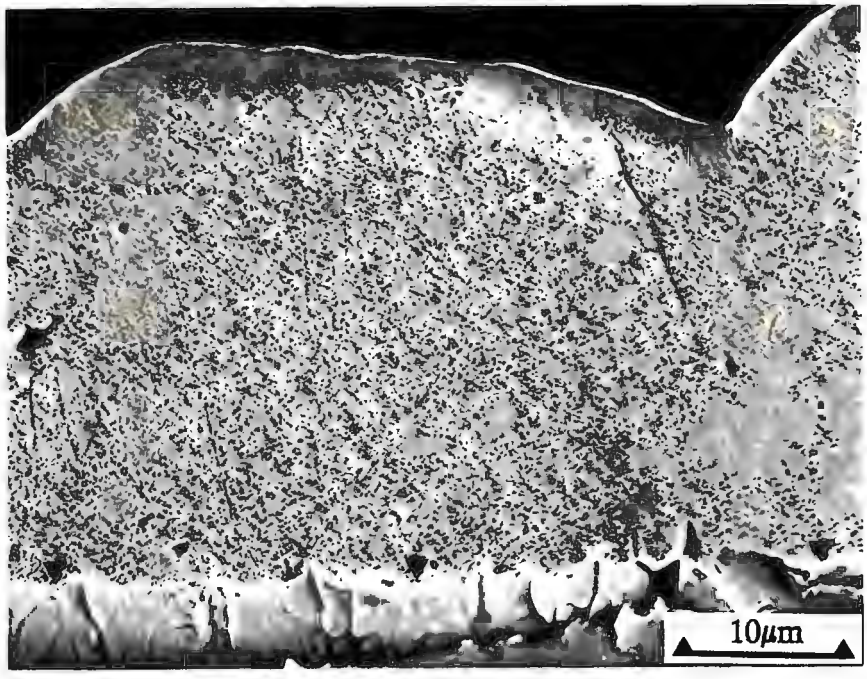

Fig. 4.13 Secondary electron SEM image of an etched tapered section of a Au-1wt.% Ti ribbon after heat treatment for 1 h at 400°C. The wheel-side surface of the ribbon is arrowed.

various heat treatment conditions. The measured microhardness values of the ribbon surfaces are consistently higher than those measured from the ribbon cross-sections (refer to fig. 4.10); however, a similar trend is observed with heat treatment temperature and time. Thus the variations in microstructure across the ribbon section of the as-solidified and heat treated alloys did not significantly influence the interfacial microhardness of the alloy.

A bright field TEM image from an electrothinned ribbon after heat treatment 24 h at 500°C (fig. 4.15), exhibits evidence of grain growth. However, no evidence of strain in the lattice due to the presence of second phase precipitates is seen in the bright field image, and no evidence was seen in the diffraction patterns of precipitation of the

(a)

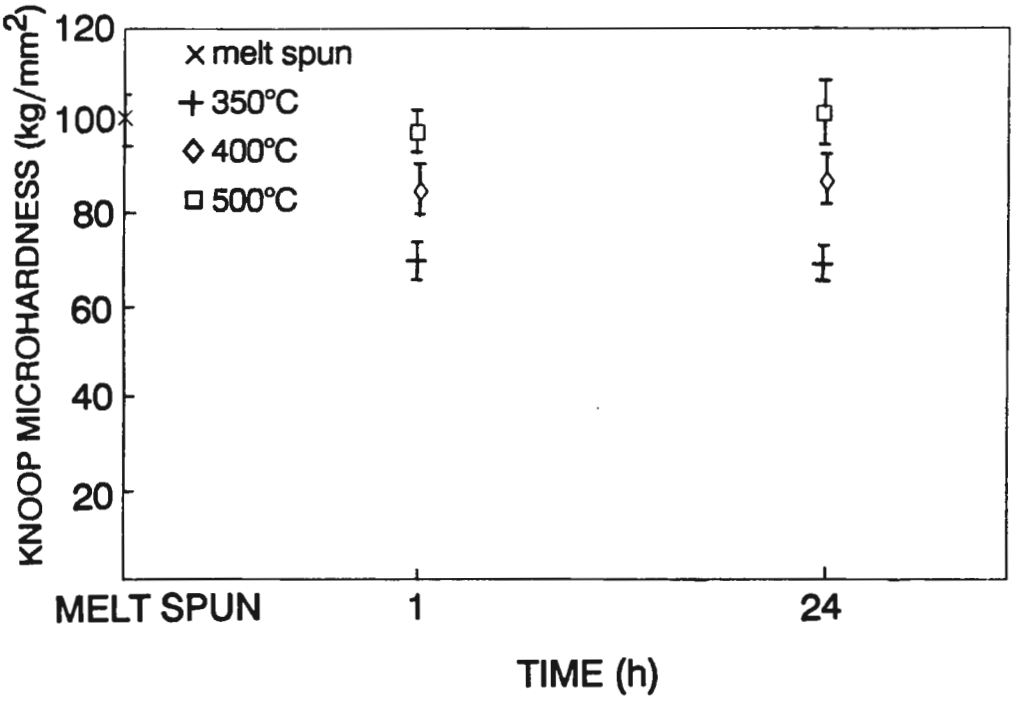

(b)

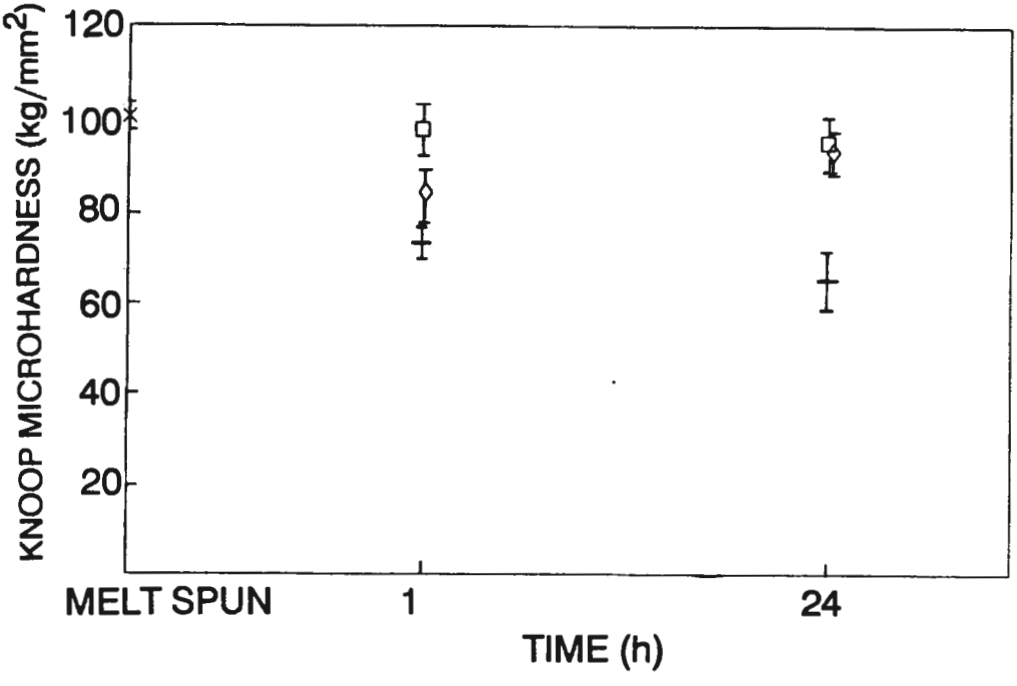

Fig. 4.14 The measured Knoop microhardness (15 g normal load) of the (a) wheel-side surface and (b) free surface of the 1wt.% Ti alloy ribbon as a function heat treatment time and temperature.

Fig. 4.15 Bright field TEM image from a 1wt.% Ti alloy ribbon after heat treatment at 500°C for 24 h.

equilibrium Au_4Ti phase. Thus the decrease in Knoop microhardness of the 1wt.% Ti alloy with heat treatment was a direct result of the observed grain growth in this alloy (as shown in fig. 4.11), with no detectable second phase formation to counteract this effect.

4.4.2 Au-2wt.% Ti

The through-thickness microstructure of this alloy directly on solidification, from the light micrograph in fig. 4.16(a), consists of columnar grains extending from the wheel-side to the free surface of the ribbon (fig. 4.16(a)). SEM examination of an etched ribbon cross-section (fig. 4.16(b)) shows that there are no additional equiaxed regions in the vicinity of the free surface of the ribbon and that the entire ribbon section is occupied by columnar grains. As the entire ribbon section consists of columnar grains

(a)

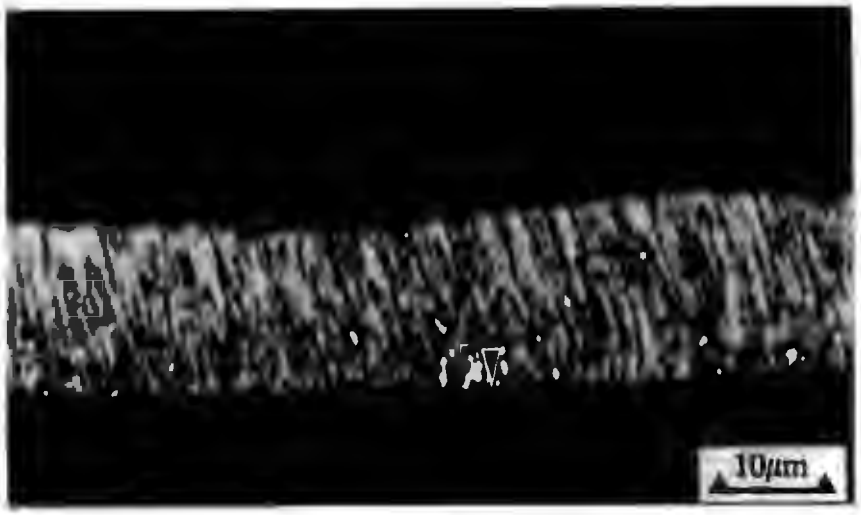

(b)

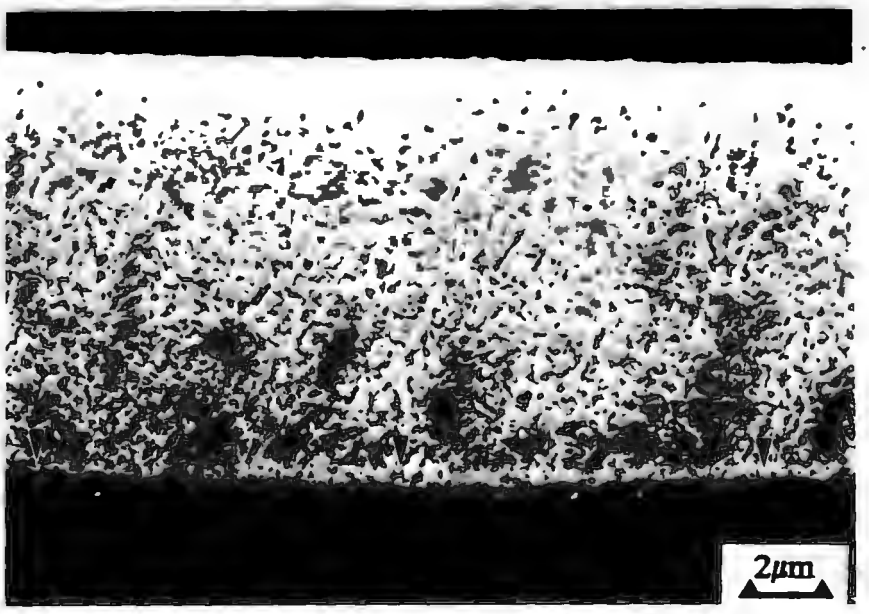

Fig. 4.16 Etched cross-sections of as-solidified Au-2wt.% Ti ribbons: (a) light micrograph; (b) secondary electron SEM image (the wheel-side surfaces of the ribbons are arrowed).

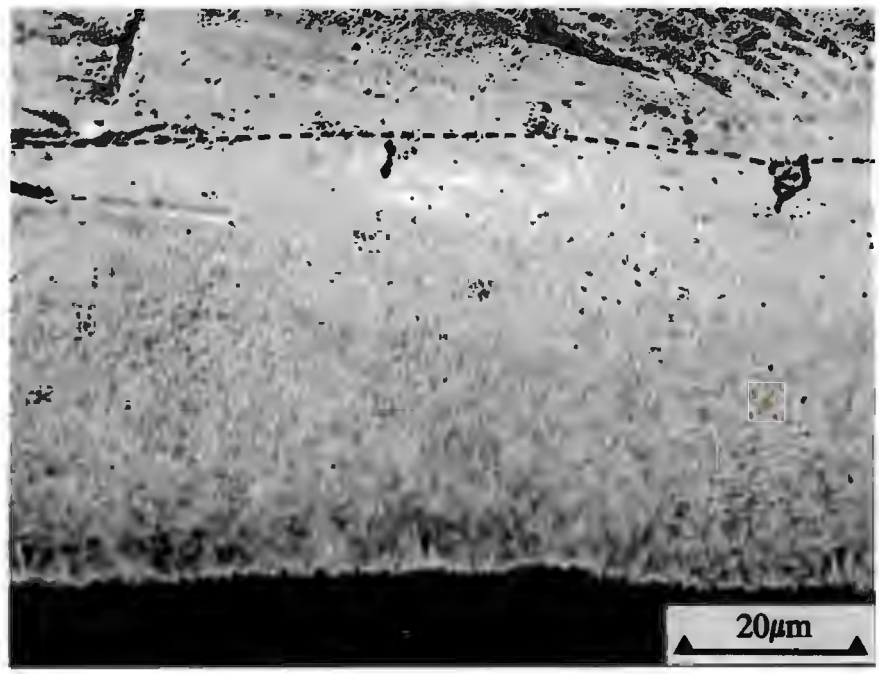

Fig. 4.17 Secondary electron SEM image of an etched tapered section from as-solidified Au-2wt.% Ti ribbon (the orientation of the section is illustrated in fig. 3.3). The wheel-side surface of the ribbon is arrowed and the boundary between the polished section and the free surface is indicated by a dashed line.

extending perpendicular to the wheel-side surface of the ribbon, a tapered section taken along the length of the ribbon shows the variation of the diameter of the columnar grains as a function of distance from the wheel surface. An etched tapered section shows that the columnar grain diameter increases as a function of distance from the wheel surface (fig. 4.17). In addition, as in the 1wt.% Ti alloy, the region adjacent to the wheel-side surface exhibits a slightly different etching response to the remainder of ribbon.

After heat treatment at 500°C for 1 h the columnar microstructure is retained, with no evidence of grain growth (fig. 4.18(a)). Heat treatment at 500°C for 24 h, however, changes the etching response of the ribbon microstructure with only traces of the columnar structure visible (fig. 4.18(b)). Nevertheless, there is sufficient evidence of

the columnar grain structure to suggest that little grain growth has occurred (fig. 4.18(b)). A tapered section of a ribbon after heat treatment at 500°C for 24 h shows that the diameters of the columnar grains are unaltered by this heat treatment (fig. 4.19).

(a)

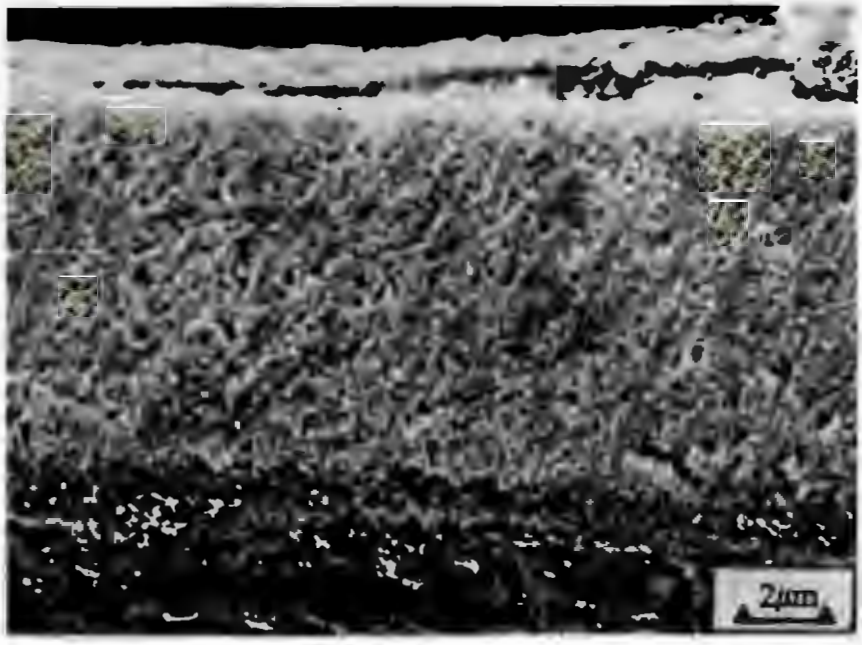

(b)

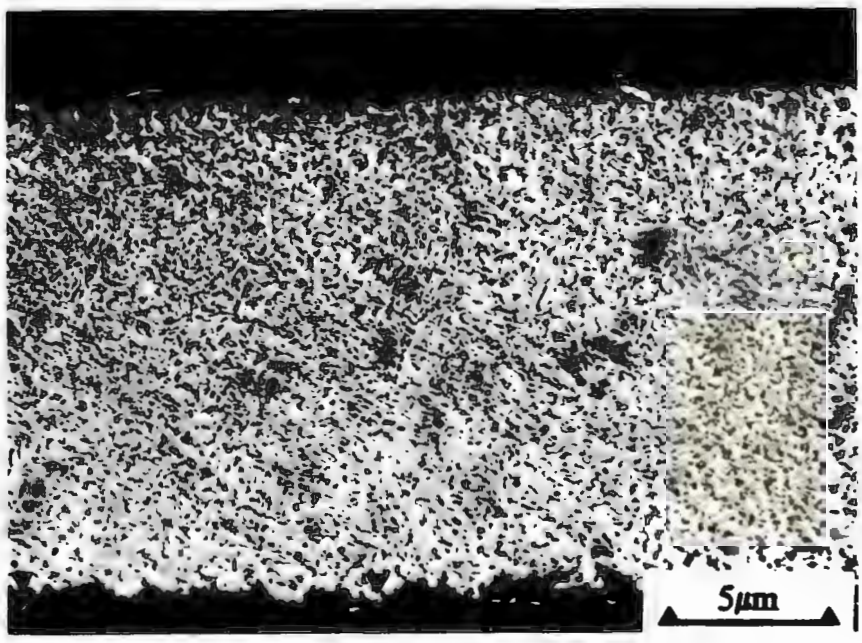

Fig. 4.18 Secondary electron SEM images of etched cross-sections from Au-2wt.% Ti ribbons after heat treatment at (a) 350°C for 24 h and (b) 500°C for 24 h (the wheel-side surfaces of the ribbons are arrowed).

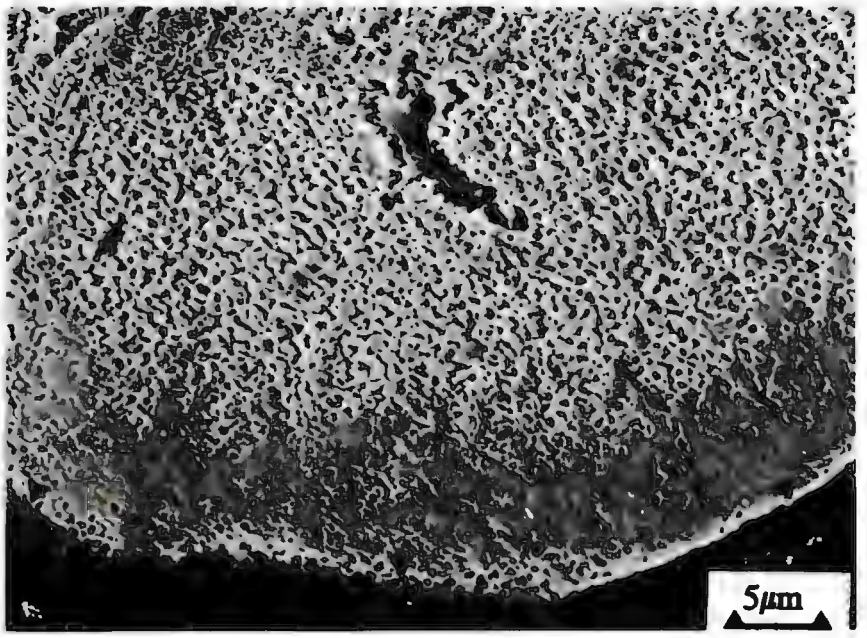

Fig. 4.19 Secondary electron SEM image of an etched tapered section from Au-2wt.% Ti ribbon after heat treatment at 500°C for 24 h (the wheel-side surface of the ribbon is arrowed).

As discussed in section 3.2.4, the as-solidified Au-2wt.% Ti ribbons contained a large number of holes through their thickness, which prohibited conventional electrothinning of the ribbons. However, sufficiently thin oxide-free regions were present in both the as-solidified and heat treated ribbons to permit direct observation of the microstructures in the TEM without prior thinning. A bright-field TEM micrograph of a typical electron transparent region in an as-solidified Au-2wt.% Ti ribbon (fig. 4.20(a)) shows that the electron transparent areas were generally somewhat distorted. There was, however, sufficient electron transparent area for the grossly distorted areas to be avoided when obtaining electron diffraction patterns. These "as-solidified" electron transparent regions were extremely thin, resulting in few discernible Kikuchi lines in the diffraction patterns (fig. 4.20(b)).

(a)

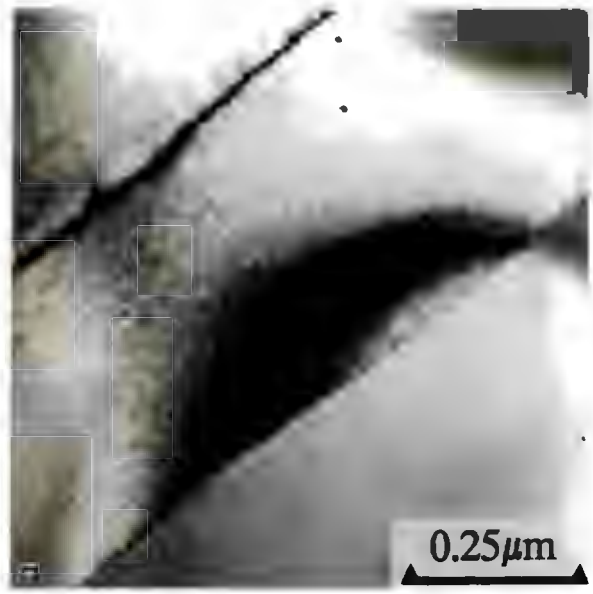

(b)

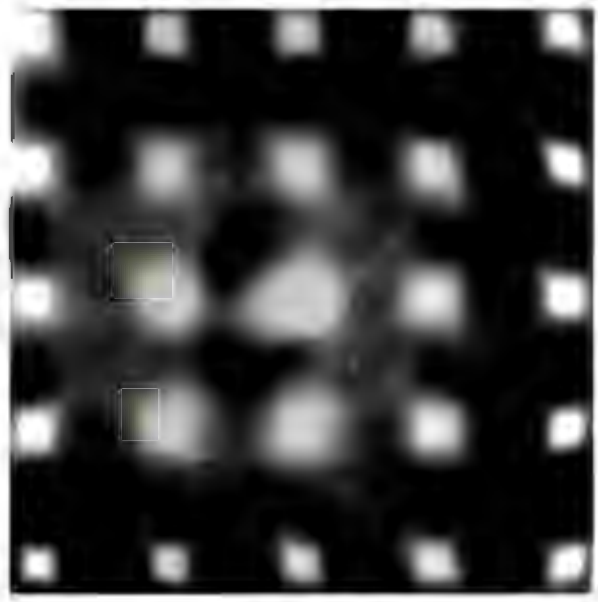

Fig. 4.20 (a) Bright-field TEM image from a typical electron transparent region in an as-solidified Au-2wt.% Ti ribbon; (b) long exposure [001] zone axis electron diffraction pattern.

Electron transparent areas from an as-solidified ribbon (fig. 4.20(a)) exhibit a fine grained homogeneous microstructure with no evidence of segregation or second phase formation. The isolated areas of strain contrast visible in fig. 4.20(a) are consistent with the presence of dislocation loops or stacking fault tetrahedra that may be expected to arise from the condensation of point defects in rapidly quenched alloys of this type [103]. As discussed in section 3.2.4, long exposure times, typically between 15 and 30 min, were required when taking diffraction pattens from these alloys in order to reveal the diffuse reflections and scattering present between the parent f.c.c. reflections. A long exposure [001] zone-axis diffraction pattern from an as-solidified ribbon is shown in fig. 4.20(b). The electron diffraction pattern exhibits no evidence of additional reflections arising from the presence of second phase precipitates beyond the resolution of the microscope. Careful examination of the original negative of this diffraction pattern reveals areas of diffuse intensity between the f.c.c. reflections similar to that seen in diffraction patterns from an as-solidified 3wt.% Ti alloy (fig. 4.27(b)). Although this diffuse scattering is related to the structural order present on solidification (see section 4.5), it is not indicative of the presence of precipitates; thus rapid solidification successfully suppressed the nucleation of the (D1a) Au_4Ti phase in this alloy.

A bright-field micrograph from a ribbon after heat treatment at 350°C for 1 h (fig. 4.21(a)) reveals evidence of strain contrast in the lattice, which is possibly associated with the presence of fine precipitates. A long exposure [001] zone-axis electron diffraction pattern from Au-2wt.% Ti after heat treatment at 350°C for 1 h (fig. 4.21(b)) exhibits superlattice reflections consistent with the presence of all of the in-plane orientational variants of the D1a structure expected from Au_4Ti (see fig. 2.11(a)). However, the precipitates could not be resolved by means of superlattice-centred dark-field imaging. On heat treatment at 350°C for 24 h, the superlattice reflections were more intense than those shown in fig. 4.21(b), but no precipitates were detectable in superlattice-centred dark-field images. Indeed, only after heat treatment at 500°C were the precipitates resolved; a bright-field/superlattice-centred dark-field pair of images from a sample heat treated at 500°C for 1 h is shown in fig. 4.22. The bright-field image shows contrast arising from the presence of strain in the lattice due to the presence of fine scale, approximately spherical precipitates imaged in fig. 4.22(b). The precipitates are homogeneously distributed throughout the microstructure with no evidence of local variations in precipitate density at regions adjacent to the grain boundaries. After heat treatment at 500°C for 24 h superlattice-centred dark-field images show some evidence of precipitate coarsening (fig. 4.23(b)), although the array of second phase particles is

still extremely fine. All of the distinguishable orientational variants of the structure are still present in electron diffraction patterns after this heat treatment.

(a)

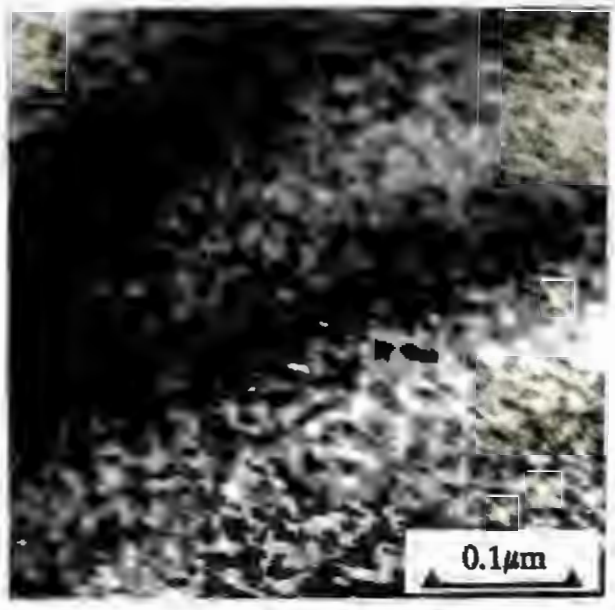

(b)

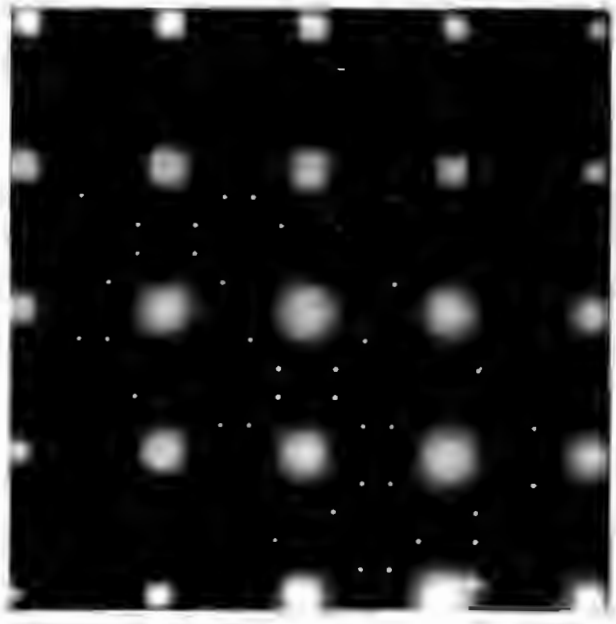

Fig. 4.21 Au-2wt.% Ti after heat treatment for 1 h at 350°C: (a) bright-field TEM image showing evidence of strain contrast; (b) [001] zone-axis electron diffraction pattern showing superlattice reflections resulting from the presence of dual variant (D1a) Au_4Ti precipitates.

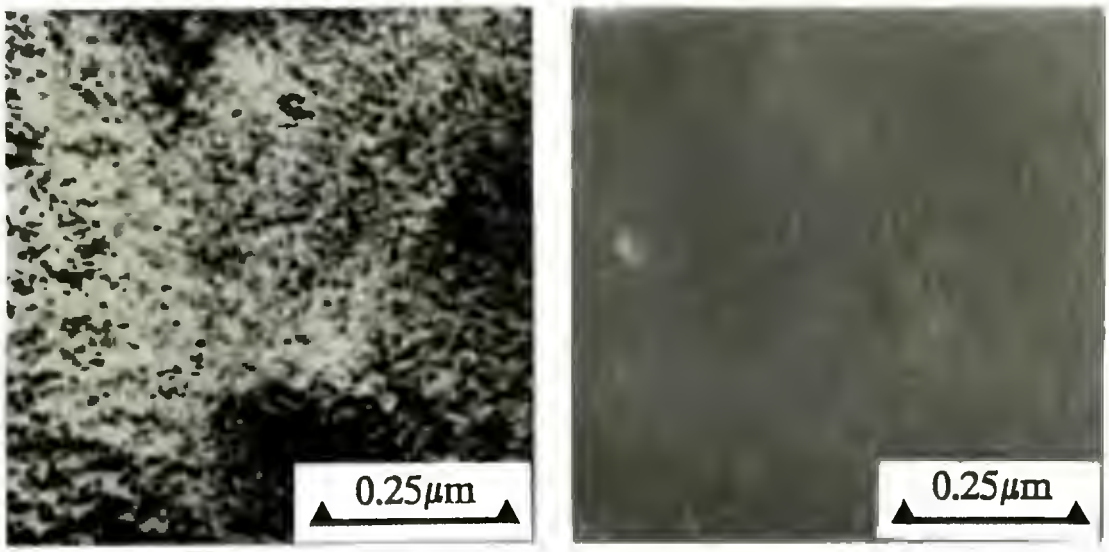

(a) (b)

Fig. 4.22 TEM images from Au-2wt.% Ti after 1 h at 500°C: (a) bright-field image; (b) superlattice-centred dark-field image.

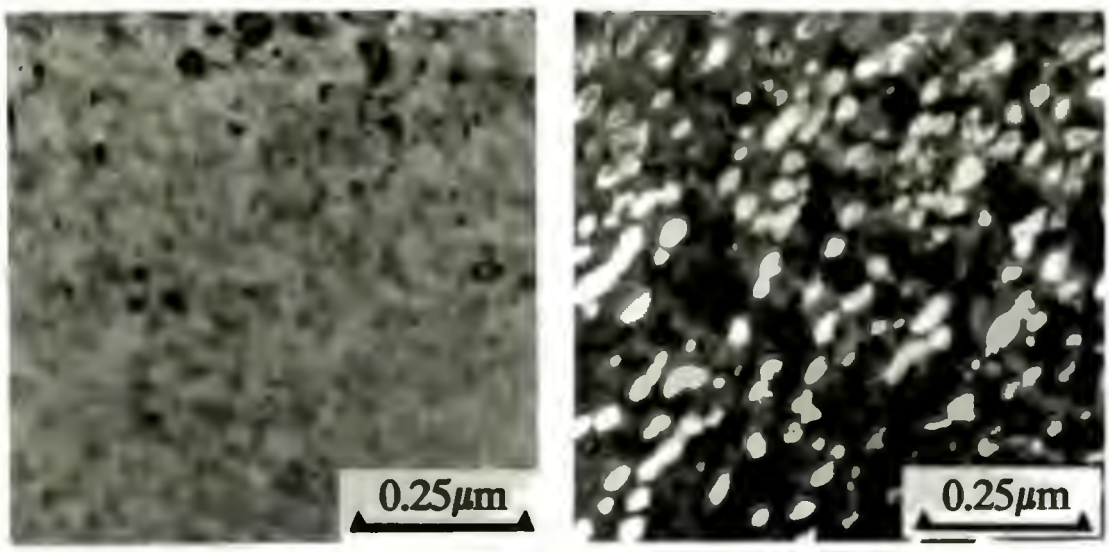

(a) (b)

Fig. 4.23 Au-2wt.% Ti after 24 h at 500°C: (a) bright-field image; (b) superlattice-centred dark-field image.

The Au_4Ti phase has a number of distinct orientational variants, only two of which are contained in a [001] zone-axis (see section 2.3.1). In order to determine whether all of the orientational variants of the structure are present a number of different zone-axes orientations were examined; a typical [112] zone-axis together with a schematic diffraction pattern showing the relative positions of the parent f.c.c reflections and the two in-plane orientational variants is shown in fig. 4.24. In each of the zone-axes examined from heat treated Au-2wt.% Ti samples all of the in-plane orientational variants of the D1a phase were present.

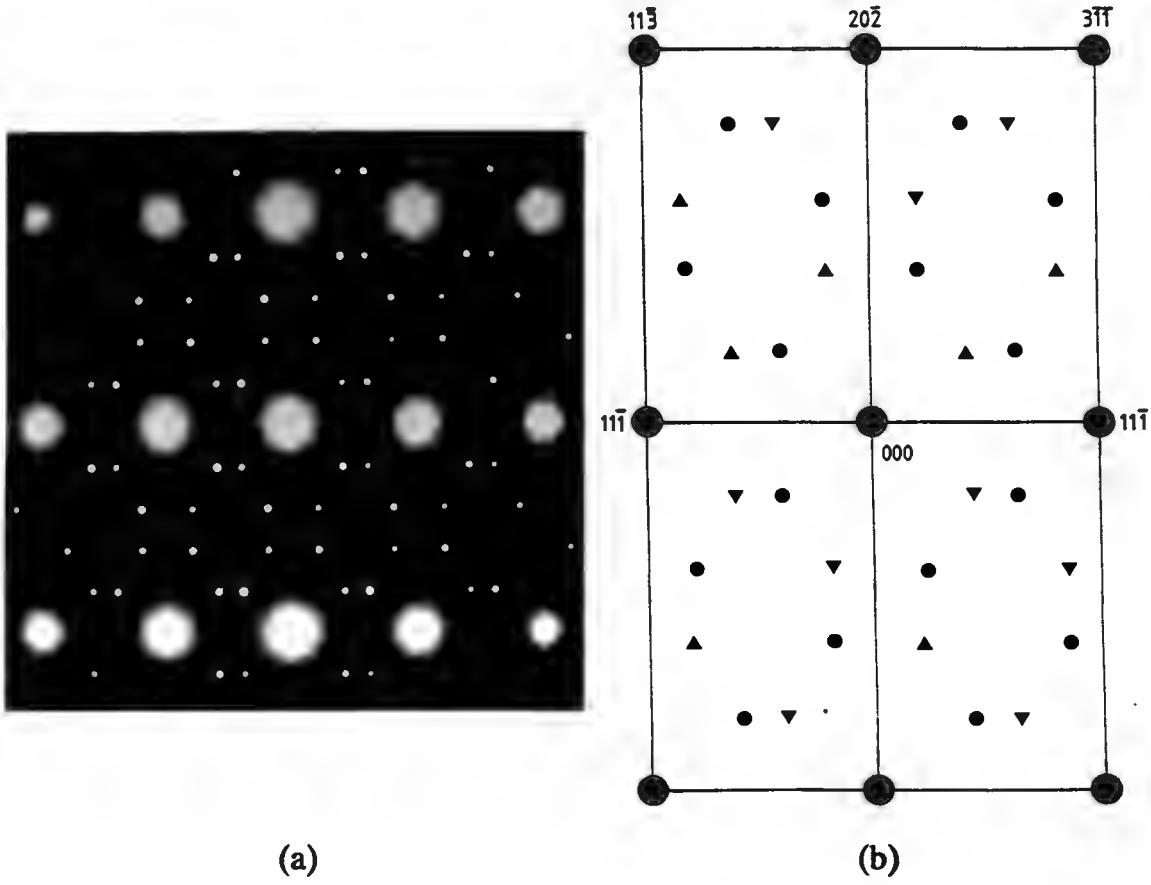

Fig. 4.24 [112] zone-axis diffraction patterns: (a) diffraction pattern from a heat treated 2wt.% Ti alloy showing superlattice reflections due to the presence of (D1a) Au_4Ti precipitates; (b) schematic zone-axis diffraction pattern showing the orientation relationship between the parent f.c.c. matrix (●) and two orientational variants of the (D1a) Au_4Ti phase (• and ▲).

4.4.3 Au-3wt.% Ti

A light micrograph of an etched cross-section from as-solidified Au-3wt.% Ti (fig. 4.25(a)) shows that the microstructure consists of columnar grains extending from the wheel-side surface (arrowed in the figure) through the ribbon thickness. SEM examination of an etched ribbon cross-section (fig. 4.25(b)) reveals that the entire transverse section of the ribbon consists of columnar grains with no evidence of equiaxed grains in the region of the free side of the ribbon. A tapered section of an as-solidified ribbon shows that the diameter of the columnar grains does not vary significantly as a function of distance from the wheel surface (fig. 4.25(c)). In addition, the tapered section from this alloy, unlike the tapered sections of the 1wt.% Ti and 2wt.% Ti alloys (fig. 4.8 and fig. 4.17 respectively), exhibits a single etching response across the entire ribbon thickness.

After heat treatment at 500°C for 24 h an etched cross-section of the ribbon still exhibits evidence of the columnar grain structure (fig. 4.26(a)), although the etching response of the microstructure was somewhat altered by this heat treatment. Nevertheless, there is sufficient evidence of the columnar grained structure to suggest that little grain growth occurred in this alloy on heat treatment for 24 h at 500°C (fig. 4.26(a)). An etched tapered section from an Au-3wt.% Ti ribbon after 24 h at 500°C (fig. 4.26(b)) shows that no growth in the diameter of the columnar grains has occurred.

The Au-3wt.% Ti ribbons contain areas which are electron transparent directly after solidification, thus allowing the microstructures in these regions to be studied in the TEM without use of conventional thinning techniques. A bright-field TEM image of a typical electron transparent region in the as-solidified alloy is shown in fig. 4.27(a). Electron diffraction patterns show the areas to be sufficiently thin for there to be no Kikuchi lines in diffraction patterns from the alloys. No evidence of surface oxide films was seen. A bright field TEM image from an as-solidified alloy (fig. 4.27(a)) reveals a fine grained microstructure with no evidence of strain contrast arising from the presence of precipitates. A long exposure electron diffraction pattern from as-solidified Au-3wt.% Ti (fig. 4.27(b)) contains considerable diffuse scattering between the parent f.c.c. lattice reflections. The shape of the diffuse scattering is reminiscent of that seen previously in quenched Au_4V (see section 2.2.3), where it was associated with the

(a)

(b)

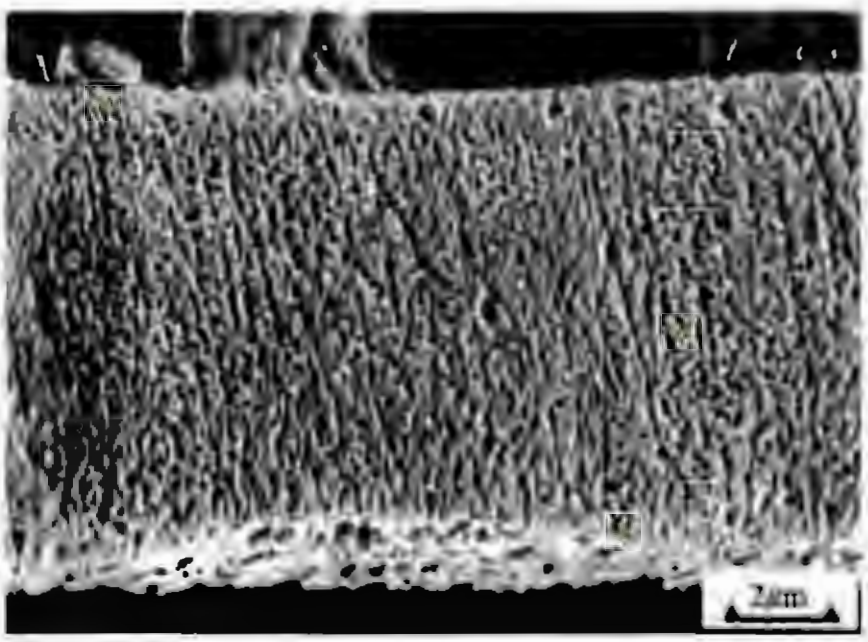

Fig. 4.25 Etched cross-sections from as-solidified Au-3wt.% Ti ribbons: (a) light micrograph; (b) secondary electron SEM image (the wheel-side surfaces of the ribbons are arrowed).

(c)

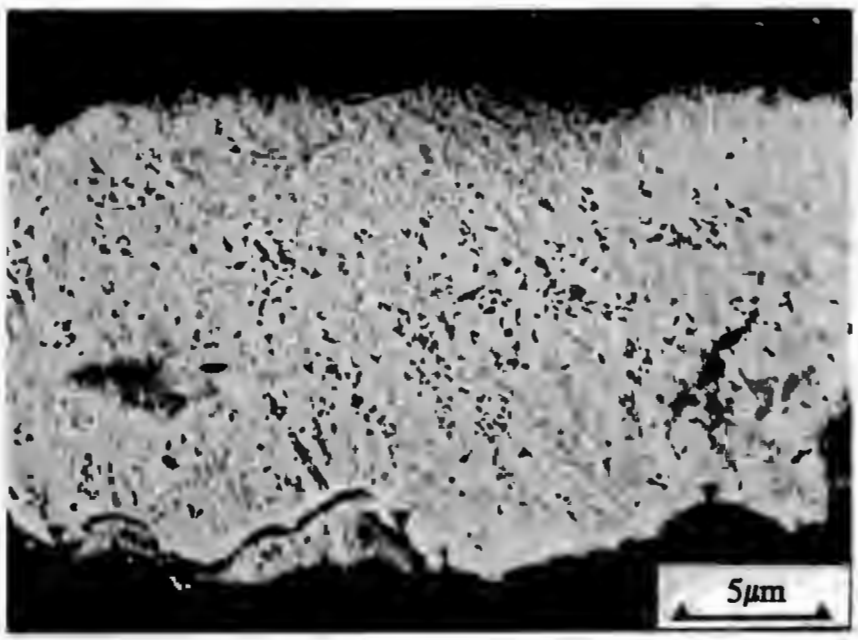

Fig. 4.25 (cont.) (c) Tapered section of an as-solidified 3wt.% Ti ribbon (the orientation of the section is illustrated in fig. 3.3). The wheel-side surface of the ribbon is arrowed.

presence of so-called $<1^1/_20>$ special-point order [87]. The details of the diffuse scattering in fig. 4.27(b) will be explored in detail in section 4.5; however, the diffuse scattering present in the diffraction pattern did not result from the presence of precipitates.

A bright field TEM image of the alloy after heat treatment at 350°C for 1 h shows evidence of strain contrast in the lattice due to the presence of precipitates (see fig. 4.28). The precipitates, however, could not be resolved by means of superlattice-centred dark-field images. Long exposure selected area diffraction patterns from the 3wt.% alloy contain superlattice reflections which are indexable on the basis of the presence of (D1a) Au_4Ti precipitates, i.e. the electron diffraction pattern is similar to

(a)

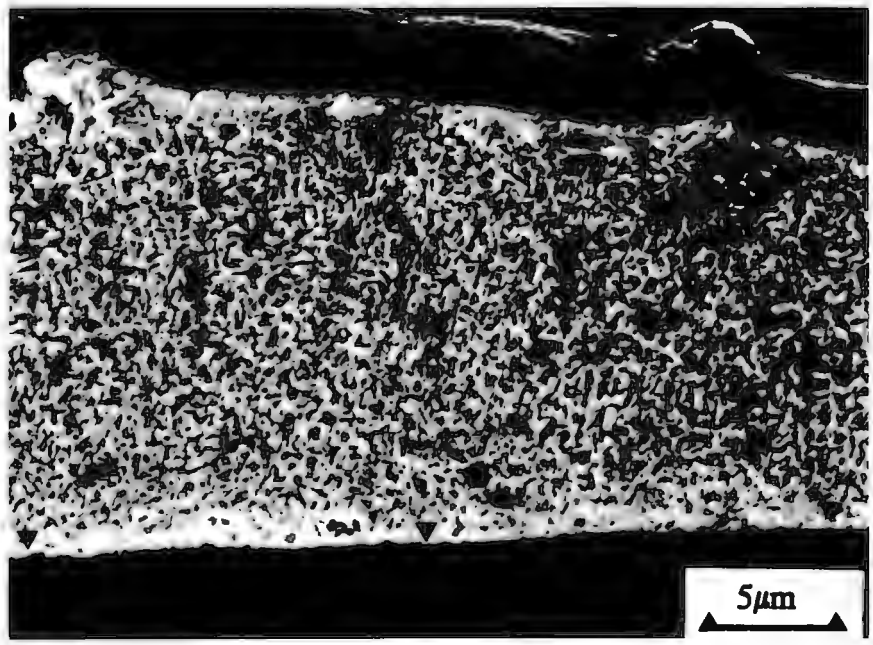

(b)

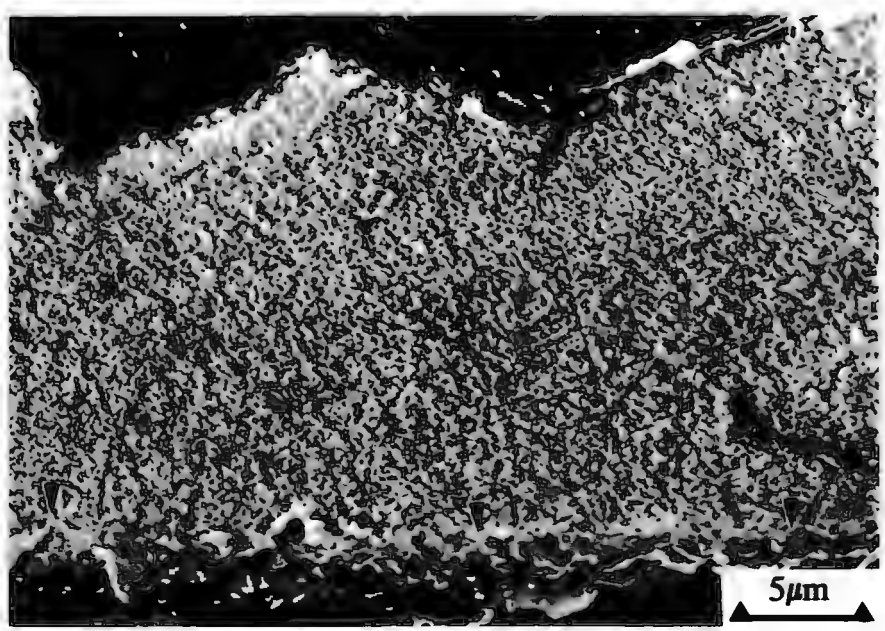

Fig. 4. 26 Secondary electron SEM images from etched Au-3wt.% Ti ribbon sections after heat treatment at 500°C for 24 h: (a) cross-section; (b) tapered section (the wheel-side surfaces of the ribbons are arrowed).

(a)

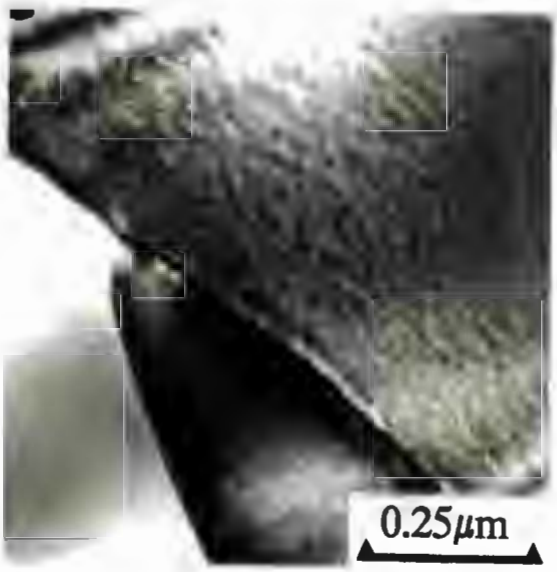

(b)

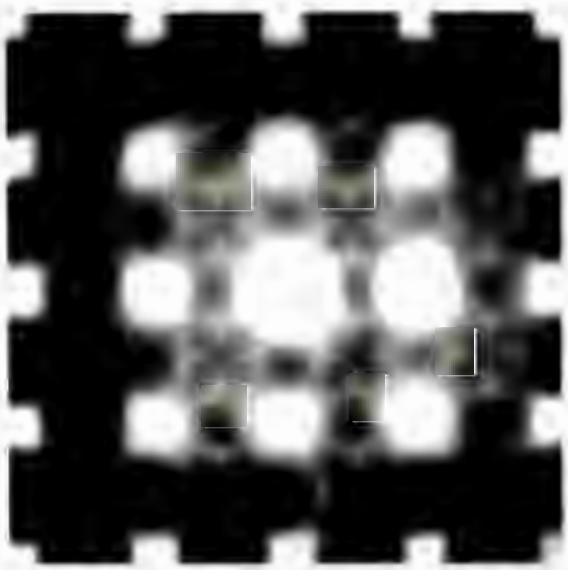

Fig. 4. 27 (a) Bright-field TEM image from a typical electron transparent region in a melt spun Au-3wt.% Ti alloy ribbon; (b) [001] zone-axis diffraction pattern from as-solidified Au-3wt.% Ti showing evidence of diffuse streaking between the fundamental f.c.c. parent lattice reflections.

Fig. 4.28 Bright-field TEM image from Au-3wt.% Ti after heat treatment at 350°C for 1 h.

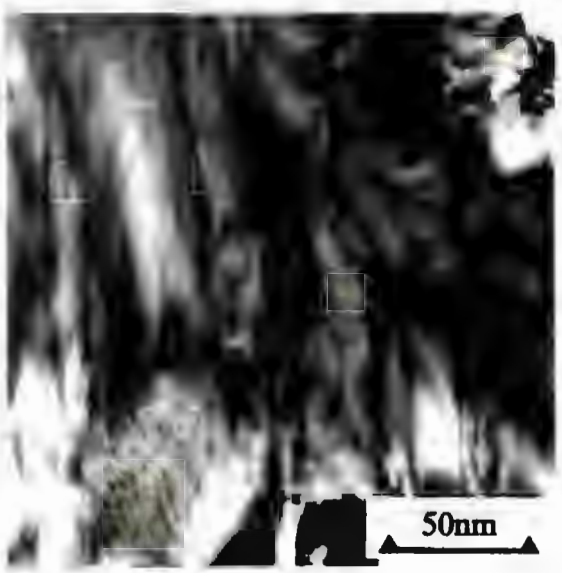

Fig. 4.29 Bright-field TEM image from Au-3wt.% Ti after heat treatment at 350°C for 24 h.

that shown in fig. 4.21. Examination of a number of diffraction patterns reveals that all of the orientational variants of this structure are present after 1 h at 350°C. All of the orientational variants are also seen in diffraction patterns after 24 h at 350°C; a bright-field TEM image from the ribbon after 24 h at 350°C is shown in fig. 4.29. Bright-field images of these samples exhibit strain contrast in the lattice consistent with the presence of precipitates. However, superlattice-centred dark-field images were not able to resolve the precipitates.

After 1 h at 500°C, all of the orientational variants of the (D1a) Au_4Ti phase are present and the precipitates can finally be resolved by means of dark field (fig. 4.30(b)). After 24 h at 500°C, however, significant changes in the precipitate morphology and size occur (fig. 4.31(b)). Interestingly, the observed change in precipitate morphology and size is associated with a change in the number of orientational variants of the D1a superlattice structure. The selected area diffraction patterns in fig. 4.31(c) and (d) show superlattice reflections consistent with the presence of only a single variant of the (D1a) Au_4Ti structure (see fig. 2.11(a) and fig. 4.24(b)). The change in precipitate shape and the strain contrast in the bright field image of this heat treated alloy suggest a loss of coherency of the precipitates in this alloy after 24 h at 500°C.

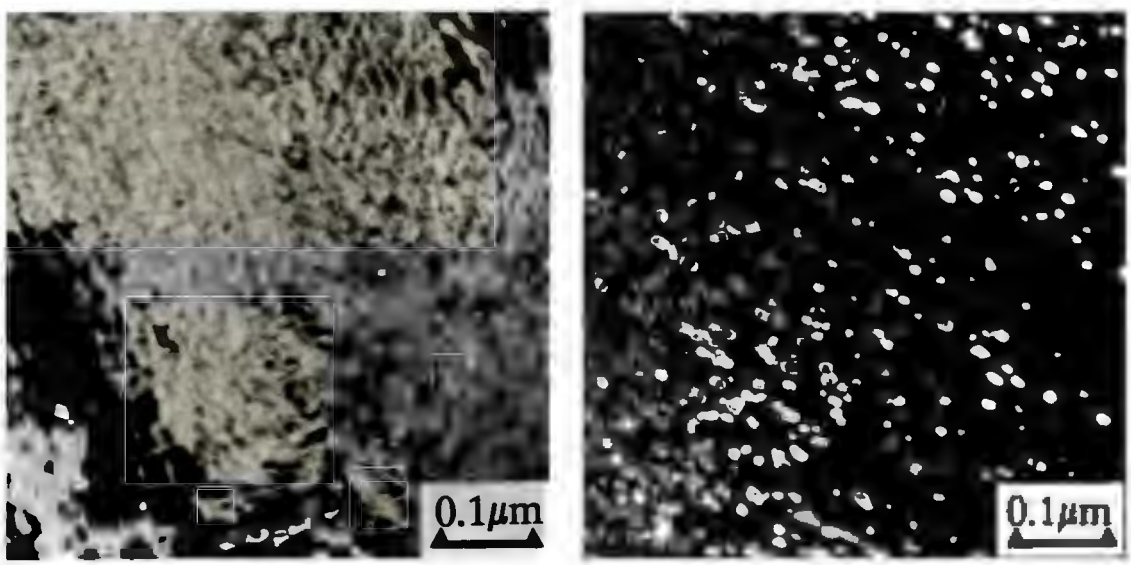

(a) (b)

Fig. 4.30 Au-3wt.% Ti after heat treatment at 500°C for 1 h: (a) bright field image; (b) superlattice-centred dark-field image.

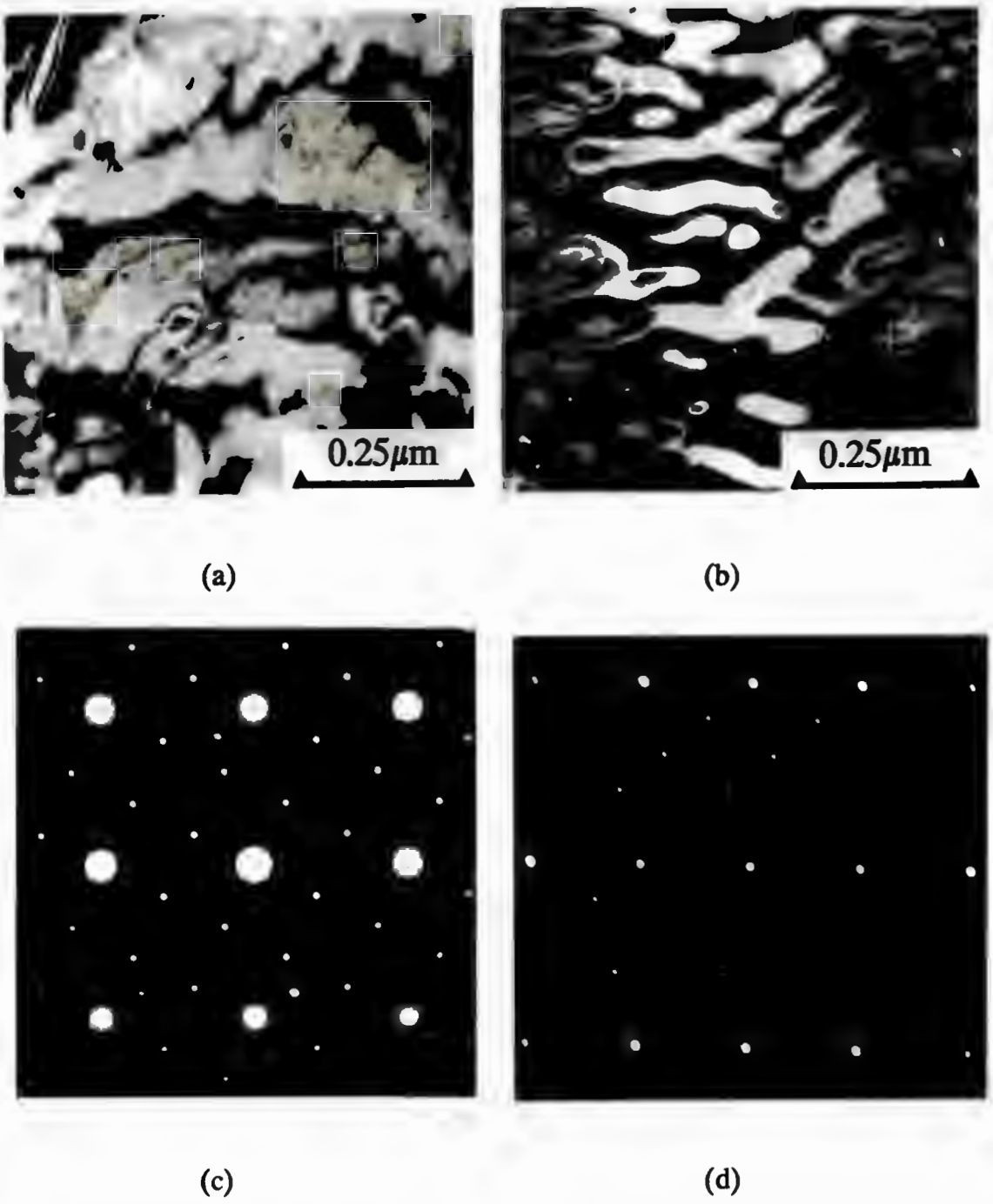

Fig. 4.31 Au-3wt.% Ti after heat treatment at 500°C for 24 h: (a) bright-field image; (b) superlattice-centred dark-field image; (c) [001] zone axis diffraction pattern; (d) [112] zone-axis diffraction pattern.

4.4.4 Au-5wt.% Ti

The rapidly solidified fragments of this alloy were too thin to be readily examined in cross-section by light microscopy. SEM examination of an etched cross-sections from as-solidified fragments of Au-5wt.% Ti shows the microstructure to vary considerably (fig. 4.32(a) and (b)). In some of the sections the entire section consisted of columnar grains extending through the ribbon thickness, while in other sections the fragment was made up entirely of large equiaxed grains. The cross-sectional microstructure was unaltered by heat treatment with both columnar grained and equiaxed regions again observed.

A bright-field TEM image from an electron transparent region present in an as-solidified 5wt.% Ti fragment directly on solidification shows evidence of strain in the lattice due to the presence of precipitates (fig. 4.33(a)). From the superlattice-centred dark-field image shown in fig. 4.33(b), the precipitates are numerous, small and approximately spherical. A long-exposure [001] zone-axis diffraction pattern illustrates that the long-range-ordered (D1a) Au_4Ti phase has nucleated during solidification (fig. 4.33(c)). Heat treatment resulted in extensive oxidation of the sample surface, precluding a study of the thermal stability and development of structural order present after heat treatment.

Examination of the diffraction pattern in fig. 4.33(c)) reveals that diffuse intensity maxima are visible at the $1^1/_20$ reciprocal lattice positions (see arrowed regions). As discussed in section 4.5, these reflections suggest that vestiges of special-point order are present in this as-solidified alloy; the significance of this observation is examined in more detail in the following section.

(a)

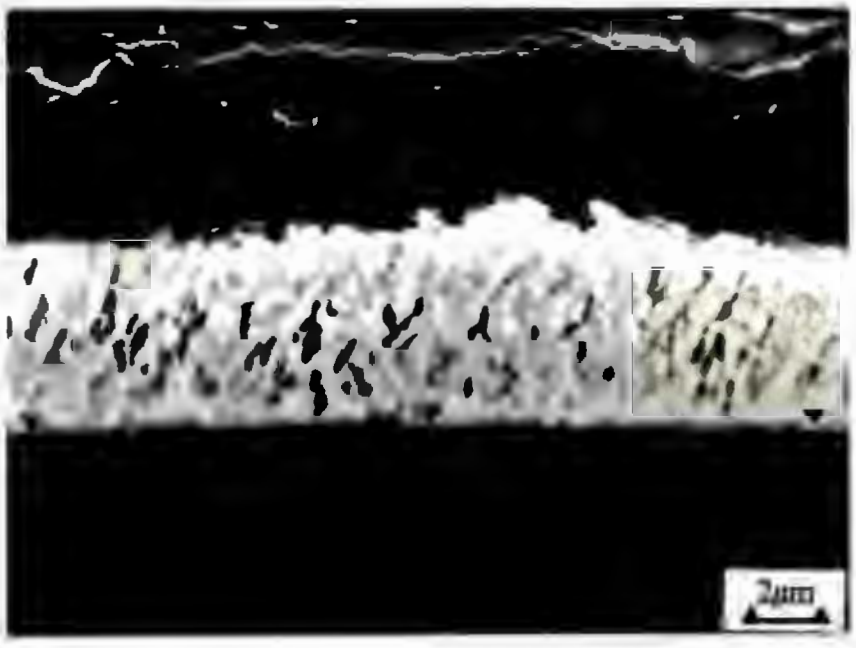

(b)

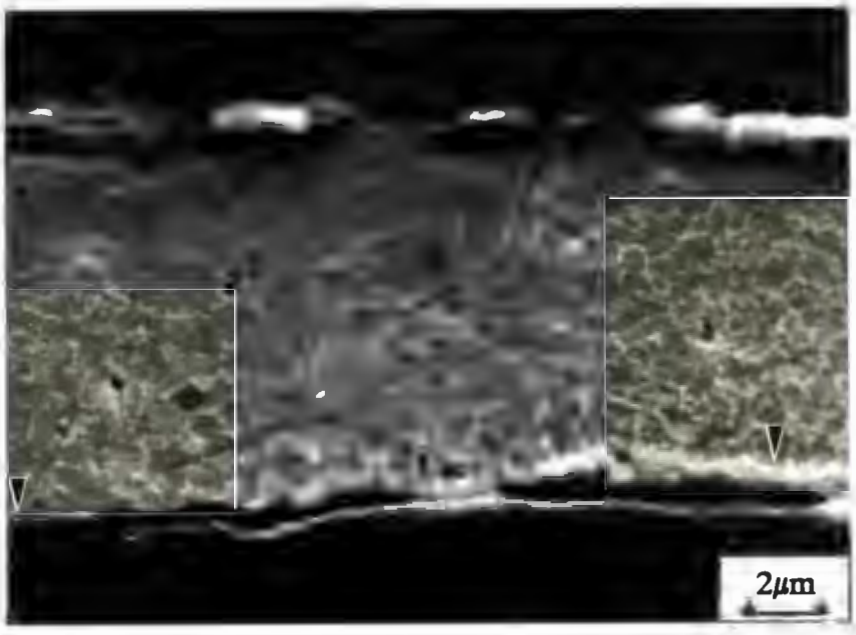

Fig. 4.32 Secondary electron SEM images of etched cross-sections from as-solidified Au-5wt.% Ti fragments showing examples of (a) columnar grained and (b) equiaxed grain morphologies. The wheel-side surfaces of the ribbons are arrowed.

(a)

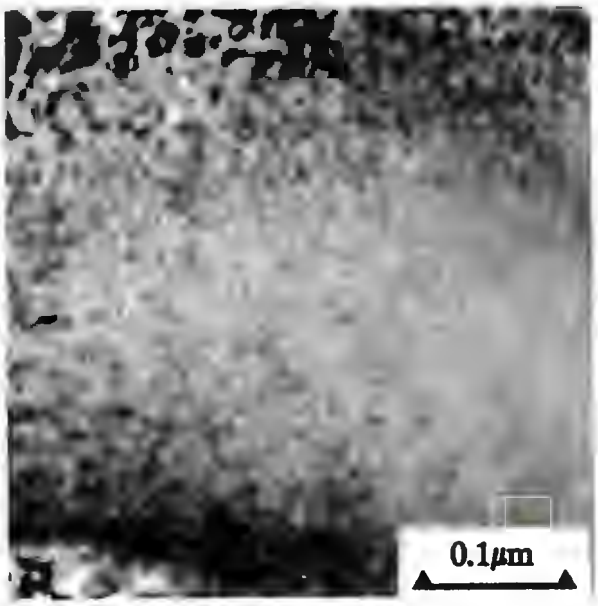

(b)

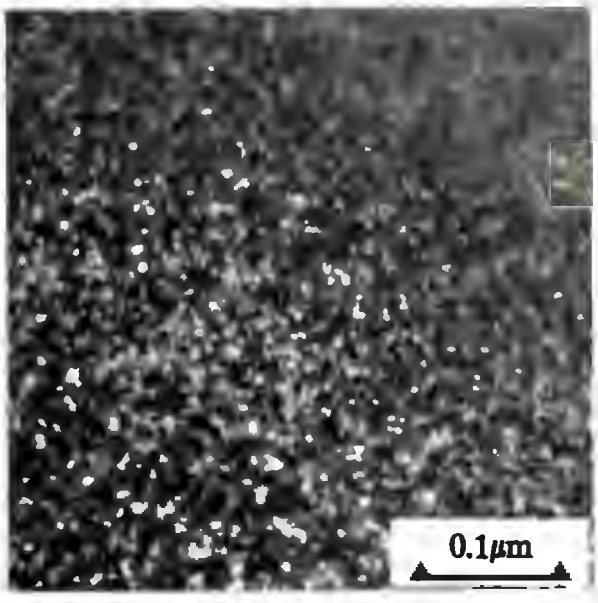

Fig. 4.33 TEM images of as-solidified Au-5wt.% Ti: (a) bright-field image; (b) superlattice-centred dark-field image from a long-range order (D1a) reflection showing small Au_4Ti precipitates.

(c)

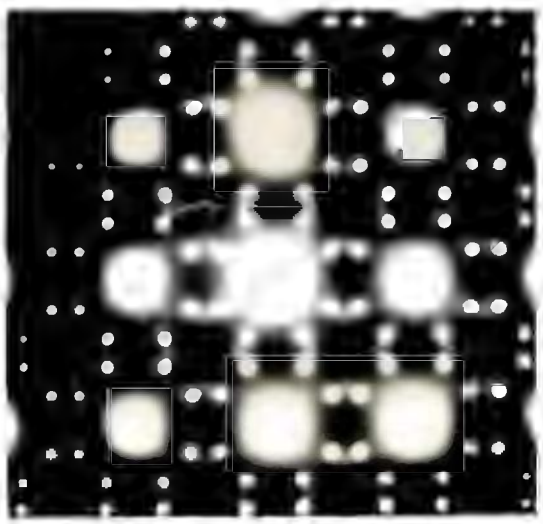

Fig. 4.33 (cont.) (c) [001] zone-axis electron diffraction pattern; a special-point order reflection at a $1^1/_2 0$-type position is arrowed.

4.5 STRUCTURAL ORDER IN THE AS-SOLIDIFIED ALLOYS.

The diffuse scattering in the electron diffraction patterns shown in fig. 4.33(c) and fig. 4.27(b) is similar to that associated with so-called special-point order (section 2.3.2). This state of order has been identified previously in a number of alloy systems possessing a long-range-ordered (D1a) structure at equilibrium, but which form so-called $<1^1/_2 0>$ special-point order on rapid quenching from a high temperature. Alloy systems which exhibit this state of order include Ni_4Mo, Au_4Cr, and Au_4V [27, 86, 87]. However, $<1^1/_2 0>$ special-point order has not been identified previously in Au-Ti alloys, and thus its characterisation and the subsequent transformation route on heat treatment are of considerable interest.

A [001] zone-axis electron diffraction pattern from as-solidified Au-5wt.% Ti (shown previously in fig. 4.33(c)) is reproduced in fig 4.34(a), together with a schematic zone-axis diffraction pattern showing the relative positions of the (D1a) long-range-ordered and $<1^1/_20>$ special-point order reflections (fig 4.34(b)). From the figure it is apparent that, in addition to the long-range order reflections, diffuse intensity maxima are detectable at the $1^1/_20$ reciprocal lattice positions (see arrowed regions), suggesting that vestiges of the special-point order are present. The presence of these special-point reflections implies that at high temperatures the structure exists predominantly as a random f.c.c. solid solution, as special-point order is known to be a specific feature of the transformation route from random to ordered structures in "special-point" alloys [104]. Direct evidence for this high temperature state of order requires the use of elevated temperature transmission electron microscopy, which was not available. Nevertheless, these reflections suggest that the Au-Ti system is a member of the $<1^1/_20>$ special-point family of alloys.

Unlike Au-5wt.% Ti, [001] zone-axis patterns from as-solidified Au-3wt.% Ti (shown previously in fig. 4.27(b), and reproduced in fig. 4.34(c)) and Au-2wt.% Ti (fig. 4.20(b)) exhibit no evidence of nucleation of the long-range-ordered (D1a) equilibrium phase. Examination of fig. 4.34(c)) from Au-3wt.% Ti reveals triangular regions of diffuse intensity centred on the $1^1/_20$ reciprocal lattice positions (see fig. 4.34(b)). In fig. 4.34(d)) the relative positions of the special-point order reflections and (D1a) long-range order reflections are superimposed on the diffuse scattering observed in fig. 4.34(c)). The figure shows that two vertices of the triangular region of diffuse intensity are situated on the two adjacent in-plane reciprocal lattice positions of the long-range-ordered (D1a) structure. The third vertex corresponds to the projected position of other variants of the D1a structure whose reflections are situated above and below the [001] zone-axis pattern zero-order reciprocal lattice plane (see fig. 2.11(b)). Careful examination of fig. 4.20(b) reveals faint traces of the diffuse scattering seen in fig. 4.34(c) (the diffuse scattering was clearly observable on the original negative). The shape of the diffuse streaking in both of the alloys is reminiscent of that seen previously in as-solidified Au-V alloys [87], although, as will be discussed later, it differs somewhat in detail.

(a)

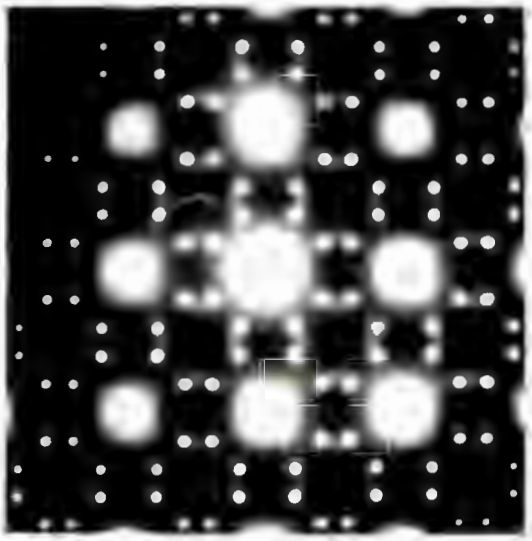

(b)

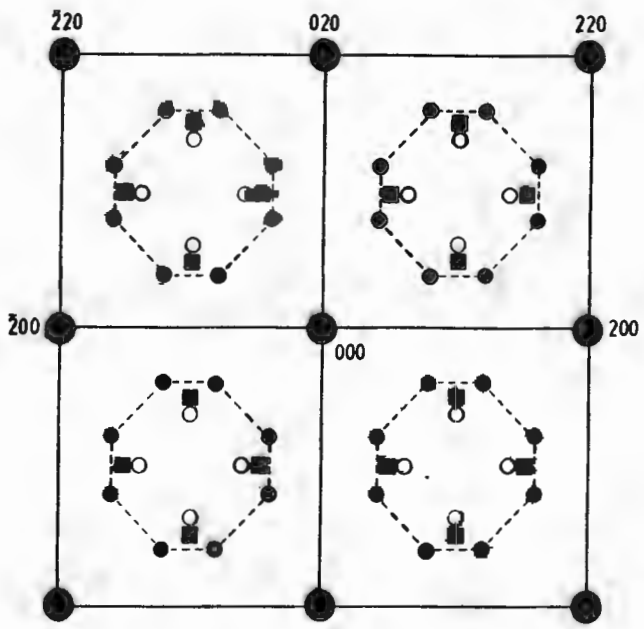

Fig. 4.34 (a) [001] zone-axis electron diffraction pattern from Au-5wt.% Ti; a special-point order reflection at a $1^1/_20$ type position is arrowed. (b) Schematic representation of [001] zone-axis diffraction pattern showing the relative positions of the parent f.c.c. matrix reflections (●), $<1^1/_20>$ special-point order reflections (■) and long-range order (D1a) Au_4Ti reflections (•). The projected D1a out-of-plane reflections are indicated by (○).

(c)

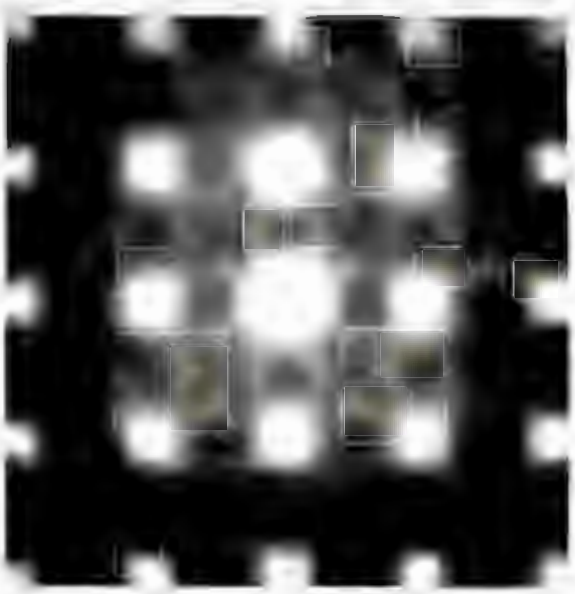

(d)

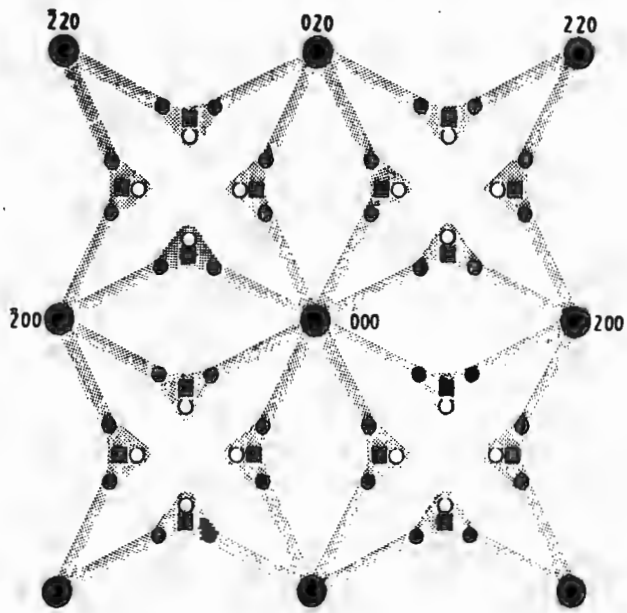

Fig. 4.34 (cont.) (c) [001] zone-axis diffraction pattern from Au-3wt.% Ti. (d) Schematic representation of (c) showing the expected positions of the special-point order and (D1a) long-range order reflections (designation of symbols as in fig. 4.34(b)).

In order to determine the three-dimensional spatial configuration of the diffuse scattering from Au-3wt.% Ti, electron diffraction patterns were obtained from several different zone-axis orientations. A [112] zone-axis diffraction pattern is shown in fig. 4.35(a), while in fig 4.35(b) a schematic [112] zone-axis pattern illustrating the relative positions of the expected in-plane (D1a) long-range order and $1^1/_20$ type reflections, as well as the fundamental f.c.c. reflections, is shown. Significant streaking occurred between the $1^1/_20$ reciprocal lattice positions and the adjacent long-range order positions, i.e. the $1^1/_20$ reflections have "wings" (fig. 4.36). Intensity maxima can also be seen at the other non-adjacent long-range order positions in the pattern. However, each of these long-range order (D1a) reflections is associated with an off-plane $1^1/_20$ type reflection, as may be seen by examining fig. 2.11(b), and is thus probably streaked towards the closest adjacent special-point $1^1/_20$ position. The streaking in question suggests that an intermediate state of order between the equilibrium D1a and $<1^1/_20>$ special-point order is present. Indeed, re-examination of the triangular regions of diffuse scattering seen in fig. 4.34(c) shows that the scattered intensity is concentrated in streaks between the $1^1/_20$ positions and the long-range order (D1a) positions, with little streaking linking the D1a positions directly.

Streaking is not only evident between the $1^1/_20$ and long-range order (D1a) reciprocal lattice positions; it is also apparent between the $1^1/_20$ positions and the fundamental f.c.c. lattice positions (fig. 4.34(c)). The visibility of this streaking is dependent upon specimen thickness, as may be seen by comparing the [112] zone-axis pattern in fig. 4.35(a) with the pattern taken from a thicker grain shown in fig. 4.36. By examining several zone-axis orientations, the three-dimensional spatial distribution of this particular streaking was found to consist entirely of streaks joining the $1^1/_20$ positions to the fundamental f.c.c. lattice positions (fig. 4.37). This streaking was discrete and apparently circular in cross-section, as is evident from a close examination of the arrowed D1a reciprocal lattice positions in fig. 4.35(a). The implications of this suggested three-dimensional distribution of diffracted intensity with regard to the applicability of the models of Stobbs and Stobbs [93] and de Ridder *et al.* [87] to the Au-Ti alloy system are addressed in section 5.4.

In addition to the streaking detailed above, a number of the diffraction patterns obtained from Au-3wt.% Ti, and occasionally from Au-2wt.% Ti, were found to contain additional intensity maxima, particularly in the [001] and [112] zone-axis orientations.

(a)

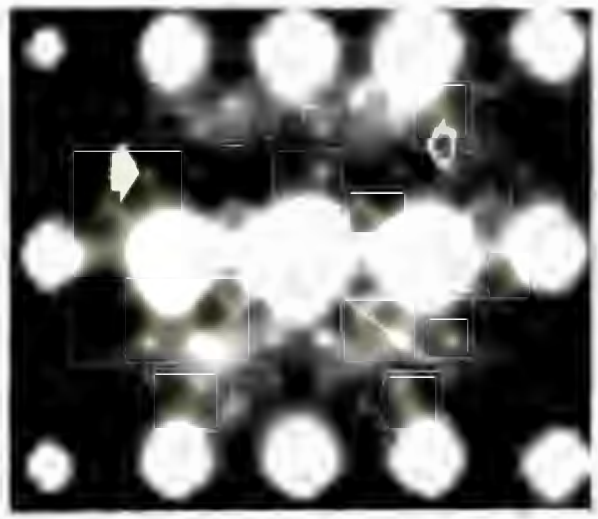

(b)

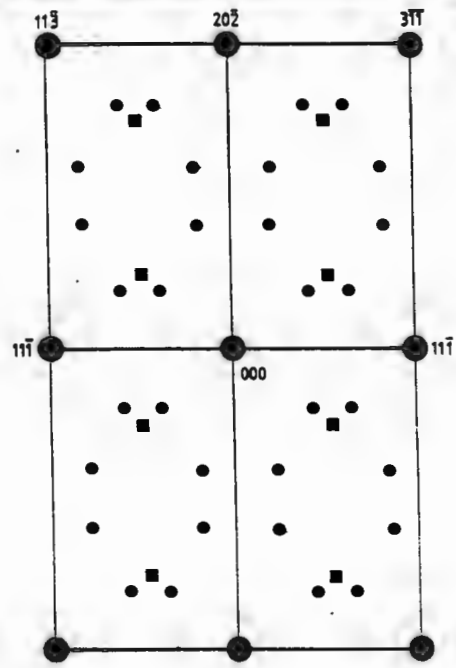

Fig. 4.35 [112] zone-axis electron diffraction patterns: (a) diffraction pattern from as-solidified Au-3wt.% Ti, the diffuse reflections at 110 positions are indicated by an unshaded arrow; (b) schematic zone-axis diffraction pattern (designation of symbols as in fig. 4.34(b)). Comparison of the figures shows that the special-point order reflections at $1^1/_2 0$ type positions are streaked toward the adjacent (D1a) long-range order reflections, i.e. the special-point order reflections have "wings". An example of a (D1a) long-range order reflection in (a) which is *not* associated with an in-plane special-point order reflection is indicated by a solid arrow.

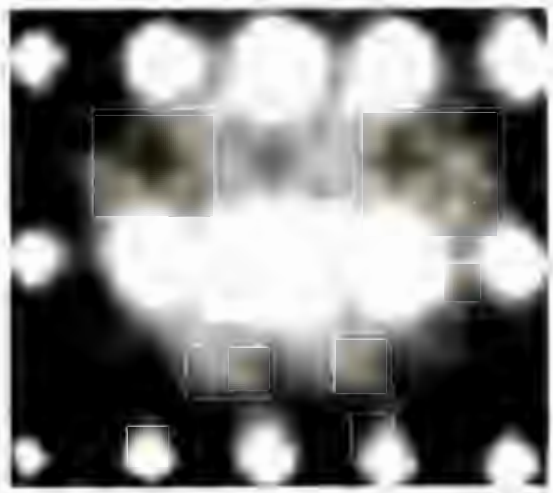

Fig. 4.36 [112] zone-axis electron diffraction pattern from Au-3wt.% Ti taken from a thicker region than that shown in fig. 4.35(a), illustrating the thickness dependence of the visibility of the streaking.

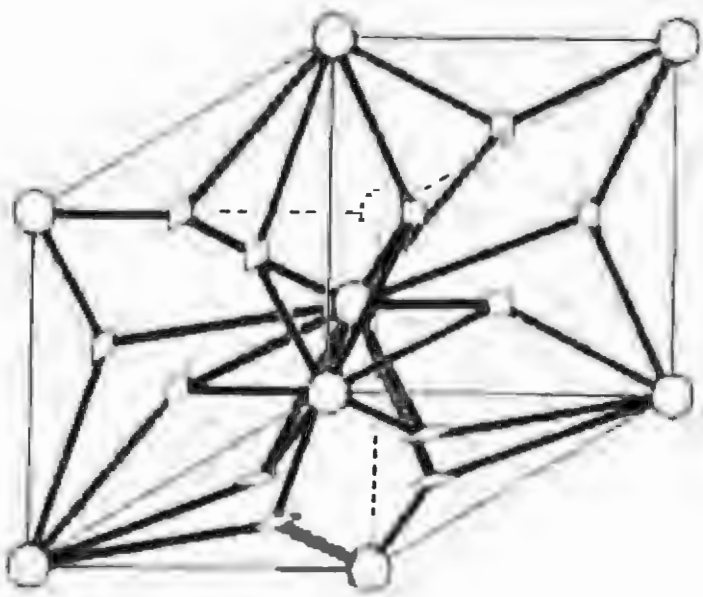

Fig. 4.37 A schematic representation of the spatial distribution of the diffuse streaking present in the background of diffraction patterns taken from as-solidified Au-3wt.% Ti. The positions of the f.c.c. parent reflections (○) and $<1\frac{1}{2}0>$ special-point order reflections (□) are indicated.

Fig. 4.38(a) is an example of a [001] zone-axis pattern which shows an additional reflection at 110 type positions (arrowed). Similar reflections have been seen previously by Van Tendeloo *et al.* [92] in lightly aged Au-Cr alloys, and were cited as evidence for the presence of elements of DO_{22} structural order in the lattice, in this case with the c-axis of the DO_{22} structure parallel to the zone-axis orientation. Careful examination of fig. 4.35 reveals faint intensity maxima at the 110 positions (arrowed in figure) in this [112] zone-axis orientation (as is often the case, the faint reflections are more clearly visible on the negative than on the printed reproduction - despite efforts to maximise the quality of the print). This suggests that, if the projected shape of the intensity maxima in 110 positions in the two orientations presented in fig. 4.35(a) and fig. 4.38(a) are compared, the reflections are approximately three-dimensionally spherical. The [112] zone-axis diffraction pattern in fig. 4.38(b) shows additional reflections at $^3/_2{}^1/_2{}^1/_2$ type positions (arrowed in the figure). Faint reflections in these positions have been seen previously by Chevalier and Stobbs [105] in lightly aged Ni-Mo alloys, but no explanation was offered for their presence. The most likely source is the intersection of the zero-order [112] zone-axis pattern plane with the streaking of off-plane 100 and 111 fundamental f.c.c. lattice reflections in the <111> direction. Evidence for streaking in the <111> direction may be seen in the fundamental lattice reflections in fig. 4.38(b).

It was necessary to identify all reflections present in every zone-axis pattern examined in order to ensure that there was no significant contribution to the diffraction patterns from oxide films. Oxide rings were seen in diffraction patterns from a few of the grains which had been tilted to large angles to the foil normal (fig. 4.39). Nevertheless, comparison of the diffraction patterns with those obtained from electropolished foils from Ni-Mo, Au-Cr and Au-V (see e.g. [81, 86, 87, 105]) indicates that the observed diffuse scattering is not due to surface artifacts, but is indeed a result of the state of order in the alloy.

A series of heat treatments were performed to determine the thermal stability of the order observed in the as-solidified alloys. No changes in diffuse scattering intensity distribution were seen in Au-2wt.% Ti or Au-3wt.% Ti at temperatures of up to 330°C for times of up to 24 h. However, at a temperature of 340°C after 1 h, nucleation of the (D1a) long-range-ordered phase was found to have occurred in both alloys with no discernible remnants of the diffuse scattering (refer to fig. 4.21). This result is

(a)

(b)

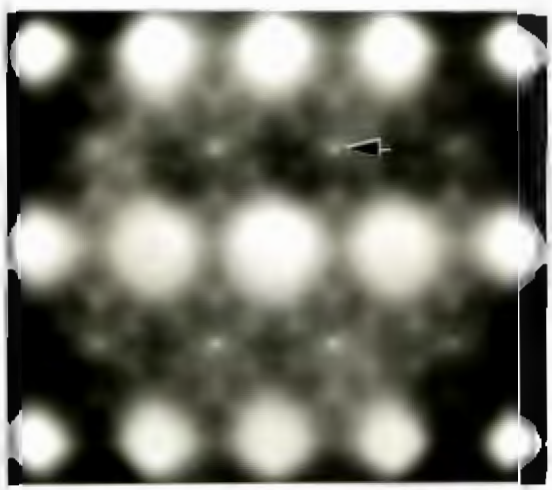

Fig. 4.38 Zone-axis electron diffraction patterns from as-solidified Au-3wt.% Ti: (a) [001] orientation, additional reflections at the 110 positions are arrowed; (b) [112] orientation, additional reflections at the $^{3}/_{2}{}^{1}/_{2}{}^{1}/_{2}$ positions are arrowed.

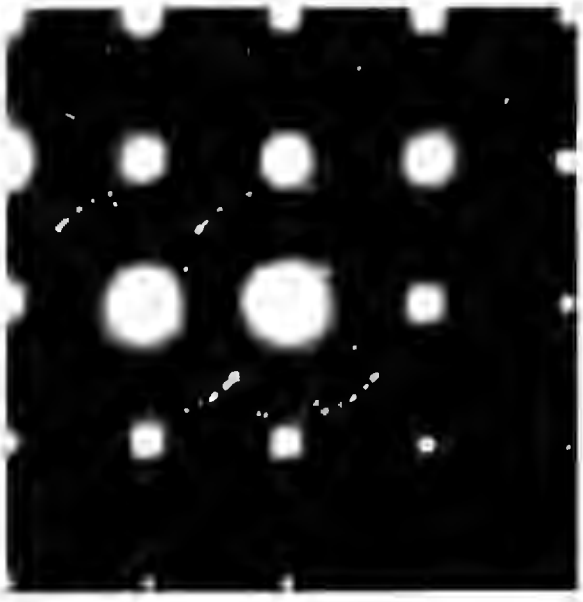

Fig. 4.39 [001] zone-axis electron diffraction pattern from as-solidified Au-3wt.% Ti tilted at a large angle to the foil normal.

somewhat surprising when compared with previous studies on similar materials [81, 86, 87, 105] and suggests that the as-solidified state of order possesses significant thermal stability up to temperatures of at least 330°C.

4.6 SUMMARY OF EXPERIMENTAL RESULTS

In the preceding sections the experimental results were loosely grouped according to experimental technique to facilitate direct comparison of the data from the various alloys. To allow the evolution of the microstructure and properties of each of the alloys on heat treatment to be followed readily, the results will be summarised in this section by alloy composition.

(a) Au-1wt.% Ti

Chemical analyses showed that the rapidly solidified ribbons of this alloy contained approximately 0.6wt.% Ti after CBMS, implying that a significant amount of Ti was lost during processing. The ribbons formed on CBMS were thicker than those of the other alloys as a result of the superior flow characteristics of this alloy when molten. The cross-section microstructures of the as-solidified ribbons consisted of three distinct regions: a region immediately adjacent to the wheel-side surface of the ribbon which showed little response to etching, a region of columnar grains extending approximately 10 μm into the ribbon thickness and finally a region of equiaxed grains extending to the free surface of the ribbon. A tapered section of an as-solidified ribbon showed a continuous coarsening of the grain size through the ribbon section with no discontinuity in grain size at the surface between the columnar and equiaxed grains. TEM examination of electron transparent regions prepared by electropolishing revealed no evidence of segregation of Ti or second phase formation in either the columnar grained or equiaxed regions of the as-solidified ribbons.

No thermal events were detected in this alloy by means of DSC on heating to 600°C. No evidence of second phase nucleation was seen in the heat treated ribbons, although considerable grain growth occurred on heat treatment at temperatures exceeding 350°C. The grain growth resulted in the microhardness of the alloy decreasing on post-solidification heat treatment. Thus, although rapid solidification successfully suppressed segregation of Ti, the loss of Ti during processing resulted in there being no detectable precipitation of second phase on heat treatment.

(b) Au-2wt.% Ti

Chemical analysis of this alloy revealed that a small amount of Ti was lost during processing (measured Ti content: 1.9wt.% Ti). The ribbons formed on CBMS were considerably thinner than those of the 1wt.% Ti alloy, suggesting a deterioration of the flow characteristics of the melt with increasing Ti content. Etched sections from the as-solidified ribbons revealed that the microstructure consisted predominantly of columnar grains extending from the wheel-side to the free surface of the ribbon, with a small region immediately adjacent to the wheel-side of the ribbon which showed a limited response to etching. The rapidly solidified ribbons contained a large number of perforations through their thickness preventing conventional electropolishing

techniques being used for preparing TEM specimens. TEM examination of "as-solidified" electron transparent regions of these ribbons showed no evidence of precipitation or second phase formation. Long-exposure electron diffraction patterns taken from these electron-transparent regions exhibited evidence of diffuse scattering between the parent f.c.c. reflections. The distribution of this scattering suggested that an intermediate state of order, containing elements of the long-range-ordered D1a structure and elements of so-called "special-point" order, was present in these alloys directly on solidification.

DSC revealed that, on heating, a transformation occurred at approximately 320°C. Evidence of an additional thermal event was seen at approximately 500°C. Examination of ribbons after heat treatment at 350°C revealed that the transformation detected by DSC at 320°C was the precipitation of (D1a) Au_4Ti. The precipitation of this phase resulted in the microhardness of the alloy increasing steadily with increasing time at 350°C. However, although evidence of contrast arising from strain in the lattice was observed in bright-field TEM images, no precipitates were resolved. On heat treatment at 500°C for 1 h, the precipitates were small, spherical and evenly distributed. The presence of these precipitates resulted in a significant increase in the microhardness of the alloy. On heat treatment at 500°C for 24 h the precipitates coarsened, with a commensurate decrease in the relative microhardness of the alloy. Comparison of the grain size in an etched cross-section of the ribbon to that of the as-solidified ribbon indicated that no grain growth occurred in the 2wt.% Ti alloy on heat treatment.

Although the large number of perforations through the ribbon thickness prevented the preparation of electropolished foils, the TEM study of "as-solidified" electron transparent regions, in conjunction with the observed increase in the mechanical properties of the alloy on heat treatment, suggested that little segregation of Ti occurred during rapid solidification of this alloy.

(c) Au-3wt.%Ti

Chemical analyses of this alloy after CBMS revealed that the ribbons contained approximately 2.6wt.% Ti. The ribbons formed by melt spinning this alloy were short and showed considerable variation in their width and thickness, suggesting that the molten alloy had poorer flow characteristics than either the 1wt.% Ti or 2wt.% Ti

alloys. Examination of etched sections showed that the ribbon microstructure consisted of columnar grains extending through the ribbon thickness. As in the 2wt.% Ti alloy, only "as-solidified" electron transparent regions could be examined, as the ribbon quality prohibited conventional electropolishing being used for preparing TEM specimens. "As-solidified" electron transparent regions showed a fine grained microstructure with no evidence of second phase formation or segregation of Ti. Long-exposure electron diffraction patterns from these regions (as for the 2wt.% Ti alloy) exhibited diffuse scattering between the parent f.c.c. reflections. The distribution of the diffuse scattering was consistent with the presence of an intermediate state of order containing elements of the long-range-ordered D1a structure and elements of special-point order. Furthermore, additional reflections in some of the diffraction patterns from this alloy indicated that the DO_{22} structure was contributory to the special point order present in this alloy.

DSC showed that, on heating, thermodynamic events occurred in the alloy at approximately 320°C and 480°C. As was shown by examination of ribbons on heat treatment at temperatures between 300°C and 350°C, the former event was associated with the nucleation of the long-range ordered (D1a) Au_4Ti phase. The microhardness of the alloy increased on heat treatment at 350°C for 1 h; however, more extended heat treatments resulted in no further change in alloy microhardness. Electron diffraction patterns suggested that there was no change in the amount of Au_4Ti present between 1 h and 24 h at 350°C. However, the precipitates could not be resolved using dark-field imaging.

Heat treatment at 500°C for 1 h resulted in a dramatic increase in the alloy microhardness; however, the microhardness decreased after longer times at this temperature. After 1 h at 500°C the Au_4Ti precipitates were small, spherical and evenly distributed in the microstructure. After 24 h at 500°C the precipitates became irregularly shaped with reduced associated coherency strains. The change in shape was accompanied by a change in the number of orientational variants on the D1a structure. Examination of etched section form the ribbons after heat treatment at 500°C for 24 h showed that the grain size was unaltered by this heat treatment.

Although the poor quality of the ribbons prohibited a comprehensive study of the distribution of Ti through the ribbon thickness, as in the 2wt.% Ti alloy CBMS of the 3wt.% Ti alloy produced highly supersaturated alloys with little evidence of segregation

of Ti or second phase precipitates.

(e) Au-5wt.% Ti

Analyses revealed that Ti was lost during CBMS of this alloy; the final alloy composition was approximately 4.6wt.% Ti. Melt spinning produced only a small quantity of flakes of material, suggesting that the flow characteristics of this alloy when molten were the poorest of the alloys examined. Etched cross-sections of the as-solidified flakes revealed that the microstructures varied considerably with some flakes consisting entirely of columnar grains and others entirely of equiaxed grains. TEM examination of "as-solidified" electron transparent regions of the flakes showed that Au_4Ti had precipitated during the rapid solidification of this alloy. The precipitates were small, and evenly distributed through the microstructure. In addition to these precipitates, electron diffraction patterns from the as-solidified alloy contained diffuse reflections consistent with the presence of so-called "special-point order"; thus clearly demonstrating that this alloy is a member of the special-point order family of alloys.

Heat treatment at temperatures of up to 500°C resulted in no change in the cross-sectional microstructures of these alloys. However, excessive oxidation of the "as-solidified" electron transparent regions of this alloy prevented a TEM investigation of the evolution of the microstructure of this alloy as a function of heat treatment.

-ooOoo-

CHAPTER 5

DISCUSSION

In this chapter the techniques applied in the course of this work are discussed and the implications of the associated results examined. In section 5.1 the solidification conditions prevalent during CBMS are discussed on the basis of a macroscopic examination of the as-solidified ribbons. The microstructural consequences of the solidification conditions are addressed in section 5.2, while in section 5.3 the response of the as-solidified microstructures to post-solidification heat treatment is examined. In section 5.4 the structural order present in the as-solidified alloys is discussed in conjunction with the existing published literature concerned with special-point order in other alloy systems. In section 5.5 the most important unresolved issues arising from the work are raised.

5.1 SOLIDIFICATION CONDITIONS DURING CBMS OF THE Au-Ti ALLOYS

Although all of the alloys examined were prepared by CBMS under identical processing conditions, the conditions prevalent at the solidification front were not necessarily the same for all of the alloys. In this section the variations in the solidification conditions with alloy composition are discussed on the basis of a macroscopic examination of the melt spun materials. In addition, the physical mechanisms underlying the observed variations in ribbon dimensions and quality as a function of alloy content are addressed.

The geometrical and visual uniformity of the melt spun ribbons deteriorates and the dimensions of the ribbons decrease with increasing Ti content (fig. 4.1). These effects arise from a decrease in the flow rate of the melt through the nozzle with increasing Ti content (table 4.1). As identical expulsion pressures were used during the processing of all the alloys, the observed decrease in flow rate with increasing solute content is indicative of a deterioration in the flow characteristics of the melt with increasing Ti concentration. This implies that the melt does not act as an inviscid liquid during

expulsion from the quartz tube, i.e. Bernoulli's equation (equation (2.1)) is no longer descriptive of the flow of the melt as a function of expulsion pressure; the changes in melt density with increasing solute concentration are too small to account for the observed changes in flow characteristics. An equation of the form of Bernoulli's equation may, however, be used to describe the system provided that a "discharge coefficient" is incorporated into the formulation. This coefficient, which takes into account the energy losses in the nozzle, is probably alloy composition dependent. In order to determine the composition dependence of this coefficient a number of CBMS experiments must be performed for each alloy composition using different expulsion pressures, wheel speeds and/or orifice diameters; this was not attempted, but would be of considerable importance in any future work on this alloy system (Chapter 7). A discharge coefficient is not generally necessary for modelling the flow of molten metal from the nozzle during CBMS, but has been used previously for modelling the CBMS characteristics of dilute Al-Mn and Al-Fe alloys [18].

The equilibrium liquidus temperature for dilute Au-Ti alloys increases with increasing Ti concentration (fig. 2.9(a)). Thus, as all of the alloys were induction heated to the same temperature (1400°C) prior to expulsion from the quartz tube, the superheat of the melt decreased as a function of Ti concentration. This decrease in melt superheat with increasing Ti may be expected to result in the viscosity of the melt increasing with increasing solute concentration, leading to a composition dependence of the discharge coefficient. In addition, the melt is cooled on passing through the nozzle in the base of the quartz tube during CBMS; this occurs as the nozzle is not heated by induction during the melting of the alloy as it contains no metal. As the effective superheat of the melt decreases with increasing with increasing Ti concentration, the probability of the temperature of the melt falling below the liquidus temperature while in the nozzle increases with increasing solute concentration. At temperatures below the alloy liquidus temperature, nucleation may commence, resulting in a considerable increase in the viscosity of the melt and a consequent decrease of the flow rate from the nozzle (see e.g. [106]). The presence of active nuclei in the melt should result in a relatively equiaxed microstructure in the as-solidified alloys [106]; however, in practice the microstructures of the 2wt.% Ti and 3wt.% Ti alloy ribbons are decidedly columnar (fig. 4.16 and fig. 4.25), suggesting that very little nucleation occurs in the melt. The equilibrium Au-Ti phase diagram (fig. 2.9(a)) shows that for dilute alloys the freezing range is small; thus by cooling only a few degrees below the liquidus temperature the system reaches the solidus temperature, at which stage (assuming near-equilibrium in

maintained) the volume fraction of solid will increase considerably. Hence once the melt temperature falls below the liquidus temperature the melt viscosity will increase rapidly with decreasing melt temperature. This increase in viscosity will reduce the flow rate of the melt through the nozzle considerably, allowing more time for cooling and for nucleation to occur, i.e. once the melt temperature reaches the liquidus temperature the nozzle will probably block. However, should the melt temperature remain above the liquidus temperature while passing through the nozzle, melt spinning should proceed without incident; the difference between a successful and unsuccessful melt spinning experiment for dilute Au-Ti alloys is thus probably only a few degrees superheat. The small alloy freezing range associated with the dilute Au-Ti alloys implies that partial blockages (which would presumably have resulted in a ribbon with dimensions which were anomalous within the series of alloys studied) are unlikely. This explanation relies on there being little or no supercooling in the melt prior to nucleation commencing in the nozzle region; however, on striking the wheel surface the melt is reported to undercool up to several hundred degrees (see e.g. [11]). This difference between nucleation characteristics of the melt in the nozzle and on the wheel surface may be explained on the basis of the higher cooling rate experienced by the melt when in contact with the wheel surface.

The geometrical and visual uniformity of a melt spun ribbon is a reflection of the stability of the melt pool during solidification [20, 107]. Thus the 1wt.% Ti and 2wt.% Ti alloy ribbons formed from relatively stable melt pools, while no stable melt pool formed during melt spinning of the 5wt.% Ti alloy [107]. The 3wt.% Ti alloy formed short ribbons with a large variation in the average ribbon widths (0.35 ± 0.13 mm), suggesting that the melt pool for this alloy was only marginally stable during CBMS. The ribbons of this alloy are narrower than those of the 1wt.% Ti and 2wt.% Ti alloys. Thus, as the ribbon width corresponds approximately to the width of the melt pool (see e.g. [24]), the melt pool was narrowest for this alloy. In addition, the 3wt.% Ti ribbons are considerably thinner than those of the other alloys. Thus, assuming that the solid-liquid interface velocities for all of the alloys were similar, the time taken to solidify the entire thickness of the ribbon (or residence time in the melt puddle: equation (2.6)) was shortest for the 3wt.% Ti ribbons. The residence time is a reflection of the length of the melt pool and thus the melt pool was shorter for the 3wt.% Ti alloy than for the 1wt.% Ti and 2wt.% Ti alloys. The small dimensions of the pool would inhibit the ability of the pool to damp out fluctuations in the flow rate of the melt from the nozzle; these fluctuations would be manifested as variations in the dimensions of the CBMS ribbons.

In addition, the melt flow rate from the nozzle for the 3wt.% Ti alloy was very low (table 4.1) rendering both the melt stream and melt pool susceptible to capillary instabilities. These instabilities would also result in fluctuations in the ribbon dimensions (see e.g. [108]). A combination of these instabilities and the fluctuations in flow rate of the melt from the nozzle gave rise to the large variations in dimensions of the 3wt.% Ti ribbons.

The wetting patterns seen on the wheel-side surfaces of all of the ribbons (fig. 4.2(a) and fig. 4.3(a)) indicate that intimate contact was achieved between the wheel surface and melt during CBMS of the 1wt.% Ti, 2wt.% Ti and 3wt.% Ti alloys. Assuming a heat transfer coefficient (h) of 10^5 $Wm^{-2}K^{-1}$ (a value typical of other alloys which were melt spun in air [24, 36]) and a thermal conductivity (k_s) equal to that of pure Au for all of the alloys (309 $Wm^{-1}K^{-1}$ [109]), the Nusselt numbers ($N = hX/k_s$) for the 1wt.% Ti, 2wt.% Ti and 3wt.% Ti ribbons during CBMS are given in table 5.1. The values indicate that heat flow was Newtonian during rapid solidification of these alloys (i.e. $N \leq$ approximately 0.015). Under Newtonian heat flow conditions (from equation (2.4)) the average cooling rate during CBMS is proportional to the inverse of thickness of the ribbon (i.e. the cooling rate is proportional to $1/X_{ave}$); these values for the 1wt.%, 2wt.% and 3wt.% Ti alloys are given in table 5.1. From the table the highest cooling rate was experienced by the 3wt.% Ti alloy, while the 1wt.% Ti alloy cooled slowest.

Table 5.1 Heat flow characterisation of the as-solidified ribbons.

Alloy Composition	Ribbon Thickness (X_{ave})(μm)	Nusselt Number	$1/X_{ave}$ (μm^{-1})
Au-1wt.% Ti	24.5 ± 1.86	0.0080	0.0405
Au-2wt.% Ti	10.5 ± 1.56	0.0034	0.0952
Au-3wt.% Ti	9.51 ± 4.39	0.0038	0.105

The irregular geometry and small size of the 5wt.% Ti flakes indicate that they were the product of a highly unstable solidification process, i.e. there was no stable melt pool formed during CBMS of this alloy. Thus the residence time of the material on the wheel surface may have varied considerably; indeed the instability of the solidification process may have been such that the flakes may not have been completely solidified

prior to leaving the wheel surface. Thus the instability during the solidification process suggests that there was a large variation in cooling rate during the CBMS of the 5wt.% Ti flakes.

Dilute Au-Ti alloys were rapidly solidified in order to reduce microsegregation and suppress the nucleation of the equilibrium second phase during solidification. Both of these effects are considerably assisted by an increased cooling rate during rapid solidification. It is thus fortuitous that the 3wt.% Ti alloy (which had the largest driving force for the nucleation of Au_4Ti of the alloys which formed ribbons) was the alloy which experienced the highest average cooling rate during CBMS. Although the relative cooling rate of the small flakes of the 5wt.% Ti alloy produced by CBMS is not known, these materials allowed a provisional study of the as-solidified microstructure and the structural order present in this alloy.

5.2 THE AS-SOLIDIFIED ALLOY MICROSTRUCTURES

In this section the current understanding of the effect of rapid solidification on both microsegregation and macroscopic segregation is used to predict the likely features of the as-solidified microstructures of dilute Au-Ti alloys. The predictions concerning Au-Ti alloys are then compared to the observed as-solidified microstructures.

Rapid solidification reduces the amount of macroscopic segregation that occurs during solidification by increasing the partition coefficient at the solid-liquid interface (section 2.2.1(a)). This increase in the partition coefficient at the solidification front occurs as a result of the solid-liquid interface velocity approaching or (in order to achieve completely partitionless solidification) exceeding the diffusional velocity of the solute in the melt. Thus at high interface velocities the partition coefficient is a function of interface velocity. The amount of solute trapping that can occur may, however, be subject to a thermodynamic constraint: there must be a thermodynamic driving force for the formation of a solid with the same composition as the liquid for partitionless solidification to be possible (section 2.2.1(a)). The Au-Ti equilibrium phase diagram (fig. 2.9(a)) shows that for the 1wt.% Ti, 2wt.% Ti and 3wt.% Ti alloys the first phase to solidify on cooling the molten alloy is the $\alpha_{f.c.c.}$ solid solution; thus for these alloys there is no thermodynamic restriction on the amount of solute trapping possible. Compositional analyses on the 5wt.% Ti alloy showed that, after CBMS, the alloy contained 4.6wt.% Ti. Thus under equilibrium solidification conditions the first phase

to solidify from the liquid should be Au_2Ti at approximately 1220°C (fig. 2.9(a)). Further cooling results in the nucleation of Au_4Ti at 1172°C prior to the nucleation of the $\alpha_{f.c.c.}$ phase at 1123°C. However, no indication of the presence of Au_2Ti precipitates was seen in diffraction patterns from the CBMS 5wt.% Ti alloy and, although the as-solidified flakes of this alloy contain Au_4Ti precipitates, the distribution and size of the precipitates suggest that this phase nucleated within an already solidified $\alpha_{f.c.c.}$ grain. In addition, all of the Au_4Ti precipitates maintained the expected orientation relationship with the parent f.c.c. reflections, confirming that they nucleated within an f.c.c. grain rather than from the melt. Thus the Au_4Ti phase present in the CBMS 5wt.% Ti alloy occurs as a result of the cooling rate subsequent to solidification being insufficient to suppress the solid state nucleation of the Au_4Ti phase from the $\alpha_{f.c.c.}$ phase. As the alloy was apparently able to solidify as an f.c.c. solid solution on CBMS, there is no thermodynamic constraint on the amount of partitionless solidification possible in this alloy. However, solute trapping is only of importance at the very highest interface velocities and is unlikely to be a general effect in the microstructures produced by CBMS (see e.g. [28]).

The degree and scale of the microsegregation present in the as-solidified microstructures is determined by the stability of the solid-liquid interface during solidification (section 2.2.1). Of particular importance with respect to microsegregation during rapid solidification is the absolute interface velocity ($R_{abs} = \Delta T_0 D/k\Gamma$, equation (2.13)), which is the interface velocity at which no microsegregation of the solute can occur. R_{abs} is proportional to the alloy freezing range ($\Delta T_0 = mC_0(1-k)/k$, fig. 2.2(c)), and inversely proportional to k. For alloys containing up to 3.5wt.% Ti the Au-Ti equilibrium phase diagram (fig. 2.9(a)) shows that ΔT_0 is small and consequently k is close to unity. TEM examination of the 5wt.% Ti alloy showed that this alloy solidified as an f.c.c solid solution; thus the alloy freezing which should be considered when determining the solid-liquid interface stability during rapid solidification of this alloy is that given by the metastable extensions of the solidus and liquidus curves for the $\alpha_{f.c.c.}$ phase; these extensions are shown in fig. 5.1 [110]. The metastable extensions suggest that ΔT_0 remains relatively small up to a composition of 5wt.% Ti, and that consequently k is not strongly dependent upon composition for rapidly solidified alloys containing up to 5wt.% Ti. As a result, assuming that D and Γ are approximately constant over the composition range, the phase diagram suggests that R_{abs} is not strongly dependent upon alloy composition for the alloys examined here. Previously published studies on the effect of rapid solidification on alloy systems in which R_{abs}

exhibits a similar behaviour have shown that microsegregation-free microstructures may form over a wide range of compositions (see e.g. [64, 111, 112]). However, the evolution of latent heat during rapid solidification by CBMS may slow down the interface velocity as solidification proceeds, resulting in the solid-liquid interface velocity varying as a function of distance from the wheel surface (section 2.2.1(d)). Thus, although R_{abs} may initially be exceeded, the interface velocity may subsequently drop below this value, resulting in a variation in solute microsegregation through the ribbon thickness.

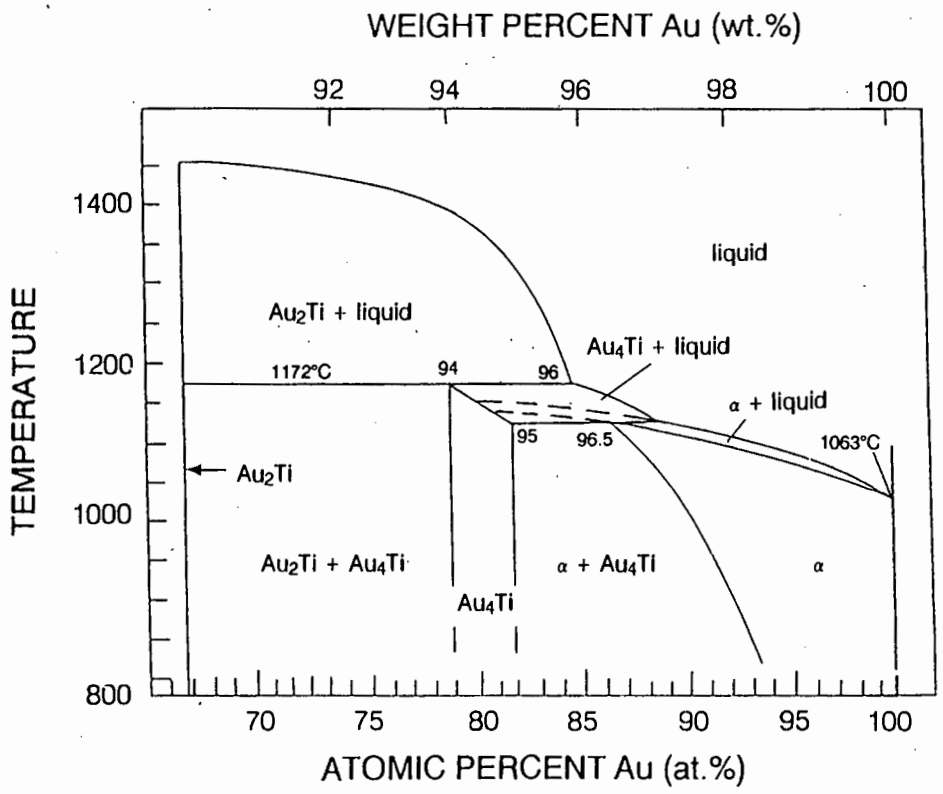

Fig. 5.1 Equilibrium binary phase diagram for the Au-Ti alloy system showing the metastable extensions (indicated by dashed lines) of the equilibrium solidus and liquidus curves of the $\alpha_{f.c.c.}$ phase.

The effects of the evolution of latent heat during the solidification of the 1wt.% Ti alloy are apparent as a variation in grain size and etching response across the ribbon section (fig. 4.7). Immediately adjacent to the wheel-side surface of the ribbon is a region which showed no response to etching. Examination of the wheel-side surface (fig. 4.4(a)) revealed that, although the grain size is small, it is not the very fine equiaxed microstructure often seen on the wheel-side of rapidly solidified ribbons (see e.g. [73,

113, 114]). The 1wt.% Ti alloy ribbons also exhibit a change in etching response at approximately 10 μm from the wheel-side surface, accompanied by a transition in the grain morphology from columnar to a more equiaxed grain morphology. No microsegregation of Ti was observed in bright-field TEM micrographs or electron diffraction patterns from either the columnar grained of equiaxed grained regions; although no analytical TEM facilities were available to confirm these observations, microsegregation of Ti does not appear to have occurred in this alloy. Interestingly, a tapered section showed that no change in grain size occurred at the interface between the columnar and equiaxed grains (fig. 4.8(b)). This continuity of the grain size across a tapered section of a 1wt.% Ti ribbon is reminiscent of the microstructures observed by Chu and Granger in melt spun Al-Fe alloys [73] and consideration must thus be given to the possibility that the solidification conditions giving rise to the microstructures of the 1wt.% Ti and Al-Fe alloys were related.

In Al-Fe alloys the transition in microstructure was shown to be the result of a change in the segregation of the solute as a function of distance from the wheel surface [73]. Chu and Granger proposed that the microstructure observed in Al-Fe alloys formed as a result of the dendrite tip radius (solidifying into an undercooled melt) increasing as a function of distance from the wheel surface due to the evolution of the latent heat of solidification (fig. 2.7(b)). In practice this coarsening of the dendrite tip translates to the cell spacing increasing as a function of distance from the wheel-side surface [73]. If there is no segregation in the "columnar grained" region adjacent to the wheel-side surface (as suggested by fig. 4.9(a)) the transition in microstructure seen at approximately 25% of the ribbon thickness may be the result of a transition from a thermal dendrite to a solutal dendrite, i.e. as a result of R decreasing from a value exceeding $(R_{abs})_c$ to a value less than $(R_{abs})_c$ (fig. 2.7(a)). However, as there is no evidence of a clearly defined dendrite structure in this region, this seems rather improbable. If there was some segregation in the "columnar grained" region, the transition could be from very fine to coarse cellular structures (as observed by Chu and Granger [73]). Both of these explanations would account for the continuous increase in the scale of the microstructure across the section (seen in the tapered section in fig. 4.8(a)) and the observed discrete change in etching response. However, although these observations are consistent with the microstructure observed in the tapered section, they do not correlate with the microstructure seen in the etched cross-section of the ribbon. Examination of a cross-section of a 1wt.% Ti ribbon (fig. 4.7(b)) reveals that the equiaxed grains coarsen with increasing distance from the wheel-side surface, and

there is some evidence of coarsening of the columnar grains. However, there is no evidence of the rather rapid transitions in grain size across the section seen by Chu and Granger in Al-Fe alloys. In addition, Chu and Granger's sections appeared "equiaxed" through the entire ribbon cross-section, and showed no evidence of the columnar grained region seen here. Thus, although there is insufficient evidence to dismiss this explanation of the microstructure observed in the 1wt.% Ti alloy, the theory does not satisfactorily explain the observed microstructures.

The transitions in microstructure seen in the etched cross-section of a 1wt.% Ti alloy ribbon (fig. 4.7) are similar to those observed in conventional castings and ingots with a region of fine equiaxed grains (or a chill zone) adjacent to the chill surface, a zone of columnar grains, and a region of equiaxed grains (see e.g. [115]). In castings, however, the transition from columnar to equiaxed grains occurs as nucleation takes place ahead of the advancing interface, resulting in a blockage of the advance of the columnar grains by the free crystals by means of mechanical, thermal or solutal field effects (see e.g. [115, 116]). As the nucleation and growth of the equiaxed grains occurs independently of that of the columnar grains, no continuity of the grain size is necessarily expected across the columnar grains/equiaxed grains interface. The apparent continuity of the grain size (in a plane approximately parallel to the ribbon surfaces) through the thickness of the 1wt.% Ti alloy ribbon therefore suggests that the nucleation and growth of the equiaxed grains was intimately linked to that of the solid-liquid interface. This type of nucleation has been seen previously in melt spun alloys and may be indicative of a situation in which the growth rate of the interface is low, allowing nucleation at, or slightly ahead of, the advancing interface [66]. The evolution of latent heat during solidification of the alloy thus slowed down the solid-liquid interface in this alloy sufficiently to allow nucleation to occur at the interface during solidification.

In a tapered section of a 2wt.% Ti alloy ribbon the region immediately adjacent to the wheel-side surface shows a limited response to etching (fig. 4.17), while the rest of the cross-section is made up of columnar grains extending through the thickness of the ribbon (fig. 4.16). In the 3wt.% Ti alloy, however, the entire ribbon cross-section consists of columnar grains extending through the ribbon thickness with no evidence of a variation in etching response across the section (fig. 4.25). The variation in etching response of the columnar grains is reminiscent of that seen by Cantor *et al.* in CBMS microstructures of Ni-Al and 316L stainless steel alloys [28]. In these alloys the transition was shown to be linked to a breakdown of the solidification interface from a

planar front to a cellular microstructure. Unfortunately, the quality of the 2wt.% Ti ribbons prohibited the preparation of TEM foils from this region by electropolishing, preventing a more detailed examination of this region. Nevertheless, the presence of these regions suggests that R_{abs} may only have been exceeded in a very small region of the ribbon cross-section and that, contrary to expectation, R_{abs} in dilute Au-Ti alloys may exhibit a sensitive dependence on Ti concentration. The most likely explanation of this discrepancy lies in the possibility that in practice ΔT_0 for dilute Au-Ti alloys may be larger than shown in (fig. 2.9(a)). Examination of the original data on which the equilibrium phase diagram is based shows that for alloys containing less than 3.5wt.% Ti the solidus and liquidus curves shown in fig. 2.9(a) are based on data from only two alloys [117]. These curves are thus subject to considerable uncertainty and hence ΔT_0 may be larger than is generally assumed to be the case.

The considerable variation in thickness and the presence of a large number of holes through the as-solidified ribbons of the 2wt.% Ti and 3wt.% Ti alloys prevented electropolished TEM specimens being prepared from these alloys for study of the segregation of Ti as a function of distance from the wheel-side surface. However, these ribbons were found to contain electron transparent regions directly on solidification. Although undoubtedly related, the microstructures of the "as-solidified" electron transparent areas are not necessarily representative of the "bulk" ribbon microstructures. The electron transparent regions in the as-solidified 2wt.% Ti and 3wt.% Ti alloys exhibited fine grained microstructures with no evidence of segregation of Ti to the grain boundaries and no evidence of nucleation of Au_4Ti. A study of the 1wt.% Ti, 2wt.% Ti and 3wt.% Ti alloys by Aboud in which x-ray diffraction patterns from the ribbons were analysed using Rietveld analysis confirmed that little segregation or second phase formation occurred during solidification [118]. Thus, although some segregation of Ti may have been present, rapid solidification largely suppressed the segregation of Ti and the nucleation of Au_4Ti during solidification, producing highly supersaturated solid solutions.

From the above discussion it is apparent that the 1wt.% Ti alloy ribbons show the largest effect of the evolution of latent heat of solidification in their microstructure. The major influence on the formation of observed microstructure was undoubtedly the cooling rate during solidification, and the evolution of the latent heat of solidification at the solid-liquid interface. The 1wt.% Ti alloy ribbons are considerably thicker than any of the other ribbons examined (table 4.1) and hence if solidification occurred under

Newtonian heat flow conditions (and assuming all other variables in equation (2.4(a)) are insensitive to alloy composition) the cooling rate was lower for the 1wt.% Ti alloy than either the 2wt.% Ti or 3wt.% Ti alloys (table 5.1). However, although overall heat flow during rapid solidification processing was Newtonian, the mode of heat flow during the solidification of the ribbon may have been ideal (section 2.1.1) in which case the cooling rate was inversely proportional to the square of the distance from the wheel surface (equation (2.5(a))). Under ideal heat flow conditions the cooling rate is thus high adjacent to the wheel surface, but decreases rapidly across the ribbon thickness. Assuming all other variables in equation (2.5(a)) to be independent of composition, the greater thickness of the 1wt.% Ti ribbon would result in a much lower cooling rate in the region adjacent to the free surface than in the 2wt.% Ti or 3wt.% Ti ribbons.

The cross-sectional microstructure of the rapidly solidified 5wt.% Ti alloy flakes varies considerably: in some of the flakes the microstructure consists of columnar grains extending from the wheel-side to the free-side of the flake, while in others the entire microstructure is made up of equiaxed grains (fig. 4.32). The variations in microstructure are probably in part the result of the variety of cooling rates associated with the variations in flake thicknesses. In addition, the highly unstable solidification process which give rise to the formation of these flakes of material suggests that the residence time of some of the flakes on the wheel surface may not have been sufficient to allow solidification of the entire ribbon thickness prior to the material leaving the wheel surface. On leaving the wheel surface the cooling rate will decrease substantially and thus this latter effect implies that, although the flakes of 5wt.% Ti alloy were considerably thinner that the CBMS ribbons formed by the other alloys, the cooling rate during rapid solidification was not necessarily higher for the 5wt.% Ti than for the other materials examined. Nevertheless, the apparent lack of nucleation of the long-range-ordered Au_4Ti phase during solidification, the presence of special-point order in the as-solidified alloys, and the columnar grained structure observed in a number of the flakes suggest that a high cooling rate was indeed achieved during solidification of at least some of the flakes of the 5wt.% Ti alloy. The nature of the product, and the very limited "as-solidified" thin area available, curtailed the study of this alloy considerably.

From the above discussion it is apparent that, although the amount of segregation present in the as-solidified alloys could not be accurately determined, rapid solidification of the 1wt.% Ti, 2wt.% Ti and 3wt.% Ti alloys suppressed the nucleation of Au_4Ti and resulted in the formation of highly supersaturated alloys. In the 5wt.% Ti

alloy the Au_4Ti phase nucleated during rapid solidification; however, the presence of special-point order in this alloy suggests that some of the Ti present was bound up in structures other than (D1a) Au_4Ti precipitates.

5.3 MICROSTRUCTURAL AND PROPERTY EVOLUTION ON POST-SOLIDIFICATION HEAT TREATMENT.

Post-solidification heat treatment of the supersaturated alloys produced by rapid solidification should result in precipitation of the (D1a) Au_4Ti phase with a commensurate improvement in the mechanical properties of the alloy. However, in practice the mechanical properties of the as-solidified alloys show widely varying responses to heat treatment: the microhardness of the 1wt.% Ti alloy decreases on post-solidification heat treatment while the microhardness of the 2wt% and 3wt.% Ti alloys increases.

The decrease in microhardness of the 1wt.% Ti alloy on heat treatment is associated with an increase in the average grain size in this alloy as a result of heat treatment. In addition, heat treatment did not result in second phase precipitation in this alloy. Chemical analysis of the 1wt.% Ti alloy after CBMS showed that the alloy contained only 0.65wt.% Ti, i.e. a considerable amount of Ti was lost during processing. From the equilibrium Au-Ti phase diagram (fig. 2.9(a)) the solubility of Ti in the $\alpha_{f.c.c.}$ terminal phase is 0.25wt.% Ti at 350°C and increases to 0.62wt.% Ti at 500°C. Thus only approximately half of the 0.65wt.% Ti present in this alloy is available for second phase formation at 350°C and virtually none at 500°C. In addition, some segregation of Ti to the grain boundaries may have occurred during rapid solidification, further reducing the amount of Ti present in solid solution in this alloy.

The grain size becomes more uniform across the 1wt.% Ti ribbons on heat treatment (fig. 4.11 and fig. 4.13). The driving force for the observed grain growth was the reduction of surface energy associated with the grain boundaries. However, there is a noticeable change in the columnar grain growth as a function of alloy heat treatment (fig. 4.11); the columnar grains coarsen on heat treatment at 350°C for 1 h but begin to break down on heat treatment at 400°C for 1 h. After 1 h at 500°C the columnar structure is no longer discernible and the equiaxed grains are the same size and shape distribution as throughout the ribbon. Annealing for 24 h at temperatures above 350°C results in a more drastic break down of the columnar grained structure; whilst some

alloy the Au_4Ti phase nucleated during rapid solidification; however, the presence of special-point order in this alloy suggests that some of the Ti present was bound up in structures other than (D1a) Au_4Ti precipitates.

5.3 MICROSTRUCTURAL AND PROPERTY EVOLUTION ON POST-SOLIDIFICATION HEAT TREATMENT.

Post-solidification heat treatment of the supersaturated alloys produced by rapid solidification should result in precipitation of the (D1a) Au_4Ti phase with a commensurate improvement in the mechanical properties of the alloy. However, in practice the mechanical properties of the as-solidified alloys show widely varying responses to heat treatment: the microhardness of the 1wt.% Ti alloy decreases on post-solidification heat treatment while the microhardness of the 2wt% and 3wt.% Ti alloys increases.

The decrease in microhardness of the 1wt.% Ti alloy on heat treatment is associated with an increase in the average grain size in this alloy as a result of heat treatment. In addition, heat treatment did not result in second phase precipitation in this alloy. Chemical analysis of the 1wt.% Ti alloy after CBMS showed that the alloy contained only 0.65wt.% Ti, i.e. a considerable amount of Ti was lost during processing. From the equilibrium Au-Ti phase diagram (fig. 2.9(a)) the solubility of Ti in the $\alpha_{f.c.c.}$ terminal phase is 0.25wt.% Ti at 350°C and increases to 0.62wt.% Ti at 500°C. Thus only approximately half of the 0.65wt.% Ti present in this alloy is available for second phase formation at 350°C and virtually none at 500°C. In addition, some segregation of Ti may have occurred during rapid solidification, further reducing the amount of Ti present in solid solution in this alloy.

The grain size becomes more uniform across the 1wt.% Ti ribbons on heat treatment (fig. 4.11 and fig. 4.13). The driving force for the observed grain growth was the reduction of surface energy associated with the grain boundaries. However, there is a noticeable change in the columnar grain growth as a function of alloy heat treatment (fig. 4.11); the columnar grains coarsen on heat treatment at 350°C for 1 h but begin to break down on heat treatment at 400°C for 1 h. After 1 h at 500°C the columnar structure is no longer discernible and the equiaxed grains are the same size and shape distribution as throughout the ribbon. Annealing for 24 h at temperatures above 350°C results in a more drastic break down of the columnar grained structure; whilst some

vestiges of their presence may be inferred from a ribbon heat treated at 400°C for 24 h, all evidence is absent after 24 h at 500°C.

The gradual breakdown of the columnar grain structure during heat treatment appears to arise from an initial coarsening of the column width followed by a gradual incorporation of boundaries across the width of the column. The driving force for initial column coarsening is the decrease in grain boundary area resulting from such a process. However, the subsequent appearance of boundaries which serve to increase the total boundary area is less easy to rationalise. The variable through-thickness dislocation densities may play a role in this process; dislocations are known to be produced by rapid solidification under suitable circumstances [11, 119]; it is probable that the wheel-side of the ribbon undergoes a greater amount of process-induced deformation than the remainder of the ribbon as it is the first region to solidify and is subsequently forcibly stripped from the wheel surface. TEM micrographs of the as-solidified microstructure taken from the region judged as corresponding to a position within the columnar grain structure (fig. 4.9(a) and fig. 5.2) show that there is a significant dislocation population which exceeds that observed from regions more distant from the heat-sink surface (fig. 4.9(b)). A detailed analysis of the dislocation density as a function of position was not attempted, but, given that a higher dislocation density is seen to exist in the columnar grained region of the ribbon, recovery processes with accretion of dislocations into cell walls would then provide the driving force for an apparent increase in the boundary area during annealing. Once dislocation-free grain interiors are established in the previously columnar regions, the coarsening seen in fig. 4.11 would be expected to be dominated by a minimisation of the boundary area.

For the 2wt.% Ti and 3wt.% Ti alloys there is a considerable increase in microhardness on heat treatment at both 350°C and 500°C (fig. 4.6(b) and (c)). These figures suggest that the microhardness values of both the as-solidified and heat treated 2wt.% Ti ribbons are similar to those of the 3wt.% Ti ribbons; however, the 3wt.% Ti ribbons were considerably thinner than those of the 2wt.% Ti alloy and thus may not have been able to accommodate all of the strain associated with the indentation process. This would result in the indents being disproportionately large, and would thus account for the apparent softness of this alloy. Although the absolute microhardness values for the 3wt.% Ti alloy do not necessarily accurately reflect the mechanical properties of this alloy relative to the 1wt.% Ti and 2wt.% Ti alloys, they nevertheless give an indication of the kinetics of hardening of the alloy as a function of heat treatment.

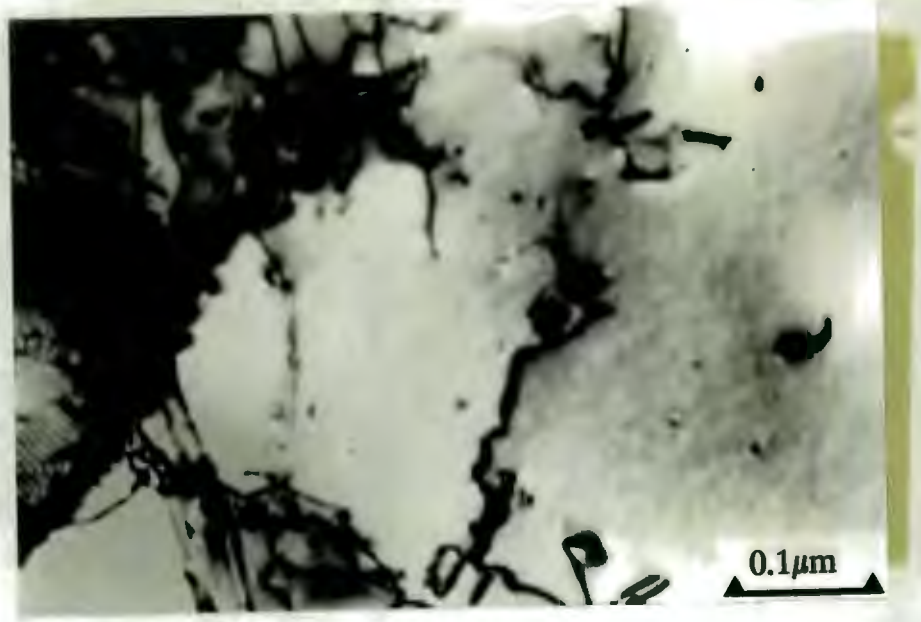

Fig. 5.2 Bright field TEM micrograph from the columnar grained region of an as-solidified 1wt.% Ti ribbon showing dislocations both in low-energy arrays and in isolated intergranular regions.

The 2wt.% Ti alloy exhibits an increase in microhardness on heat treatment at 350°C for 1 h (fig. 4.6(b)); longer times at this temperature result in the microhardness of the 2wt.% Ti ribbons increasing further. TEM examination of the 2wt.% Ti alloy ribbons after heat treatment reveals evidence of contrast in the lattice consistent with the strain associated with the presence of precipitates (fig. 4.21(a)). In addition, electron diffraction patterns exhibit superlattice reflections consistent with the presence of (D1a) Au_4Ti precipitates (fig. 4.21(b)). The intensity of these superlattice reflections is dependent upon the length of time the specimen had been held at 350°C. However, the (D1a) Au_4Ti precipitates could not be imaged by means of superlattice-centred dark-field imaging; this was a result of both the very low intensity of the superlattice reflections (the diffraction pattern shown in fig. 4.21(b) required an exposure time of 20 minutes) and the very small size of the Au_4Ti precipitates present.

The microhardness of the 3wt.% Ti alloy increases substantially on heat treatment at 350°C for 1 h; however, the microhardness of the 3wt.% Ti alloy does not change significantly on longer heat treatment times at this temperature (fig. 4.6(c)). Diffraction

patterns from the 3wt.% Ti alloy after 1 h at 350°C reveal superlattice reflections due to the presence of (D1a) Au_4Ti precipitates. However, for this alloy the intensities of the superlattice reflections relative to the parent f.c.c. reflections do not change between heat treatments of 1 h and 24 h at this temperature. This suggests that the amount of Au_4Ti formed after 1 h at 350°C does not increase substantially on longer heat treatment at this temperature. A possible explanation of this effect is that only a portion of the Ti in this alloy is mobile at 350°C (and hence able to form Au_4Ti precipitates), while the remainder is bound-up in structures which are stable at this temperature. As will be discussed in section 5.4, the state of order present in this alloy directly on quenching is particularly stable and thus, although the long-range ordered Au_4Ti phase nucleates at a temperature below 350°C, it is nevertheless possible that elements of the quenched-in state of order are retained at this temperature. Should this occur, on heat treatment at 350°C the mobile Ti would be rapidly consumed to form Au_4Ti precipitates, resulting in the observed increase in microhardness. Thereafter no more precipitates can form, and provided that the precipitates do not coarsen (which does not appear to have occurred), the microhardness will be unaltered by more extended heat treatments.

On heat treatment at 500°C for 1 h both the 2wt.% Ti and 3wt.% Ti alloys form Au_4Ti precipitates which are homogeneously distributed with no evidence of local variations in the precipitate density in the region of the grain boundaries (fig. 4.22 and fig. 4.30 respectively). The small difference between the lattice parameters of the Au_4Ti and the Au solid solution - a 2.3% contraction in the c-direction and a 0.16% expansion in the a- and b-directions occurs on the formation of the ordered phase* - is reflected in the spherical shape of the precipitates and their coherency with the matrix. On heat treatment at 500°C for 24 h the precipitates in the 2wt.% Ti alloy are seen to have coarsened (fig. 4.23) but they retain their spherical shape and there is still evidence of considerable coherency stains in the lattice. The precipitates for the 3wt.% Ti alloy, however, have undergone a change in morphology from approximately spherical to non-crystallographic elongated shapes with a suggested loss of coherency evidenced by a reduction of strain contrast in the bright field image from this alloy (fig. 4.31(a) and (b)). The loss of coherency is apparently accompanied by the predominance of a single orientational variant of superlattice structure, reflecting the preferred growth of one

* The calculation of the dilation and contraction of the lattice is based on $a' = (5/2)^{1/2}(a_{f.c.c.})$ and $c' = c_{f.c.c.}$ [120]. $a_{f.c.c.} = 4.078$Å, $a'_{Au4Ti} = 6.458$Å and $c'_{Au4Ti} = 3.983$Å [79]. The definitions of a', c' and a are given in fig. 2.9(b).

orientational variant to the detriment of others (fig. 4.31(c) and (d)). Examination of superlattice-centred dark-field micrographs taken using reflections from a number of different orientational variants of the precipitates after heat treatment at 500°C for 1 h suggests that the precipitates may contain more than one orientational variant of the D1a structure. Thus the predominance of a single orientational variant of the structure on extended heat treatment is not merely a result of the coarsening of the precipitates, but may also imply the annealing out of domain interfaces. Ruel *et al.* [82] showed that there are three types of domain interfaces in D1a structures, namely (in order of increasing surface energy): antiphase boundaries (APB), antiparallel twin boundaries (APTB) and perpendicular twin boundaries (PTB). Based on the work of Chakravarti *et al.* [121], Vasudevan *et al.* [122] showed that the coarsening of the domains in Ni_4Mo occurs predominantly as a means of eliminating the interfacial energy associated with the APB; it is probable that a similar driving force underlies the elimination of orientational variants of the Au_4Ti phase. Interestingly, the predominance of a single orientational variant in Ni_4Mo is generally associated with a large precipitate growing at a grain boundary [122], rather than the isolated precipitates seen for the 3wt.% Ti alloy.

Although the microstructures observed in the "as-solidified" electron transparent regions are not necessarily representative of the microstructures of the bulk, the changes in size and shape of the precipitates observed in the dark-field images show a good correlation with the observed changes in microhardness: the fine precipitate distributions seen in the 2wt.% Ti and 3wt.% Ti alloys after heat treatment at 500°C for 1 h may be expected to result in an increased microhardness, and the large increase in precipitate size after 24 h at this heat treatment is consistent with the deterioration in microhardness. Indeed even the shapes of the precipitates seen in the dark field images are similar to those seen by Graham in 1wt.% Ti bulk alloys [2, 3]. In addition, the relative intensities of the superlattice reflections and f.c.c. reflections in the 3wt.% Ti alloy on heat treatment at 350°C offer a plausible explanation of the stability of the microhardness at this temperature.

The DSC traces shown in fig. 4.5 exhibit evidence of a transformation commencing at approximately 480°C. However, on examining ribbons heat treated at this temperature no evidence was found of any transformations occurring at this temperature. It is probable that the peak observed was due to the oxidation of the specimen in the DSC cell; the oxidation would not have been observed in the heat treated alloys as the heat

treatments were carried out under a high vacuum as opposed to the relatively unclean dynamic Ar atmosphere maintained in the DSC cell. This is consistent with the observation made by Graham [3] that Au-Ti alloys are susceptible to oxidation above 400°C. This explanation also accounts for this peak being larger and more distinct for the 3wt.% Ti alloy than for the 2wt.% Ti alloy. The oxidation of the specimen was probably the cause of the slight "endothermic" peak seen for both the 2wt.% Ti and 3wt.% Ti alloys on reheating (fig. 4.5(b) and (c)). Confirmation of the oxidation of the sample in this temperature range requires the use of a surface analytical technique such as secondary ion mass spectrometry (SIMS) or Auger electron spectroscopy, neither of which were available.

The DSC traces for the 2wt.% Ti and 3wt.% Ti alloy ribbons (fig. 4.5(b) and (c)) show that a transformation commenced at approximately 320°C. This transformation was undoubtedly the precipitation of the Au_4Ti phase seen on heat treatment at 350°C. No evidence of transformations in the 2wt.% Ti and 3wt.% Ti alloys is seen in the DSC traces at temperatures below 320°C as is consistent with the observed stability of the state of order present in these alloys directly on solidification. The implications of the thermal stability of this quenched-in state of order, and the real-space interpretation of the diffuse scattering observed, will be discussed in the next section.

5.4 SPECIAL-POINT ORDER IN Au-Ti ALLOYS

The driving force for the formation of ordered phases in the Au-Ti system is known to be high [123]. It is thus not surprising that the long-range-ordered (D1a) phase in Au-Ti alloys is stable up to the melting point of the material [79]. However, rapid solidification of alloys with concentrations as high as 5wt.% Ti is apparently able to disrupt the formation of long-range order and introduce elements of $<1\frac{1}{2}0>$ special-point order. The presence of diffuse intensity maxima in electron diffraction patterns resulting from $<1\frac{1}{2}0>$ special-point order suggests that the high cooling rates associated with the rapid solidification process suppress the nucleation of the long-range-ordered (D1a) phase, producing instead a random f.c.c. solid solution. Provided that the cooling rate is high enough to prevent nucleation of the long-range-ordered (D1a) phase, concentration waves due to the $<1\frac{1}{2}0>$ special-point order will form at high temperatures and will be amplified on cooling through the ordering spinodal [89]. The diffracted intensity, which is a function of the amplitudes of these concentration waves, will thus be enhanced. In Au-5wt.% Ti significant nucleation of long-range

order occurred during the solidification process, with only traces of the $<1^1/_20>$ special-point order persisting to room temperature (fig. 4.34(a)). Increased cooling rates are likely to suppress, at least partially, the nucleation of the D1a phase, and thus enhance the degree of special-point order.

In Au-2wt.% Ti and Au-3wt.% Ti no detectable nucleation of the (D1a) long-range-ordered equilibrium phase occurred during the solidification process. Nevertheless, diffraction patterns from Au-3wt.% Ti (figs. 4.34(c) and 4.35(a)) suggest that elements of the long-range-ordered structure may be present in the as-solidified structure. As-solidified Au-3wt.% Ti shows considerably more scattering at the long-range order (D1a) positions than was discernible from electron diffraction patterns from previously studied as-solidified alloys showing special-point order; notably Au-Cr, Au-V and indeed Ni-Mo (e.g. compare the diffraction pattern shown in fig. 4.34(c) to those shown in fig. 1 of Van Tendeloo *et al.* [92]). As a first approximation, the presence of diffuse scattering at the D1a positions in fig. 4.34(c) suggests the existence of imperfectly ordered, discrete microdomains of D1a structure, possibly in the form of platelets parallel to the $\{420\}_{f.c.c.}$ planes, as has been previously suggested by Okamoto and Thomas [81]. However, as may be seen in fig. 4.35(a), the streaking extends unidirectionally from the D1a reciprocal lattice positions to the $1^1/_20$ positions, with no corresponding streaking in the opposite direction, as would be expected for in-plane streaking due to precipitate shape.

A description of the state of order which incorporates elements of both the D1a and DO_{22} structures, as suggested by Van Tendeloo *et al.* [92], would appear to be appropriate. The incorporation of elements of the DO_{22} structure is vindicated by the presence of the 110 reflections shown in fig. 4.38(a), as these reflections cannot arise from any other source [92, 93]. The incorporation of this structure in the real space description of special-point order in other alloy systems, where no evidence of these reflections was detected, was perhaps not always justified. Van Tendeloo *et al.* [92] have suggested that the "wings" seen in fig. 4.35(a) show evidence of a transfer of intensity from the $1^1/_20$ positions to the D1a positions. As both of these reciprocal lattice positions occur along a <210> direction in reciprocal space fig. 4.35(b) the intensity transfer between these reflections corresponds to a variation in the length of the diffraction vector without a change in its direction. In real space this implies that a variation in lattice spacing from that corresponding to the $1^1/_20$ reflections to that responsible for D1a reflections is present. Variation of the lattice spacing may be

achieved by introducing slabs of D1a structure between the {110} planes of the DO_{22} structure [92] - depending on the proportion of D1a and DO_{22}, the average lattice constant will vary and hence the position of the intensity maxima will shift from the $1^1/_20$ to the long-range order position. In-plane streaking is expected from the slabs of D1a structure. Unfortunately, no imaging evidence could be obtained to support this hypothesis, since the diffuse scattering was too weak to allow dark-field imaging.

Streaking was also evident between the $1^1/_20$ reflections and the fundamental f.c.c. reflections in Au-3wt.% Ti, as illustrated in fig. 4.37. This streaking is reminiscent of that seen previously by de Ridder *et al.* [87] in quenched alloys of composition Au_4V. However, their suggested three-dimensional spatial distribution for the diffuse streaking differs from that shown in fig. 4.37. De Ridder *et al.* have suggested that the diffuse streaking in Au_4V extends along cylindrical surfaces parallel to the cube directions and intersects the cube faces of the reciprocal lattice along pseudo-circles. They presented [001] and [112] zone-axis diffraction patterns in support of their suggestion. However, the visibility of the streaking seen in Au-3wt.% Ti was critically dependent upon the specimen thickness (compare fig. 4.35(a) and fig. 4.36). This has been shown also to be the case in Au_4V by Stobbs and Stobbs [93], although they did not elaborate on the three-dimensional spatial distribution of the streaking. Thus, as no thickness information was given by de Ridder *et al*, it is not possible to ascertain whether or not the streaking from Au_4V conformed to our suggested spatial distribution. However, the triangular shaped diffuse scattering seen in fig. 4.34(c) is not apparent in their diffraction patterns (e.g. compare fig. 4.34(c) to the diffraction patterns shown in fig. 12(a) of de Ridder *et al.* [87]), and hence the state of order in Au_4V appears to differ from that present in the Au-3wt.% Ti examined here. Thus, if the streaking seen was, as suggested by de Ridder *et al.*, due to the formation of particular cluster configurations, or, as seems more likely, due to the long-range interaction between the different local elements of order as suggested by Stobbs and Stobbs, the streaking would be expected to be different in Au-3wt.% Ti when compared with Au_4V. A more detailed study of the thickness dependence of diffuse streaking in Au_4V is required in order to clarify these issues. Nevertheless, the streaking was superficially similar in both Au_4V and Au-3wt.% Ti and thus may not be unique to a specific alloy as was originally suggested [93].

The 110 reflections (fig. 4.38(a)), attributed to the orientational variant of the DO_{22} structure which has its c-axis perpendicular to the zone-axis, are of some interest in that

there are no long-range order reflections in their immediate vicinity, as may be seen from fig. 2.11(b), and hence the reflections are expected to be spherical. The presence of 110 reflections is direct evidence that the DO_{22} type structure is indeed present [92, 93]. The presence of this structure in as-solidified Au-2wt.% Ti (composition $Au_{12}Ti$) and Au-3wt.% Ti (composition Au_8Ti) is somewhat surprising, as a stoichiometric DO_{22} phase would have the composition Au_3Ti. Unlike the reflections observed by Van Tendeloo *et al.* [92], the 110 reflections seen in the Au-3wt.% Ti studied here were found to occur not only in slightly aged alloys but also in alloys in the as-solidified state.

Annealing of special-point alloys at low temperatures generally results in enhanced diffuse scattering at the $1^1/_20$ positions due to the amplification of the amplitudes of the concentration waves (as suggested by de Fontaine [89] and Van Tendeloo *et al.* [92]), or by the annealing out of defects in the DO_{22} structure [81]. The thermal stability of Au-3wt.% Ti and Au-2wt.% Ti relative to other special-point alloys (see e.g. [81, 86, 87, 105]) must be attributed to the immobility of Ti in the lattice. However, the diffusivity of Ti in Au is known to be high [124, 125], and would be expected increase due to the high defect concentrations known to be associated with the rapid solidification process (see e.g. [126]). It is thus probable that the stability of the order present in as-solidified material is the result of the Ti being held in structures where it is stable. Stoichiometric DO_{22} has the composition Au_3Ti and the presence of this structure would consume significant amounts of the Ti in Au-3wt.% Ti and Au-2wt.% Ti, leaving little of the Ti in the remaining disordered regions. As a result, the enhancement of diffuse intensity maxima due to the formation of additional DO_{22} is unlikely. The order present in as-solidified Au-3wt.% Ti and Au-2wt.% Ti is apparently stable until nucleation of the equilibrium D1a phase occurs between 300°C and 360°C.

5.5 GENERAL DISCUSSION

In the introduction to this thesis it was suggested that rapid solidification may result in enhanced alloy mechanical properties. Although not the major thrust of the work presented here, it is nevertheless of some interest to attempt to assess the effect of rapid solidification on the properties by comparing the maximum microhardness values obtained on heat treating the rapidly solidified alloys with those reported in the literature for bulk alloys. No comparable Knoop microhardness values were found for bulk dilute Au-Ti values and the dimensions of the ribbons prevented the Vickers microhardness numbers of the ribbons being determined. However the Knoop and

Vickers microhardness values are known to be similar over a wide range of hardnesses, as a first approximation the values can be compared directly [127]; this is demonstrated by comparing the Vickers microhardness number of pure annealed Au (HV 40 [128]) with the Knoop microhardness value of this material (40.25kg/mm^2 (section 4.3)). Graham [3] obtained a maximum Vickers microhardness of approximately HV 180 in a 1.4wt.% Ti alloy bulk specimen while the 1wt.% Ti is claimed to have a maximum hardness number of between HV 180 and HV 170 [1]. The rapidly solidified 1wt.% Ti alloy (which, on analysis, was shown to contain 0.65wt.% Ti) softened on heat treatment; the maximum hardness of this alloy was thus in the as-solidified condition where the measured Knoop microhardness was 87.39kg/mm^2. In addition, as discussed in section 5.3, the absolute microhardness values obtained for the 3wt.% Ti alloy are not a reflection of the mechanical properties of this alloy relative to the other melt spun alloys, and thus the maximum hardness achieved in this alloy (225kg/mm^2) should not be compared directly to that of the commercial alloys. The largest measured microhardness of the rapidly solidified 2wt.% Ti alloy after post-solidification heat treatment was 253.15kg/mm^2; this value compares favourably with the HV 180 achieved by the 1.4wt.% Ti bulk alloy. Unfortunately, what contribution rapid solidification makes to this mechanical property enhancement is not known as no bulk alloy of composition 2wt.% Ti has been examined previously. Nevertheless, the results suggest that there is considerable microhardness enhancement associated with the higher alloy compositions studied here and thus indicate that additional research with the view to producing commercial Au-Ti alloys with higher Ti contents than those presently available may be of some interest.

The preceding sections illustrate that there are a number of unresolved issues relating to the route by which the state of order present in the as-solidified alloys transforms on heat treatment to the equlibrium long-range-ordered structure. The DSC traces for both the 2wt.% Ti and 3wt.% Ti alloys suggest that the nucleation of Au_4Ti commences at approximately 320°C, although the high heating rate used for obtaining these traces adversely influences the accuracy of the absolute value of this temperature. The (D1a) Au_4Ti phase has nucleated in both of these alloys by 350°C, and no transformations are observed at temperatures below 300°C. A series of heat treatments in this temperature range showed that Au_4Ti had nucleated by 340°C, but that at 330°C the alloy still retained the state of order present directly after solidification. A [112] zone axis diffraction pattern from a 3wt.% Ti alloy ribbon after 1 h at 335°C, shown in fig. 5.3, exhibits, in addition to the diffuse intensity associated with the quenched-in structure,

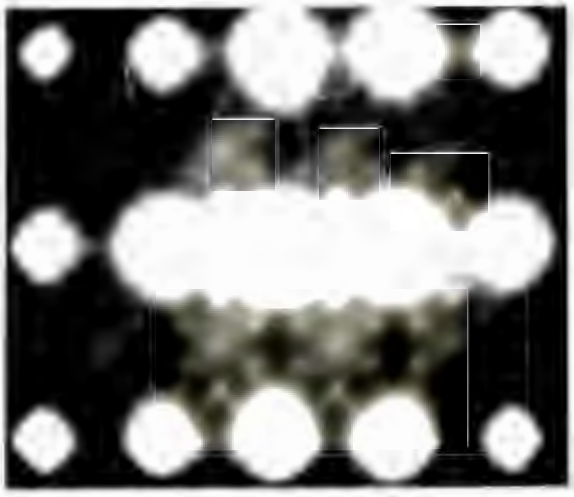

Fig. 5.3 [112] zone-axis electron diffraction pattern from the 3wt.% Ti alloy after heat treatment at 335°C for 1 h. The additional reflections arrowed in the figure are apparently associated with the transformation from the as-solidified structural order (fig. 4.35) to the long-range-ordered D1a structure (fig. 4.24).

reflections at positions not previously seen in as-solidified Au-Ti alloys, or indeed in the transformation from special-point-ordered to long-range-ordered D1a structures in other members of the special-point order family of alloys. A shortage of material and time prevented this aspect of the work being investigated further; however, the diffraction pattern suggests that the transformation route in Au-Ti alloys from the state of order present directly on solidification to the long-range-ordered state is a fruitful area for future research.

-ooOoo-

CHAPTER 6

CONCLUSIONS

(1) The flow characteristics of molten dilute Au-Ti alloys deteriorate with increasing Ti content. This results in the processing conditions necessary for forming high quality ribbons during CBMS changing considerably with Ti content.

(2) The microstructures of the as-solidified alloys are critically dependent upon the solidification conditions prevalent during rapid solidification (and hence upon the thicknesses of the ribbons formed during CBMS) and upon solute content. Thus, as the thicknesses of the ribbons examined here are dependent upon the Ti content of the alloy, the dependence of the ribbon microstructure on solute concentration cannot be unambiguously ascertained.

(3) CBMS of dilute Au-Ti alloys suppresses the nucleation of the long-range-ordered (D1a) Au_4Ti phase during the solidification of alloys containing up to 3wt.% Ti.

(4) Rapidly solidified 2wt.% Ti, 3wt.% Ti and 5wt.% Ti alloys contain elements of $<1^1/_20>$ special-point order directly after solidification, although the precise state of order varies with composition.

(5) Diffraction patterns from as-solidified 2wt.% Ti and 3wt.% Ti alloys suggest that there exists in these alloys an intermediate state of order which is best described by incorporating both elements of the (D1a) long-range ordered structure and elements of $<1^1/_20>$ special-point order. The 5wt.% Ti alloy contains D1a (Au_4Ti) precipitates directly on solidification.

(6) Streaking seen in the background of zone-axis diffraction patterns from a 3wt.% Ti alloy extends from the $1^1/_20$ reciprocal lattice positions to the parent f.c.c.

positions. The visibility of the diffuse streaking is dependent upon the foil thickness.

(7) The presence of diffuse reflections at 110 reciprocal lattice positions suggests that the incorporation of elements of both DO_{22} and D1a structures is appropriate in the description of the structural order giving rise to the special-point reflections observed directly upon solidification.

(8) The state of order present in the 3wt.% Ti alloy is stable up to a temperature of approximately 335°C, a temperature below the nucleation temperature of the equilibrium long-range ordered (D1a) Au_4Ti phase. The detailed transformation route from the state of order present directly on solidification to the equilibrium long-range-ordered state is, however, not known.

(9) The (D1a) Au_4Ti precipitates observed in the as-solidified 5wt.% Ti alloy nucleated from a supersaturated f.c.c solid solution, rather than from the solidifying liquid. This suggests that in principle there is no thermodynamic limit to the amount of solute trapping possible during the solidification of alloys containing up to 5wt.% Ti.

(10) A CBMS alloy of composition 0.65wt.% Ti (referred to as 1wt.% in the text) undergoes considerable grain growth with no discernible precipitation of Au_4Ti on heat treatment at temperatures in excess of 350°C. This grain growth results in a rapid deterioration of the microhardness of the alloy.

(11) Rapidly solidified 2wt.% Ti, 3wt.% Ti and 5wt.% Ti alloys exhibit considerable resistance to grain growth on heat treatment, with no change in grain size evident after 24 h at 500°C.

(12) Heat treatment of rapidly solidified 2wt.% Ti and 3wt.% Ti alloys at 350°C for 1 h results in a considerable increase in microhardness as a result of the nucleation of (D1a) Au_4Ti precipitates. The microhardness of the 3wt.% Ti alloy is unchanged by longer heat treatments at this temperature, while that of the 2wt.% Ti alloy continues to increase. It is suggested that this difference in response to heat treatment results from the stability of the remnants of quenched-in order in the 3wt.% Ti alloy at this temperature.

(13) On heat treatment at 500°C for 1 h the (D1a) Au_4Ti precipitates form in both 2wt.% Ti and 3wt.% Ti alloys. The precipitates are small, spherical, evenly distributed, and coherent with the matrix. Their presence is associated with a considerable increase in the alloy microhardness.

(14) On heat treatment at 500°C for 24 h the precipitates coarsen in both the 2wt.% Ti and 3wt.% Ti alloys, with a commensurate decrease in the alloy microhardness. The precipitates in the 2wt.% Ti alloy retain their spherical shape after this heat treatment; however, the precipitates in the 3wt.% Ti alloy become irregularly shaped. This change in shape is associated with the annealing out of orientational variants of the (D1a) phase.

-oo0oo-

CHAPTER 7

PROPOSED FUTURE WORK

The present work has shown that CBMS of dilute Au-Ti alloys has a number of complex microstructural and structural consequences, the detailed understanding of which would benefit from additional experimental work.

The alloys examined here were all CBMS using identical processing parameters. However, the processing parameters chosen produced high quality ribbons for only the 1wt.% Ti alloy, with the ribbon quality deteriorating with increasing Ti content (fig. 4.1). In addition, the thickness of the rapidly solidified ribbons decreased with increasing solute content, implying (see section 5.1) that the cooling rate experienced by the alloys during rapid solidification decreased with increasing solute content. Thus the as-solidified microstructures of the alloys examined here were influenced by variations in both solute concentration and cooling rate (during CBMS). In order to separate these effects it is necessary to manipulate the CBMS processing parameters so that the cooling rates during CBMS are very similar for all of the alloys examined. In principle, this requires that the cooling rate be determined as a function of processing parameters for each alloy composition prepared. However, for a particular alloy composition the cooling rate during rapid solidification is proportional to the inverse of the ribbon thickness (see e.g. [28]); thus, as a first approximation, it may be sufficient to compare the microstructures of CBMS ribbons with a variety of compositions but similar thicknesses. In addition, an indication of the effect of cooling rate on the alloy microstructure may be obtained by observing the changes in ribbon microstructure for a particular alloy composition as a function of ribbon thickness. Although both of these studies would be largely qualitative (CBMS does not lend itself readily to quantitative interpretation, see e.g. [40]), they might offer a more detailed insight into the effect of CBMS on alloy microstructure.

In order to produce ribbons of similar thicknesses, the effect of the various processing parameters on the ribbon dimensions would have to be ascertained. From such a study the discharge coefficient (see section 5.1 and [18]) as a function of alloy composition could be determined readily, thus giving a detailed insight into the physical processs underlying this parameter. In addition, the characterisation of the ribbon dimensions as a function of processing parameters for the various alloy compositions would allow these parameters to be manipulated so that high quality ribbons could be produced for all of the alloy compositions examined. The improved quality of the ribbons should facilitate the electropolishing of TEM specimens from the ribbons and hence allow TEM examination of the microstructures of the as-solidified and post-solidification heat treated alloys. Further, by preferentially electropolishing from one side of the ribbon, TEM examination of the grain size, dislocation density, structural order, precipitate density and size, and degree of segregation as a function of distance from the wheel surface for a variety of alloy compositions would be facilitated.

The microhardness values of the 2wt.% Ti alloys examined here appear to be appreciably larger than the values for so-called "bulk" alloys reported in the literature. However, the literature values were quoted for alloys containing less Ti than the materials examined here, and hence the proportion of the property enhancement resulting from rapid solidification, rather than the addition of more Ti, is not known. To systematically evaluate the contribution to property enhancement made by the rapid solidification of dilute Au-Ti alloys, alloys containing higher solute contents should be prepared and their microhardness values compared to those of rapidly solidified alloys with the same composition.

By examining alloys which have been CBMS under stable solidification conditions, the degree to which the nucleation of Au_4Ti can be suppressed by CBMS could be evaluated. For the 5wt.% Ti alloy examined here, the solidification conditions were highly unstable (resulting in the formation of flakes of material) and hence the cooling rate experienced by this alloy during CBMS is subject to considerable uncertainty. Consequently, the presence of Au_4Ti precipitates in the as-solidified 5wt.% Ti alloy does not necessarily preclude suppression of this phase in alloys with higher Ti contents. Should the nucleation of this phase be suppressed in higher Ti content alloys than was possible here, the likelihood of elements of special-point order being observed in these alloys would be enhanced and the characterisation of this state of order over a wide range of alloy compositions facilitated.

Special-point order has been identified previously in a number of alloy systems which, at equilibrium, contain a long-range-ordered phase with structure D1a (see section 2.3.2). However, examination of the equilibrium binary phase diagrams of the special-point order family of alloys (i.e. Au-V, Au-Mn, Au-Cr and Ni-Mo) reveals that the D1a structure is only stable to a temperature below the alloy melting point, i.e. at high temperatures all of these alloys form a disordered f.c.c. structure. The presence of special-point order in rapidly solidified Au-Ti alloys in which the Au_4Ti phase is stable (at equilibrium) up to its melting point is thus somewhat surprising, and suggests that the formation of special-point order may be possible in a number of other alloy systems; additional candidate Au alloy systems include Au-Hf and Au-Sc.

The special-point order present in Au-Ti alloys is associated with particularly well-defined reflections at the 110-type positions and thus clearly demonstrates the importance of the DO_{22} structure in the description of special-point order (see section 5.4). More extensive studies using high resolution TEM of the structural order present in these alloys directly on solidification would thus be of considerable interest. In addition, electron diffraction patterns from the as-solidified 3wt.% Ti alloy examined here exhibit diffuse streaking, the visibility of which is dependent upon the thickness of the specimen. The detailed characterisation of the visibility of the streaking as a function of foil thickness and the detailed underlying mechanisms for the formation of this streaking, require further investigation.

On the evidence of the additional reflections in the diffraction pattern shown in fig. 5.3, the transformation route in Au-Ti alloys from the state of order present in the as-solidified alloys to the formation of the equilibrium (D1a) long-range ordered Au_4Ti phase on post-solidification heat treatment differs somewhat from the transformation routes seen in other members of the special-point order family of alloys (see e.g. [81, 80, 105, 87]). The structures giving rise to these additional reflections and their significance in the transformation route are not known and require additional TEM characterisation.

-ooOoo-

REFERENCES

1.....G. GAFFNER, *Gold Bull.* **22**, 112 (1989).

2.....M. GRAHAM in *Proceedings of the 31st Annual EMSA Conference* (edited by C.J. Arceneaux), p. 148. Claitors, Baton Rouge (1973).

3.....M. GRAHAM, PhD Thesis, Northwestern University, Evanston , Illinois (1974).

4.....G. VAN TENDELOO, G. AMELINCKX AND D. DE FONTAINE, *Acta Crystallogr.* **B41**, 281 (1985)

5.....W. M. STOBBS AND S. H. STOBBS, *Phil. Mag. B* **53**, 537 (1986).

6.....H. JONES, *J. Mater. Scie.* **19**, 1043 (1984).

7.....H. JONES, *Rapid Solidification of Metals and Alloys*. Institution of Metallurgists, London (1982).

8.....T.R. ANANTHARAMAN AND C. SURYANARAYANA, *Rapidly Solidified Metals: A Technological Overview*. Trans Tech Publications, Aedermannsdorf (1987).

9.....B.L. MORDIKE AND R.W. BERGMANN in *Rapidly Solidified alloys and their Mechanical and Magnetic Properties* (edited by B.C. Giessen, D.E. Polk and A.I. Taub), p. 3. Materials Research Society, Pittsburg (1986).

10.....R. MEHRABIAN, S.C. HSU, C.G. LEVI AND K. KOU, *Advances in Metal Processing*, 13 (1981).

11.....C. HAYZELDEN, J.J. RAYMENT AND B. CANTOR, *Acta metall.* **31**, 379, (1983).

12.....K. TAKESHITA AND P.H. SHINGU, *Trans. Jpn. Inst. Met.* **27**, 454 (1986).

13.....S.Y. Lee, P. Nash and S. Bradley, *J. Mater. Scie.* **25**, 1219, (1990).

14.....E.A. Strange and C.H. Pim, U.S. Patent No. 905,758 (December 1, 1908).

15.....R.B. Pond, U.S. Patent No. 2,825,108 (March 4, 1958).

16.....R.E. Maringer, *Mater. Scie. Eng.* **98**, 13 (1988).

17.....H.H. Liebermann and C.D. Graham, Jr., *IEEE Trans. Magn.* **12**, 921, (1976).

18.....S.J.B. Charter, D.R. Mooney, R. Cheese and B.Cantor, J. *Mater. Scie.* **15**, 2658, (1980).

19.....S. Kavesh in *Metallic Glasses* (edited by J.J. Gilman and H.J. Leamy), p. 36. ASM, Metals Park, Ohio, (1976).

20.....J.H. Vincent and H.A. Davies in *Solidification Technology in the Foundry and Casthouse*, p. 153. The Metals Society, London (1983).

21.....L. Katgerman, *Scripta metall.* **14**, 861 (1980).

22.....Z. Sun and H.A. Davies, *Mater. Scie. Eng.* **98**, 71 (1988).

23.....L.A. Anestiev, *Mater. Scie. Eng.* **A110**, 131, (1989).

24.....A.G. Gillen and B. Cantor, *Acta metall.* **33**, 1813 (1985).

25.....B.P. Bewlay and B. Cantor, *Int. J. Rapid Solidifn* **2**, 107 (1986).

26.....J.H. Vincent, J.G. Herbertson and H.A. Davies in *Rapidly Quenched Metals IV* (edited by T. Masumoto and K. Suzuki) Vol. 1, p. 77. Japan Institute of Metals, Sendai (1982).

27.....R.C. Ruel, *Mater. Scie. Eng.* **1**, 313 (1967)

28.....B. Cantor, W.T. Kim, B.P. Bewlay and A.G. Gillen, *J. Mater. Scie.*, **26**, 1266 (1991).

29.....H. Jones, *Rep. Prog. Phys.* **36**, 1425 (1973).

30.....H.S. CARSLAW AND J.C. JAEGER, *Conduction of Heat in Solids*. Oxford University Press, Oxford (1959).

31.....R. MEHRABIAN, *Int. Met. Rev.* **27**, 185 (1982)

32.....P.G. BOSWELL AND G.A. CHADWICK, *Scripta metall.* **11**, 459 (1977).

33.....T.C. PENG, S.M.L. SASTRY, J.R. O'NEAL AND J.F. TESSON in *Lasers in Materials Processing* (edited by E.A. Metzbower) p. 241. ASM., Metals Park, Ohio (1983).

34.....E. VOGT, *Int. J. Rapid Solidifn.* **3**, 131 (1987).

35.....H. HILLMAN AND H.R. HILZINGER in *Rapidly Quenched Metals III* (edited by B. Cantor) Vol. 1, p. 22. The Metals Society, London (1978).

36.....S.C. HUANG, R.P. LAFORCE, A.M. RITTER AND R.P. GOEHNER, *Metall. Trans. A* **16A**, 1773, (1985).

37.....D.J. THOMA, T.K. GLASGOW, S.N. TEWARI, J.H. PEREPEZKO AND N. JAYARAMAN, *Mater. Scie. Eng.* **98**, 89 (1988).

38.....L. KATGERMAN in *Science and Technology of the Undercooled Melt* (eds. P.R. Sahm, H. Jones and C.M. Adams), p. 121. Martinus Nijhoff, Dordrecht (1986).

39.....S.C. HUANG AND H.C. FIEDLER, *Mater. Scie. Eng.* **51**, 39 (1981).

40.....H. JONES, *Mater. Scie. Eng.* **A137**, 77 (1991).

41.....G. -X. WANG AND E.F. MATTHYS, *Mater. Scie. Eng.* **A136**, 85 (1991).

42.....W. KURZ AND D.J. FISHER, *Fundamentals of Solidification*. Trans Tech Publications, Aedermannsdorf (1989).

43.....W. KURZ AND R. TRIVEDI, *Acta metall. mater.* **38**, 1 (1990).

44.....P. DUWEZ, R.H. WILLENS AND W. KLEMENT, *J. Appl. Phys.* **31**, 1136 (1960).

45.....J.W. RUTTER AND B. CHALMERS, *Can J. Phys.* **31**, 15 (1953).

46.....W.A. TILLER, J.W. RUTTER, K.A. JACKSON AND B. CHALMERS, *Acta metall.* **1**, 428 (1953).

47.....M. COHEN in *Specialty Steels and Hard Metals* (edited by N.R. Comins and J.B. Clark), p. 1. Pergamon Press, Oxford (1983).

48.....M.C. FLEMINGS, *Solidification Processing.* McGraw-Hill, New York (1974).

49.....J.W. CAHN, S.R. CORIELL AND W.J. BOETTINGER in *Laser and Electron Beam Processing of Materials, Proc. Symp. of Materials Research Society* (edited by C.W. White and P.S. Peercy), p. 89. Academic Press, New York (1980).

50.....J.C. BAKER AND J.W. CAHN, *Acta metall.* **17**, 575 (1969).

51.....K.A JACKSON, G.H.GILMER AND H.J.LEAMY in *Laser and Electron Beam Processing of Materials, Proc. Symp. of Materials Research Society* (edited by C.W. White and P.S. Peercy), p. 104. Academic Press, New York (1980).

52.....M.J. AZIZ, *J. Appl. Phys.*, **53**, 1158 (1982).

53.....J.C. BAKER AND J.W CAHN in *Solidification*, p 23. ASM, Metals Park, Ohio (1971).

54.....W.J. BOETTINGER in *Rapidly Solidified Amorphous and Crystalline Alloys, Proc. Symp. of Materials Research Society* (edited by B.H. Kear, B.C. Giessen and M. Cohen) p. 15. Elsevier/North-Holland, New York (1982).

55.....W.W. MULLINS AND R.F. SEKERKA, *J. Appl. Phys.* **35**, 444 (1964).

56.....S.R CORIELL AND R.F. SEKERKA in RAPID SOLIDIFICATION PROCESSING *Principles and Technologies II* (edited by R Mehrabian, B.H. Kear and M. Cohen), p. 35. Claitors Publishing Division, Banton Rouge, LA (1980).

57.....M. COHEN, B.H. KEAR AND R. MEHRABIAN in *Rapid solidification processing: Principles and Technologies II.* (edited by R. Mehrabian, B.H. Kear and B.H. Kear) p. 1. Claitors Publishing Division, Baton Rouge, LA. (1980).

58.....V. LAXMANAN, *Acta metall.* **37**, 1109 (1989).

59.....J.S. LANGER AND H. MÜLLER-KRUMBHAAR, *J. Cryst. Growth*, **42**, 11 (1978).

60.....J.S. Langer and H. Müller-Krunbhaar, *Acta metall.* **26**, 1681, 1689, 1697 (1978).

61.....W. Kurz, B. Giovanola and R. Trivedi, *Acta metall.* **34**, 823 (1986).

62.....J.S. Langer, *Phys. Rev. A,* **33**, 435 (1986).

63.....P. Pelce (ed.), *Dynamics of Curved Fronts.* Academic Press, New York and London (1988).

64.....W.J. Boettinger, D. Shechtman, R.J. Schaefer and F.S. Biancaniello, *Metall. Trans. A*, **15A**, 55 (1984).

65.....V. Laxmanan, *Mat. Res. Symp. Proc.*, **58**, 41 (1986).

66.....W.J. Boettinger, S.R. Coriell and R.F. Sekerka, *Mater. Scie. Eng.* **65**, 27 (1984).

67.....J. Lipton, W. Kurz and R. Trivedi, *Acta metall.* **35**, 957 (1987).

68.....J. Lipton, W. Kurz and R. Trivedi, *Acta metall.* **35**, 957 (1987).

69.....A.L. Greer, *Mater. Scie. Eng.* **A133**, 16 (1991).

70.....F. Spaepen and D. Turnbull in *Rapidly Quenched Metals II* (edited by N.J. Grant and B.C. Giessen), Vol.1, p. 205. MIT Press, Cambridge, Massachusetts (1972).

71.....D. Turnbull and B.G. Bagley in *Treatise on Solid State Chemistry* (edited by N.B. Hannay), Vol. 5, p. 513. Plenum, New York (1975).

72.....T.W. Clyne, *Metall. Trans. B.* **15B**, 369 (1984).

73.....M.G. Chu and D.A. Granger, *Metall. Trans. A*, **21A**, 205 (1990).

74.....W.T. Kim and B. Cantor, *Scr. Metall. Mater.* **24**, 633 (1990).

75.....A.K. Sinha, B.C. Giessen and D.E. Polk in *Treatise on Solid State Chemistry* (edited by N.B. Hannay), Vol. 3, p. 1. Plenum, New York (1976).

76.....D. Turnbull, *Metall. Trans. A*, **12A**, 695 (1981).

77.....*Proceedings of the Seventh International Conference on Rapidly Quenched Metals* (Editors H. Fredriksson and S. Savage) in *Mater. Scie. Eng.* **A134** (1991).

78.....J.L. Murray in *Binary Alloy Phase Diagrams* (edited by T.B. Massalski) Vol. 1, p. 324. ASM (1986).

79.....P. Pietrokowsky, *J. Inst. Met.* **90**, 434 (1962).

80.....J. Dutkiewicz and G. Thomas, *Met. Trans.* **6A**, 1919 (1975).

81.....P.R. Okamoto and G. Thomas, *Acta metall.* **19**, 825 (1971).

82.....E. Ruedl, P Delavignette and S. Amelinckx, *Phys. Stat. Sol.* **28**, 305 (1968).

83.....A.G. Khachaturyan, *Prog. Mater. Scie.* **22**, 1 (1978).

84.....D. de Fontaine, *Solid St. Phys.* **34**, 73 (1979).

85.....E. Ruedl, P. Delavignette and S. Amelinckx, *Phys. Stat. Sol.* **28**, 305 (1968).

86.....S.K. Das, P.R. Okamoto, P.M.J. Fisher and G. Thomas, *Acta metall.* **21**, 913 (1973).

87.....R. de Ridder, G. Van Tendeloo and S. Amelinckx, *Acta crystallogr.* **A32**, 216, 1976.

88.....P.R. Okamoto and G. Thomas, *Acta metall.* **19**, 825 (1971).

89.....D. de Fontaine, *Acta metall.* **23**, 553 (1975).

90.....A.G. Khachaturyan, *Phys. Stat. Sol. B* **60**, 9 (1962).

91.....L.D. Landau, *Phys. Zet. Sowjet Un.* **11**, 26 (1937).

92.....G. Van Tendeloo, S. Amelinckx and D. de Fontaine, *Acta crystallogr.* **B41**, 281 (1985).

93.....W.M. Stobbs and S.H. Stobbs, *Phil. Mag.* B, **53**, 537, 1986.

94.....R. Kikuchi, *Phys Rev. B*, **81**, 988 (1951).

95.....G. Gaffner, *Gold Bull.* **22**, 112 (1989).

96.....P. Mathews, *Experimental Physical Chemistry,* p. 60. Claredon Press, Oxford (1985).

97.....A.K. Jena, A.K. Gupta and M.C Chaturvedi, *Acta metall.* **37**, 885 (1989).

98.....G.F. Van Der Voort, *Metallography: Principals and Applications*, p. 629. McGraw-Hill, New York (1984).

99.....E. Batawi, M.A. Morris and D.G. Morris, *Mater. Scie. Eng.* **98**, 161 (1988).

100...T. Schober and A. Meisenburg, *Praktische Metallographie* **13**, 87 (1976).

101...H. Jones, *Mater. Scie. Eng.* **5**, 1 (1969/70).

102...F.B. Pickering, *The Basis of Quantitative Metallography*, p.19. Institute of Metallurgical Technicians, London (1976).

103...J. Silcox and P.B. Hirsch, *Phil. Mag.* **4**, 72 (1959).

104...S. Banerjee, K. Urban. and M. Wilkens, *Acta metall.* **32**, 299 (1984).

105...J.-P. Chevalier and W.M. Stobbs, *Acta metall.* **27**, 1197 (1979).

106...M.C. Flem ings in *Encyclopedia of Materials Science and Engineering* (ed. M.C. Bever), Vol. 6, p. 4241. Pergamon Press, Oxford (1986).

107...D. Pavuna, *J. Mater. Scie.* **16**, 2419 (1981).

108...T.R. Antony and H.E. Clyne, *J. Appl. Phys.* **49**, 829 (1978).

109...E.M. Savitski (Editor) *Handbook of Precious Metals*. Hemisphere Publishing Corporation, London (1989).

110...D. Shechtman (Private communication)

111...H. Jones, *Mater. Lett.* **6**, 181 (1988).

112...J.A. Juarez-Islas, H. Jones and W. Kurz, *Mater Scie. Eng.* **98**, 201 (1988).

113...M.A. Morris and D.G. Morris, *Acta metall.* **35**, 2511 (1987).

114...E. Batawi, M.A. Morris and D.G. Morris, *Acta metall.* **36**, 1755 (1988).

115...H. Biloni in *Physical Metallurgy* (eds. R.W. Cahn and P. Haasen), p. 478. North Holland, Amsterdam (1983).

116...S.C. Flood and J.D. Hunt, J. *Cryst. Growth* **82**, 552 (1987).

117...E. Raub, P. Walter and M. Engel, *Z. Metallkunde* **43**, 112 (1952)

118...T. Aboud, MSc thesis, Technion, Haifa, Israel (1992).

119...M.P. Shaw and J.V. Bee in *Proc. XIth Int. Cong. on Electron Microscopy* (edited by T. Imura, S. Maruse and T. Suzuki), p. 1275. Japanese Society of Electron Microscopy, Tokoyo (1986).

120...D. Harker, *J. chem. Phys.* **13**, 315 (1944).

121...B. Chakravarti, E.A. Starke Jr and B.G. LeFevre, *J. Mater. Scie.* **5**, 394 (1970).

122...V.K. Vasudevan, E.E. Stansbury and C.R. Brooks, *Acta metall. mater.* **40**, 2113 (1992).

123...O.J. Kleppa and L. Topor, *Metall. Trans. A,* **16A**, 93 (1985).

124...P.G. Shewmon, *Diffusion in Solids*. McGraw-Hill, New York (1963).

125...T.C. Tisone and J. Drobek, *J. Vac. Sci. Technol.* **9**, 271 (1972).

126...C. DeW. Van Siclen and W.G. Wolfer, *Acta metall. mater.* **40**, 2091 (1992).

127...L. Edmond, *Met. Prog.* **74**, 97 (1958); **76**, 114 (1959).

128...G. Gafner, *J. S. Afr. Inst. Min. Metall.* **89**, 173 (1989).

APPENDIX 1

GLOSSARY OF TECHNICAL TERMS AND ABBREVIATIONS

wt.%	Weight percent
at.%	Atomic percent
CBMS	Chill block melt spinning
A_r	Cross-sectional area of a melt spun ribbon (m^2)
ϕ	Liquid jet diameter during chill block melt spinning (m)
P	Expulsion gas overpressure during chill block melt spinning (Pa)
V_s	Surface velocity of the melt spinning wheel (ms^{-1})
ρ	Density of the melt (kg/m^3)
w	Width of the melt spun ribbons (w)
Q	Volumetric flow rate of the melt (m^3/s)
X	Thickness of the melt spun ribbons (m)
h	Heat transfer coefficient at the ribbon-wheel interface (W/m^2K).
T	Temperature (K unless otherwise stated)
T_w	Wheel temperature (K)
R	Solidification front velocity (m/s)
T_f	The alloy freezing temperature (K)
x	Distance solidified (measured in a direction perpendicular to the ribbon-wheel interface) (m)
N	Nusselt number (hX/k_s)

k_s	Thermal conductivity of the solid (W/mK)
l_{pool}	Melt pool length (m)
θ_R	Residence time of melt in the puddle (s)
k	Equilibrium partition co-efficient at the solid-liquid interface
C_0	Initial alloy concentration (at.%, wt.%)
T_l	Local equilibrium solidification temperature of an element of the melt (K)
G_L	Temperature gradient in the melt ahead of the advancing solid-liquid interface (K/m)
T_q	Local temperature of an element of the melt (K)
m_L	Slope of the equilibrium liquidus line (defined as being positive when k is greater than unity, negative when k is less than unity) (K/wt.%)
G_C	Unperturbed solute gradient in the liquid at the solid-liquid interface (wt.%/m)
D_L	Diffusivity coefficient of the solute in the melt (m^2/s)
δ	Characteristic diffusion length (m)
k_v	Velocity-dependent partition coefficient
δ_i	Length of interatomic dimensions which characterises compositional rearrangement at the solid-liquid interface (m)
D_i	Interface diffusion coefficient (m^2/s)
R_{trap}	Critical interface velocity for complete solute trapping during solidification (m/s)
T_0	Temperature at which the free energies of the solid and liquid phases are equal for a particular alloy composition (K)
ΔG_r	Change in Gibbs free energy associated with the presence of a curved solid-liquid interface (J/mol)
ν_m	Molar volume of the solid (m^3/mol)
γ	Solid-liquid interface energy (J/m^2)
K	Curvature
r_1, r_2	Principle radii of the curved surface (m)
z	Direction of advance of the solid-liquid interface (m)
x, y	Directions contained within the plane of the solidification front (m)
ω	Wave number (/m)
λ	Wavelength (m)

T_M	Equilibrium melting temperature of the interface in the absence of solute and curvature (K)
ΔH_f	Latent heat of fusion per unit mass (J/kg)
ρ_S	Solid density (kg/m^3)
k_l	Thermal conductivity of the liquid (W/mK)
G_S	Temperature gradient in the solid at the solid-liquid interface (K/m)
G^*	Effective temperature gradient at the solidification front (K/m)
R_{abs}	Critical solid-liquid interface velocity for interface stability (m/s)
ΔT_0	Alloy freezing range (= $m_L(1-k)C_0/k$) (K)
Γ	Gibbs-Thomson coefficient (Km)
λ_i	Critical wavelength for interface stability (m)
r_d	Dendrite tip radius (m)
$(R_{abs})_c$	Contribution to the critical interface velocity for interface stability from the solute field (m/s)
$(R_{abs})_t$	Contribution to the critical interface velocity for morphological stability from the thermal fields at the solid-liquid interface (m/s)
a	Thermal diffusivity (m^2/s)
θ_t	Unit thermal undercooling ($\Delta h_f/C$) (K)
Δh_f	Latent heat of fusion per unit volume (J/m^3)
C	Volumetric specific heat (J/kgK)
T_N	Temperature at which nucleation occurs in the undercooled melt (K)
T_G	Steady state solidification temperature (K)
C'	Specific heat modified to take into account the evolution of the latent heat of solidification (J/kgK)
ΔT_n	Nucleation undercooling (T_M - T_N) (K)
d	Grain diameter (m)
f.c.c.	Face centred cubic
DSC	Differential scanning calorimetry
SEM	Scanning electron microscopy
TEM	Transmission electron microscopy
l	Measured length of a section of ribbon (m)
ρ_r	Theoretical alloy density (kg/m^3)

W_r	Weight of a section of ribbon (kg)
X_{ave}	Calculated average thickness of a melt spun ribbon (μm)
X_{meas}	Average thickness of a melt spun ribbon measured directly from a polished ribbon cross-section (μm)
WDS	Wavelength dispersive spectroscopy
EDS	Energy dispersive spectroscopy
D_{ave}	Average grain diameter (as calculated by the mean linear intercept method) (μm)
d_{mean}	Mean linear intercept (i.e. 1/n) (μm)
n	Number of grain boundaries per unit length of traverse in the mean linear intercept method
σ_d	Standard deviation associated with the grain size as determined by the mean linear intercept method (μm)
σ_{int}	Standard deviation of the individual intercept lengths (in the mean linear intercept technique) (μm)